Investigating the role of cGMP-dependent protein kinase I in thermogenesis in mice

Dissertation
der Mathematisch-Naturwissenschaftlichen Fakultät
der Eberhard Karls Universität Tübingen
zur Erlangung des Grades des
Doktors der Naturwissenschaften
(Dr. rer. nat.)

vorgelegt von
Ioannis-Angelos Vachaviolos
aus Alexandroupolis, Griechenland

Tübingen
2019

Investigating the role of cGMP-dependent protein kinase I in thermogenesis in mice

Tag der mündlichen Prüfung: 05.02.2020

Dekan der Math.-Nat. Fakultät: Prof. Dr. W. Rosenstiel

1. Berichterstatter: Prof. Dr. Robert Feil
2. Berichterstatter: Prof. Dr. Marlies Knipper

Prüfungskommission: PD Dr. Hannes Schmidt
Prof. Dr. Peter Ruth

Erklärung / Declaration:

Ich erkläre hiermit, dass ich diese zu meiner Promotion eingereichte Arbeit mit dem Titel: „Investigating the role of cGMP-dependent protein kinase I in thermogenesis in mice“ selbständig verfasste, nur die angegebenen Quellen und Hilfsmittel benutzt und wörtlich oder inhaltlich übernommene Stellen als solche gekennzeichnet habe. Ich versichere an Eides statt, dass diese Angaben wahr sind und dass ich nichts verschwiegen habe. Mir ist bekannt, dass die falsche Abgabe einer Versicherung an Eides statt mit Freiheitsstrafe bis zu drei Jahren oder mit Geldstrafe bestraft wird.

I hereby declare that I have produced this work entitled "Investigating the role of cGMP-dependent protein kinase I in thermogenesis in mice", submitted for the award of a doctorate independently, without assistance from external parties, have used only the sources and aids indicated and have marked passages included from other works, whether verbatim or in content, as such. I swear on oath that these statements are true and that I have not concealed anything. I am aware that making a false declaration under oath is punishable by imprisonment up to three years or a fine.

Tübingen, den ....
Datum / Date Unterschrift /Signature

Ithaka

Brichst du auf gen Ithaka,
wünsch dir eine lange Fahrt,
voller Abenteuer und Erkenntnisse.
Die Lästrygonen und Zyklopen,
den zornigen Poseidon fürchte nicht,
solcherlei wirst du auf deiner Fahrt nie finden,
wenn dein Denken hochgespannt, wenn edle
Regung deinen Geist und Körper anrührt.
Den Lästrygonen und Zyklopen,
dem wütenden Poseidon wirst du nicht begegnen,
falls du sie nicht in deiner Seele mit dir trägst,
falls deine Seele sie nicht vor dir aufbaut.

Wünsch dir eine lange Fahrt.
Der Sommermorgen möchten viele sein,
da du, mit welcher Freude und Zufriedenheit!
In nie zuvor gesehene Häfen einfährst;
Halte ein bei Handelsplätzen der Phönizier
Und erwirb die schönen Waren,
Perlmutter und Korallen, Bernstein, Ebenholz
Und erregende Essenzen aller Art,
so reichlich du vermagst, erregende Essenzen,
besuche viele Städte in Ägypten,
damit du von den Eingeweihten lernst und wieder lernst.

Immer halte Ithaka im Sinn.
Dort anzukommen ist dir vorbestimmt.
Doch beeile nur nicht deine Reise.
Besser ist, sie dauere viele Jahre;
Und alt geworden lege auf der Insel an,
reich an dem, was du auf deiner Fahrt gewannst,
und hoffe nicht, dass Ithaka dir Reichtum gäbe.

Ithaka gab dir die schöne Reise.
Du wärest ohne es nicht auf die Fahrt gegangen.
Nun hat es dir nicht mehr zu geben.

Auch wenn es sich dir ärmlich zeigt, Ithaka betrog dich nicht.
So Weise, wie du wurdest, in solchem Maße erfahren,
wirst du ohnedies verstanden haben, was die Ithakas bedeuten.

Konstantinos Kavafis

Nun, dass meine Reise auch zu Ende ist,
nun, dass ich meine Ithaka erreicht habe,
nun möchte ich zurückblicken, und
ganz vom Herzen aus,
Professor. Robert Feil danken,
denn ich wäre ohne ihn nie „auf die Fahrt gegangen“.

Sie war nicht immer einfach, das muss man sagen!
Denn manchmal, der durch den wütenden Poseidon erregte Sturm, vernebelte mir den Weg.
Und wenn ich meine Ithaka nicht mehr im Sicht hatte,
wenn ich hoffnungslos mich im kalten Ozean kämpfte,
dort kamen Dr. Susanne und Robert Feil an und
zeigten mir den Weg wieder zu der Ithaka.

Nun dass diese Reise zu Ende ist, viele sind die „Korallen, und die Bernsteine,
und die Essenzen aller Art“, die ich erworben habe, und jetzt, weiser, so wie ich geworden bin,
möchte ich hiermit allen dafür sehr danken. Dr. Hannes Schmidt,
Dr. Markus Wolters, Barbara Birk,
und allen anderen Laborleuten, ganz herzlich,
die mich zu dieser Fahrt begleitet und unterstützt haben.

Zum Schluss und ganz wichtig, möchte ich mich bei meiner Familie und meinen Freunden bedanken. Denn ich hätte mich ohne sie erst gar nicht auf diese Reise begeben. Besonders bei meiner Mutter und meinem Bruder, die sich jedes Mal auf den Weg nach Deutschland machten, wenn ich sie gebraucht habe. Danke euch dafür!

Vielen Dank an alle für diese schöne Reise!

Table of Contents

Zusammenfassung

In der vorliegenden Arbeit wurde die Bedeutung der cGMP-abhängigen Proteinkinase I (cGKI) für die durch Kältestress induzierte Thermogenese in Mäusen untersucht. Genetisch veränderte Mäuse, denen die cGKI im Nervensystem fehlt (cGKI-Hirn KO Mäuse), wurden mit Hilfe der Cre/lox Technologie durch Verwendung von Nestin-Cre Mäusen erzeugt. Die Versuchstiere wurden einer Kältebelastung unterzogen und hinsichtlich verschiedener Parameter untersucht. Gemessen wurde u.a. ihre Körpertemperatur mittels rektaler Sonde, der Noradrenalin-Gehalt im braunen Fettgewebe („brown adipose tissue“, BAT) mittels Immuntest, der Gehalt an Proteinen, die mit der Thermogenese assoziiert sind, durch Western Blot, sowie die Aktivität des BAT durch Positronen-Emissions-Tomographie (PET) mit radioaktiv markierter Glukose ([^{18}F]FDG). Des Weiteren wurden cGMP-Messungen mit einem Fluoreszenz Resonanz Energie Transfer (FRET)-basierten cGMP-Sensorprotein und zahlreiche Analysen des BAT mittels Immunfärbungen durchgeführt.

Wir haben die Expression von cGKI in verschiedenen Regionen des Hypothalamus sowie in neuronalen und nicht-neuronalen Zellen des BAT nachgewiesen, nicht aber in den braunen Fettzellen selbst. cGKI-Hirn KO Mäuse zeigten eine beeinträchtigte Regulation der Körpertemperatur während akutem Kältestress. Die Noradrenalin-Konzentration war im BAT von cGKI Mutanten unter basalen Bedingungen signifikant reduziert und nach Kälteexposition tendenziell geringer als bei Kontrolltieren. Der Gehalt an Tyrosinhydroxylase und „Uncoupling Protein 1“ war im BAT aller Versuchsgruppen ähnlich, sowohl vor als auch nach Kälteexposition. Die PET-Analyse wies darauf hin, dass die BAT-Aktivität von cGKI-Hirn KO Mäusen unter Kältestress signifikant geringer war als von Kontrolltieren. FRET-basierte cGMP-Messungen in Gewebelebendschnitten zeigten, dass bestimmte cGKI-positive Zellen im BAT durch NO zur cGMP-Synthese angeregt werden können. Diesen bisher noch nicht beschriebenen cGKI-positiven Zelltyp haben wir nicht nur im BAT, sondern auch in der Nebennierenrinde entdeckt und mittels Immunfärbung mit Markerproteinen als Perizyten, die mit kleinen Blutgefäßen assoziiert sind, identifiziert.

In dieser Arbeit haben wir eine wichtige Rolle von cGMP und der cGKI für die kälteinduzierte Thermogenese im BAT von Mäusen nachgewiesen. Unsere Ergebnisse weisen darauf hin, dass die cGKI nicht direkt in den braunen Fettzellen exprimiert wird, sondern die BAT-Aktivität

indirekt reguliert, z.B. über die Noradrenalin-Ausschüttung von Neuronen und/oder über Perizyten an Kapillaren, die möglicherweise den Blutfluss im BAT beeinflussen.

Abstract

This project investigated the role of cGMP-dependent protein kinase I (cGKI) in cold-stress-induced thermogenesis in mice. A genetic mouse model lacking cGKI in the nervous system (cGKI-brain KO mice) was generated via Cre/lox technology using the Nestin-Cre mouse line. After exposure of experimental animals to cold-stress, multiple parameters were analysed. We measured body temperature with a rectal probe, noradrenaline content in brown adipose tissue (BAT) by immunoassay, thermogenesis-related proteins by Western blot, and BAT activity via positron emission tomography (PET) with radio-labelled glucose ([^{18}F]FDG). cGMP was monitored using a fluorescent resonance energy transfer (FRET)-based cGMP sensor protein, and numerous other BAT analyses were performed by immunostaining.

We have demonstrated the expression of cGKI in different regions of the hypothalamus as well as in neuronal and non-neuronal cells of BAT, but not in brown adipocytes themselves. cGKI-brain KO mice showed impaired regulation of body temperature during acute cold-stress. Noradrenaline concentration was significantly lower in BAT of cGKI mutant mice under basal conditions and tended to be lower after cold exposure than in control animals. The levels of tyrosine hydroxylase and uncoupling protein 1 were similar in BAT of all experimental groups, both before and after cold exposure. PET analysis indicated that BAT activity of cGKI-brain KO mice under cold-stress was significantly lower than that of control animals. FRET-based cGMP measurements in live tissue sections showed that certain cGKI-positive cells in BAT can be stimulated by NO to generate cGMP. We discovered this previously unknown cGKI-positive cell type not only in BAT, but also in the adrenal cortex, and identified it by immunostaining with marker proteins as pericytes associated with small blood vessels.

In sum, we have demonstrated an important role of cGMP and cGKI in cold-induced thermogenesis in BAT of mice. Our results indicate that cGKI is not directly expressed in brown fat cells, but instead indirectly regulates BAT activity, e.g. via noradrenaline release from neurons and/or via pericytes around capillaries, which may influence blood flow in BAT.

List of Figures

List of tables

List of Abbreviations

ANP	atrial natriuretic peptide
αSMA	α smooth muscle actin
BAT	brown adipose tissue
BNP	brain natriuretic peptide
bp	base pair(s)
BSA	bovine serum albumin
cAMP	cyclic 3’,5’-adenosine monophosphate
CFP	cyan fluorescent protein
cGi500	FRET-based biosensor with EC_{50} 500 nM
cGK	cGMP-dependent protein kinase
cGKI	cGMP-dependent protein kinase I
cGKII	cGMP-dependent protein kinase II
cGMP	cyclic 3’,5’-guanosine monophosphate
CNG	cyclic nucleotide-gated
CNP	C-type natriuretic peptide
CNS	central nervous system
CORT	corticosterone
Cre	cyclisation/recombination
DEA/NO	2-(N,N-diethylamino)-diazenolate-2-oxide diethyl ammonium salt
DMEM	Dulbecco’s modified Eagle medium
DMSO	dimethyl sulfoxide
DNA	deoxyribonucleic acid
EDTA	disodium ethylenediaminetetraacetic acid dihydrate
ELISA	enzyme-linked immunosorbent assay
EM-CCD	electron-multiplying charge-coupled device
eNOS	endothelial NO synthase
F_{480}	emission at 480 nm (CFP emission)
F_{535}	emission at 535 nm (YFP emission)
FRET	fluorescence resonance energy transfer
GC	guanylyl cyclase
GFP	green fluorescent protein
iBAT	interscapular BAT
iNOS	inducible NO synthase
LacZ	β-galactosidase encoding gene
loxP	locus of X-over in P1
mRNA	messenger RNA
Nes-Cre	nestin-Cre
NGS	normal goat serum
nNOS	neuronal NO synthase
NO	nitric oxide
NO-GC	NO-sensitive guanylyl cyclase
NOS	nitric oxide synthase
PBS	phosphate-buffered saline
PET	positron emission tomography
PCR	polymerase chain reaction
PDE	phosphodiesterase
PDGFRβ	platelet-derived growth factor receptor beta
Pen/Strep	penicillin/streptomycin
pGC	particulate guanylyl cyclase
R	CFP/YFP emission ratio
ROI	region of interest
R26	reverse orientation splice acceptor 26 locus
RT	room temperature
SDS	sodium dodecyl sulphate
TBS	tris-buffered saline
TH	tyrosine hydroxylase
Tris	tris(hydroxymethyl) aminomethane
UCP-1	uncoupling protein 1
VSMCs	vascular smooth muscle cells
X-Gal	5-bromo-4-chloro-3-indolyl-β-D-galactopyranoside
YFP	yellow fluorescent protein

A. Introduction

A.1 Introduction to cGMP signalling

Cyclic 3’,5’-guanosine monophosphate (cGMP) is an important intracellular second messenger now appreciated for its pivotal role in a plethora of (patho-) physiological processes. It first attracted attention for its importance in vascular-tone homeostasis [1]. More specifically, it was found that a peptide produced by the cardiac atria in response to heart overload, was capable of bringing about a drop in blood pressure by promoting natriuresis/diuresis, and cGMP-induced relaxation of the blood vessels [2, 3]. Nowadays, cGMP signalling is known to be involved in a wide range of additional processes such as cellular growth and contractility, inflammation, neuronal growth, plasticity, and learning, sensory axon bifurcation [4], and sensory transduction [2, 5], as well as pain perception [6, 7]. Since its first synthesis in the early 1960s [8, 9] and its discovery in rat urine [10], the cGMP area has led to a Nobel Prize awarded in 1998 to Dr Furchgott, Dr Ignarro, and Dr Murad. Nowadays, numerous drugs that target this signalling pathway are approved for clinical use. For example VIAGRA® (Sildenafil) for the treatment of erectile dysfunction, or the organic nitrates to relieve the symptoms of angina pectoris.

cGMP generation relies on two types of guanylyl cyclases (GCs) which differ in their cellular localisation and activators [11, 12]. The NO-GC, previously referred to as “soluble GC” (sGC), is thought to be located mainly in the cytoplasm and can be activated by NO that freely diffuses through the plasma membrane. The second type of GC, named particulate guanylyl cyclases (pGC), is found anchored to the plasma membrane and acts as a receptor for natriuretic peptides (NPs); ANP: atrial natriuretic peptide, BNP: brain natriuretic peptide, and CNP: C-type natriuretic peptide. Upon ligand binding, both GCs facilitate cGMP synthesis from GTP and contribute to the “global and local cGMP pool” (**Figure 1**) [1].

Synthesised cGMP binds and modulates downstream target proteins. The three major target proteins of cGMP are: a) cGMP-dependent protein kinases (cGKs), which phosphorylate target proteins at serine/threonine residues, b) cGMP-dependent phosphodiesterases (PDEs) responsible for cGMP or cAMP degradation and c) cyclic nucleotide-gated channels (CNG), abundantly found in the visual and olfactory system [1]. All the above-mentioned components of the cGMP signalling pathway will be discussed in more detail in the following sections.

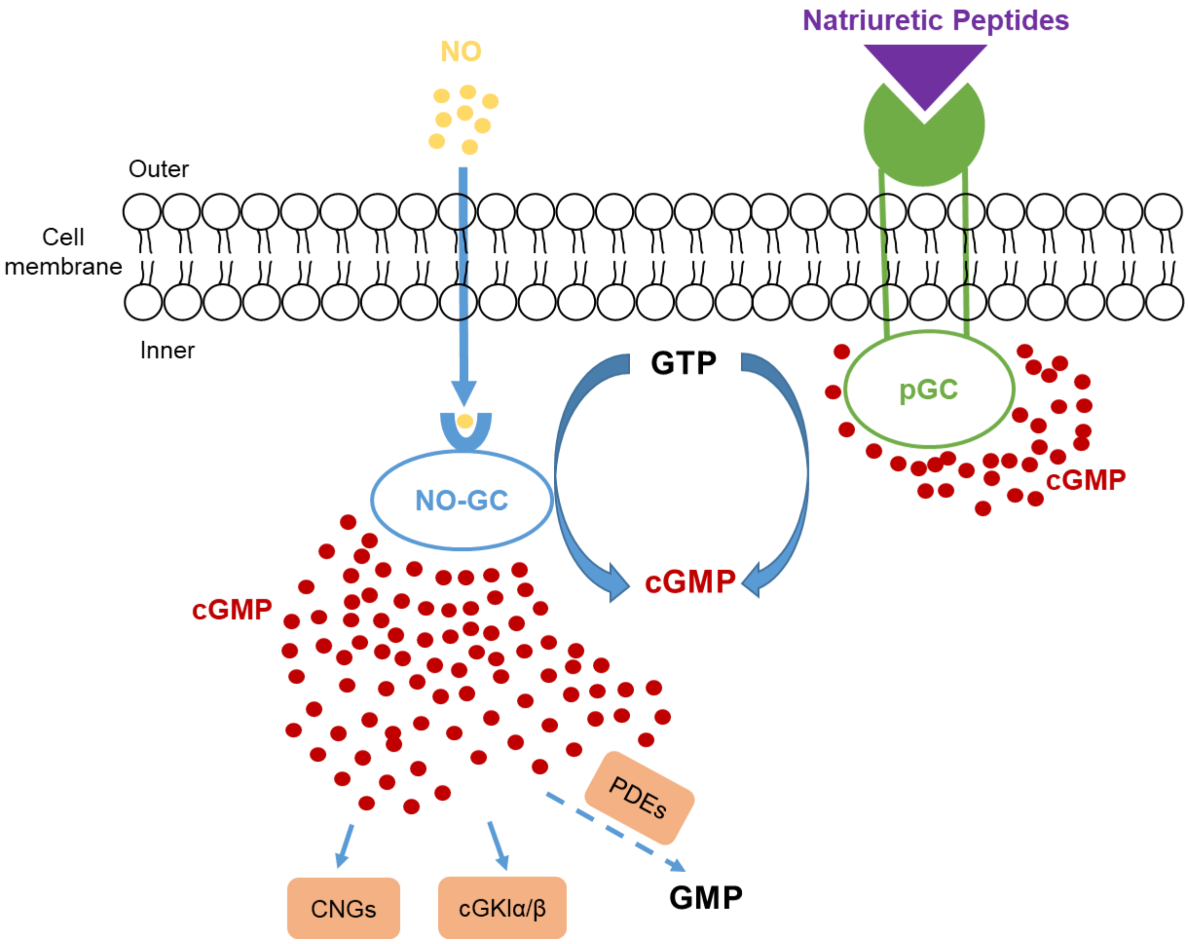

Figure 1. Graphical representation of the components of the cGMP signalling pathway.

The membrane-associated pGC is activated on the extracellular side by ANP, BNP, or CNP, whereas the cytosolic NO-GC is activated by the gaseous molecule NO shown in yellow, which can freely diffuse through the plasma membrane. Both guanylyl cyclases catalyse the conversion of GTP to cGMP and contribute thereby to the local and global pools of cGMP (red dots). Generated cGMP of either pool, exerts its physiological functions through a) cyclic-nucleotide gated channels (CNGs), b) cGMP-dependent protein kinases I α/β (cGKI α/β), and c) cGMP-regulated phosphodiesterases (PDEs), which degrade cGMP to GMP. PDEs are also a means of crosstalk between cGMP and cyclic adenosine-3′, 5′-monophosphate (cAMP) signalling pathway. For instance, PDE3 is a cAMP-degrading PDE that is inhibited by cGMP. Contrarily, PDE1 is boosted by cGMP to degrade cAMP.

A.2 The cGMP signalling pathway: Generators

cGMP is generated from GTP by two distinct classes of guanylyl cyclases, the NO-GC and the pGC, which are going to be discussed below.

The NO-GC is located mainly in the cytosol and acts as a receptor for the gaseous signalling molecule NO [13]. Binding of NO to the Fe^{2+}-haem complex of the β1 subunit of the NO-GC induces conformational changes to the protein leading to enzyme activation (here Mg^{2+} is required as a cofactor) [14-17]. The mammalian NO-GC is a heterodimeric haemoprotein consisting of one alpha (either α1 or α2) and one beta subunit (β1); with the β1 subunit acting as a dimerizing partner for either α subunit [15]. Thus the combination of the subunits gives rise to two NO-GC isoforms: NO-GC1 (consisting of α1β1 subunits) and NO-GC2 (consisting of α2β1 subunits) (**Figure 2**). In the absence of the β1 subunit, the α subunits cannot form dimers and therefore remain catalytically inactive. In more detail, expression studies revealed that the α1 isoform is found ubiquitously distributed with special emphasis in the cardiovascular tissues. The α2-containing isoform, in contrast, is highly expressed in the brain, where it is believed to have an important role in inter-neuronal communication [17, 18]. Mouse strains lacking forms of NO-GC have already been generated to assess the function of NO-GC. Their phenotypes range from mild to more severe ones, and encompass malfunctioning of a series of organs including the gastrointestinal tract, cardiovascular system, platelets, and the neuronal system (for excellent reviews see [15] and [17]). Due to its critical involvement in a plethora of pathologies, the NO-GC system has been the target of newly-developed drugs. For instance, the NO-sensitizer Riociguat and the NO-haem-mimetic Cinaciguat (BAY 58-2667) are now in clinical use and in clinical phase trials (respectively) for the merit of patients with pulmonary hypertension and heart failure, respectively [17, 19].

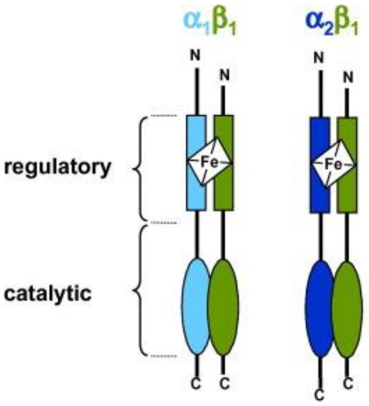

Figure 2. Schematic illustration of the two isoforms of NO-GC.

NO-GC is a heterodimeric enzyme composed of one α and one β subunit. As there are two alpha subunits (α1 and α2) and one beta subunit known, two dimers can be formed: α1β1 and α2β1. The N terminal part of NO-GC contains the regulatory prosthetic haem group, which acts as an NO receptor. Binding of NO results in a conformational change that leads to the activation of the enzyme. The catalytic domain, responsible for the conversion of GTP to cGMP, is located in the C-terminal part of the enzyme. (Adapted from [15]).

NO, in turn, is synthesised by enzymes known as NO-synthases (NOSs). Three isoforms have been described so far: the endothelial NOS (eNOS), the neuronal NOS (nNOS) and the inducible NOS (iNOS). nNOS and eNOS are constitutively expressed and activated by increased intracellular Ca^{2+} concentrations [20] or fluid shear stress [21], respectively. iNOS, on the other hand, is expressed “on-demand” upon stimulation, for instance, with lipopolysaccharides (LPS) or cytokines [22]. As nicely reviewed by Förstermann, all NOS are homodimers that utilise L-arginine as substrate, molecular oxygen (O_2), as well as reduced nicotinamide-adenine-dinucleotide phosphate (NADPH) as co-substrates. NOS synthesise NO in two steps. In the first step, NOS hydroxylates L-arginine to N^{ω}-hydroxy-L-arginine. In the second step, NOS oxidises N^{ω}-hydroxy-L-arginine to L-citrulline and NO [23, 24].

nNOS was the first NOS to be purified and cloned, and it is ubiquitously expressed throughout the CNS, where it serves as the main source of NO in the brain [25]. In the CNS, nNOS-generated NO has been positively linked to synaptic plasticity and learning [26]. However, besides its function as a neurotransmitter in the CNS, NO can also act as a paracrine agent. In 2009, research conducted by Toda *et al.* demonstrated that blockade of nNOS activity in the medulla and hypothalamus of rats caused systemic hypertension, as a result of increased peripheral resistance [27]. In the periphery, outside the CNS, many smooth-muscle tissues are innervated by nitrergic nerves; namely nNOS-containing nerves, able to generate and release NO. The latter can be viewed as an unorthodox neurotransmitter, which is able to provoke NO-GC stimulation in its effector cells, thereby decreasing, for instance, the tone of various smooth-muscle cells [23]. For example, the knowledge of this mechanism has found significant therapeutic application in the treatment of erectile dysfunction [28]. There, nNOS-bearing nitrergic nerves of the corpus cavernosum generate the necessary NO that provokes cGMP-mediated smooth-muscle relaxation, and eventually an increase in blood flow that facilitates and induces erection of the penis. In the clinical practice, PDE5 inhibitors such as sildenafil (Viagra®), vardenafil (Levitra®), or tadalafil (Cialis®) are prescribed for the treatment of erectile dysfunction. They work by increasing cGMP levels in the corpus cavernosum via inhibition of its degradation [29, 30].

eNOS, on the other hand, is mostly expressed in endothelial cells, where it regulates vascular tone and consequently plays a key role in maintaining blood pressure homeostasis [31]. Yet besides endothelial cells, eNOS expression has also been discovered in cardiomyocytes, platelets, as well as in certain neurons [22, 32]. eNOS existence in cardiomyocytes and platelets, in particular, has been linked to certain cardiovascular diseases such as atherosclerosis [23, 33, 34].

First identified in macrophages and microglia, iNOS activation is largely associated with immune responses against microbes [22, 25, 32, 35]. Once expressed, iNOS remains constantly active and contrary to the other two NOSs, its regulation is independent of intracellular Ca^{2+} concentrations [25, 36]. Interestingly, recent data implicate iNOS in a number of brain pathologies such as neurodegeneration [37] and other diseases like cancer, inflammation, asthma, chronic liver diseases, inflammatory bowel disease, arthritis [38].

In contrast to NO-GC, transmembrane pGCs elevate intracellular cGMP concentrations upon binding of ANP, BNP, or CNP, guanylin, uroguanylin, or enterotoxins, thus exercising their roles in the cardiovascular, skeletal, nervous, and reproductive system [39, 40]. ANP and BNP are stored as pro-peptides in the cardiac atria and ventricles, and are secreted in response to cardiac stress, such as congestive heart failure [39]. CNP is present at higher concentrations in chondrocytes and therefore it is implicated in the growth of longer bones [3, 39-41].

So far, three known receptors for NPs exist (**Figure 3**): GC-A (known also as NPR-A or NPR-1), which catalyses the synthesis of cGMP upon binding of ANP [42] or BNP [3, 43], and GC-B (known also as NPR-B or NPR-2) that is homologous to GC-A, but can only be activated by CNP. Renal excretion of Na^{2+}, H_2O, and vasorelaxation constitute the most well-known physiological paradigms of GC-A activation [40]. Last, NP receptor-C (NPR-C), which can bind all three natriuretic peptides, resembles GC-A and GC-B extracellularly, but lacks the intracellular catalytic domain. Although it may have other, so far unknown, signalling functions, the majority of the data indicate that the primary role for NPR-C is to clear natriuretic peptides from the extracellular environment via a receptor-mediated internalisation and degradation process [39]. Indeed, in 2018, Boudin *et al.* showed that bi-allelic inactivating mutations in the NPR-C receptor provoked a phenotype characterised by tall stature, long digits, and variable connective tissue abnormalities, including aortic dilatation and joint hypermobility. The origin of these defects was postulated to be the enhanced activity of the GC-A/B receptors, due to reduced clearance of natriuretic peptides by the defective NPR-C receptor [44]. Furthermore, recent studies have pinpointed the significance of the CNP/GC-B/cGMP/cGKI signalling pathway in sensory axon bifurcation in the developing spinal cord, and also in axon guidance [4, 45].

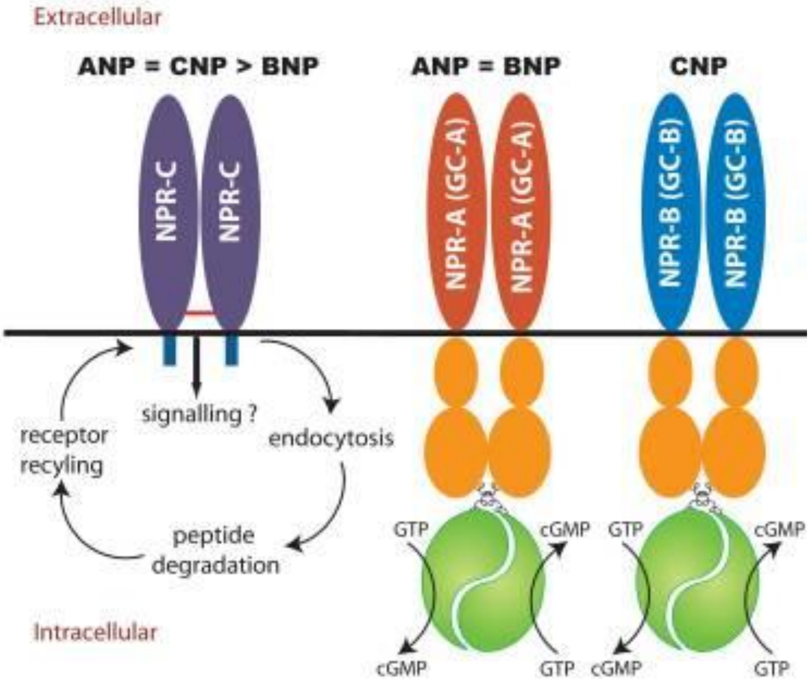

Figure 3. Schematic representation of the natriuretic peptide signalling system.

NPs: ANP, BNP, and CNP bind to transmembrane proteins called pGCs or NPR (stands for natriuretic peptide receptors), and induce synthesis of cGMP from GTP. Two classes of pGCs exist with catalytic activity: GC-A, which binds ANP and BNP, and GC-B that only binds CNP. The NPR-C receptor can bind and internalise all three natriuretic peptides thus delivering them to intracellular proteases for degradation. The upper row indicates the affinity of NPs for each corresponding receptor. NPR-C preferentially binds ANP or CNP with similar affinity, but will also bind BNP with less affinity. ANP exhibits a similar affinity with CNP, and both have greater affinity over BNP. Likewise, ANP demonstrates a similar affinity to BNP for the GC-A receptor. (Adapted from [39]).

A.3 The cGMP signalling pathway: Effector molecules

cGMP exerts its physiological effects via three main types of effectors: a) cGKs, b) CNG cation channels, c) and PDEs (see **Figure 1**).

The cGKs are homodimeric enzymes that belong to the serine/threonine kinase family and consist of three isoforms: cGKIα, cGKIβ, and cGKII. In mammals, two genes termed prkg1 and prkg2 encode for cGKI and cGKII respectively [1, 46, 47]. Regarding the two cGKI isoforms (cGKIα, cGKIβ), which differ in their N-terminal ~100 amino acids, these are most likely the result of an alternative promoter usage upstream of the prkg1 gene. Each subunit of the cGK homodimer consists of three domains: a) the N-terminal domain responsible for homodimerization (via a leucine zipper), interaction with other proteins, and possibly autoinhibition/autophosphorylation of kinase activity in the absence of cGMP [16, 48-51], b) the regulatory domain that is made up of two cGMP-binding pockets and controls the kinase activity, and c) the kinase domain, ultimately responsible for the transfer of the γ-phosphate from ATP to the hydroxyl group of the side chain of a serine/threonine residue at the target protein [52, 53]. For efficient phosphorylation to occur, each regulatory domain requires binding of two cGMP molecules that aid in releasing the catalytic domain from the autoinhibitory/pseudosubstrate domain located at the N-terminal (**Figure 4**) [53, 54]. No less importantly, the N-terminus acts as a targeting sequence and influences the subcellular localisation of the various cGK isoforms. Regarding their localisation, cGKI is located in the cytosol, whereas cGKII resides at the cell membrane [55, 56]. cGKI is highly expressed in smooth-muscle cells, platelets, numerous brain regions (cerebellum, hippocampus, dorsomedial hypothalamus, paraventricular nucleus) as well as in the dorsal root ganglia [46, 57]. In line with its broad expression profile, cGKI is involved in various physiological processes of the cardiovascular system. For instance, cGKI has been shown to control platelet aggregation and thrombosis [58, 59], while in the heart, cGKI was shown to mediate the negative inotropic effects of the NO/cGMP signalling pathway [53, 60]. Moreover, cGKI has been reported to have pro-angiogenic effects on new blood vessel formation [14, 61, 62]. Yet, the most thoroughly investigated effect of cGKI remains its impact on blood flow regulation via the relaxation of VSMCs [63, 64].

In contrast to the cytosolic cGKI, the 87 kDa-heavy cGKII is anchored to the plasma membrane, as a consequence of its myristoylated N-terminus [65]. Even though the structures of cGKII and cGKI are very similar and both form homodimers, they differ in their tissue distribution and function [56, 66, 67]. Analyses have shown localisation of cGKII in the intestinal mucosa, in chondrocytes, lung, kidney, several brain nuclei, as well as the adrenal cortex [5, 56]. In the intestinal mucosa, for example, the cystic fibrosis transmembrane conductance regulator (CFTR) has been identified as an in vivo substrate for cGKII based on its localisation in the apical membrane of enterocytes [68]. Therein cGKII has been found to regulate the intestinal fluid secretion by phosphorylating CFTR. cGKII has also been suggested to be involved in endochondral ossification [69-71], the synchronisation of the circadian clock after induced phase-shifts [72], modulation of anxiety-like behaviour in mice [73], and aldosterone secretion [74, 75].

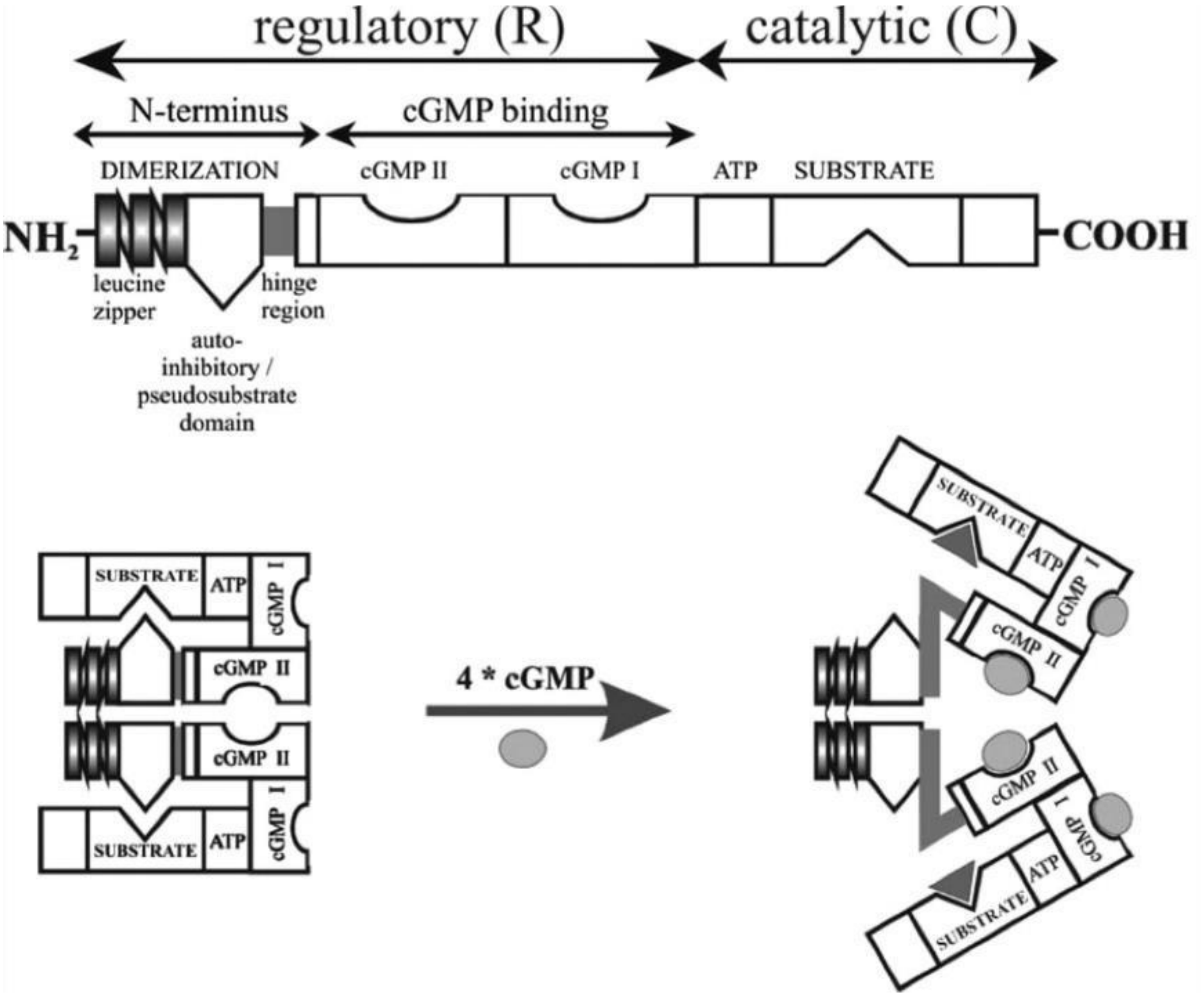

Figure 4. Structure of cGMP-dependent protein kinases (cGKs).

cGKs form homodimers with each subunit consisting of three domains as depicted in the top row of the present illustration: a) the N-terminal domain, providing the regions necessary for homodimerisation and interaction with other proteins, b) the regulatory domain, which binds two cGMP molecules with different affinity (cGMP I > cGMP II) and activates the kinase activity, and c) the kinase domain, which possesses the catalytic activity of the enzyme and is responsible for the transfer of the γ-phosphate group of ATP to the serine/threonine residues of the target proteins. The inactive enzyme is believed to form a “closed” structure, in which the catalytic domain is tightly associated with the autoinhibitory domain of the N-terminus (left-hand-side of the bottom row). Upon binding of 4 cGMP molecules, the catalytic domain is released from the autoinhibitory N-terminal domain and can exercise its catalytic activity. (Taken from [56]).

cGMP can also activate CNG channels, which are located in the plasma membrane and allow the passage of cations. CNG channels belong to the superfamily of the pore-loop cation channels [76, 77] that form heterotetrameric complexes comprising two or three different subunits [78]. The six different CNG-channel genes encode for four A subunits (A1, A2, A3, A4) and two B subunits (B1 and B3) [77]. The resulting six homologous proteins exhibit variable tissue expression patterns and binding affinities to cGMP and cAMP [77]. The channels open upon binding of cyclic nucleotides to the protein's intracellular region and permit the influx of Na^+, K^+, and Ca^{2+}. CNGs exhibit voltage-dependent opening capabilities that are assisted upon binding of cyclic nucleotides [76]. CNG channels are highly expressed in the rod and cone photoreceptors of the retina, in the olfactory bulb, the brain, kidneys, and also in sperm cells [76, 79]. Moreover, CNG channels are present throughout the mammalian CNS and have been implicated in the modulation of the neuronal synaptic function [76, 80, 81]. Interestingly, research performed by Komatsu and colleagues found that cGMP constitutes an important intracellular messenger in *C. elegans's* sensor transduction system, and that a tax-4 channel, with high homology to the vertebrate CNG channels, seems to be essential for thermosensation and chemosensation in that organism [82].

PDEs constitute the last interaction partners of cGMP and are responsible for the degradation of cyclic nucleotides. A total of 21 PDE genes compose over 50 different PDE proteins, due to alternative initiation sites and alternative splicing. PDEs hydrolyse both cGMP and cAMP into GMP and AMP respectively. PDEs 5, 6, and 9 are cGMP-specific, PDEs 4, 7, and 8 are cAMP-specific, while PDEs 1, 2, 3, 10, and 11 degrade both cAMP and cGMP with varying efficiency [83-86]. PDEs encompass allosteric binding sites for both cAMP and cGMP, and their existence has been linked with the notion of cGMP-cAMP crosstalk [87]. Due to their high abundance in tissues of the cardiovascular system, PDEs have traditionally been the targets of numerous drugs for diseases such as pulmonary hypertension or erectile dysfunction. Furthermore, recent research has also implicated PDEs 9, 10, and 11 in a series of mental conditions, such as bipolar disorder [88], social interaction deficits, schizophrenia [89-91], and also in major depression [92]. In the field of adipose tissue biology, research demonstrated, that in BAT of obese "Zucker" rats, PDE2, 3, 4 might modulate cAMP and cGMP signalling, affecting thereby the thermogenic capacity of this organ [93].

A.4 Stress, the HPA axis, and the cGMP signalling pathway

Living organisms, commencing from the most simple, unicellular, to the highest, multicellular ones, are constantly called to cope with various types of stresses that could potentially endanger their homeostatic balance [94]. To prevent disruption of their homeostasis, the neuroendocrine system of the more complex organisms responds to stressful stimuli with activation of the hypothalamic-pituitary-adrenal (HPA) axis in combination with the systemic sympathetic and adrenomedullary nervous system [95]. This process, which is initiated in the hypothalamus, involves a cascade of hormonal secretions, commencing with the release of corticotrophin-releasing hormone (CRH) from the parvocellular cells of the hypothalamic paraventricular nucleus (PVN). CRH, in turn, triggers the secretion of adrenocorticotropic hormone (ACTH), a 39-amino-acid peptide, from the anterior pituitary gland. Ultimately, in the adrenal gland cortex, ACTH stimulates the synthesis and release of corticosterone (CORT) from CORT-producing cells (**Figure 5**). At the same time, preganglionic sympathetic neurons located in the splanchnic nerves stimulate chromaffin cells via acetylcholine (ACh) secretion. As a response, chromaffin cells (found in the adrenal gland medulla), which are made up of modified postganglionic neurons, release catecholamines (mainly adrenaline and to a less extent noradrenaline) into the bloodstream [96].

Holistically seen, the cardiac output and respiration rate are accelerated, catabolism is increased, and the blood flow is redirected to temporarily provide higher amounts of blood to threatened sites and to the alerted brain, heart, and the muscles, as stated by Kyrou and Tsigos [95]. All these actions facilitate the adaptive physiological and behavioural changes in response to the threatening stress stimulus and aim to maximise the chances of the individual for survival. However, chronic stimulation of the stress-response system might have potentially harmful consequences [97-99]. Indeed, excessive and/or chronically-persisting stressors can impair a number of essential physiological functions such as the metabolism, or the cardiovascular [99], and immune system [94, 95, 100, 101]. Interestingly, meta-analyses have found a linkage between chronic stress, depression and type-2 diabetes [95, 102].

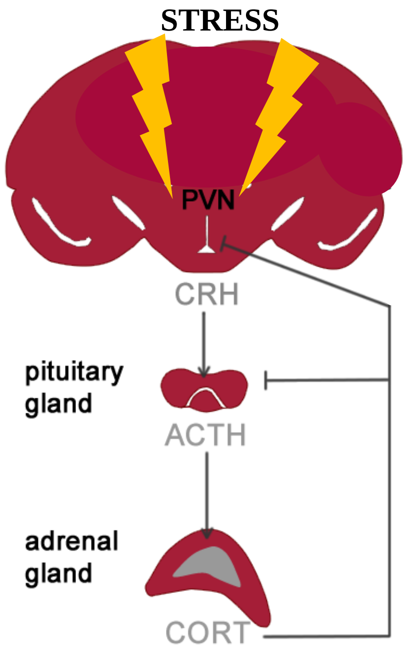

Figure 5. Schematic depiction of HPA axis activation and its negative feedback regulation.

In response to external and internal stressful stimuli, the parvocellular neurons of the hypothalamic paraventricular nucleus (PVN) produce and release corticotrophin-releasing hormone (CRH), which in turn stimulates corticotroph cells in the anterior pituitary gland. As a result, corticotroph cells secrete adrenocorticotropic hormone (ACTH), which, via the bloodstream, reaches the adrenal gland cortex. Upon binding of ACTH to its specific receptors, corticosterone (CORT) is synthesised and secreted into the circulation. CORT inhibits its own secretion at the level of the brain (PVN) and the pituitary gland via negative feedback signalling (Taken from [103]).

The NO/cGMP signalling has long been proposed to be implicated in the modulation of the HPA axis response and steroidogenesis [104-108]. For example, inhibitory effects of NO on CORT production and secretion have been reported for the rat adrenal gland in vitro and in vivo [109, 110]. In contrast, an enhancing effect of NO on the rapid CORT release in ACTH-stimulated hemi-adrenal glands in vitro has also been proposed [111]. Furthermore, in addition to NO, NPs have also been implicated in the HPA axis modulation. For instance, intranasal administration of ANP in humans has been associated with inhibitory effects on the HPA axis regulation [112]. At the adrenal gland level, BNP and ANP inhibit steroidogenesis in an adrenocortical human and mouse tumour cell line, respectively [113, 114]). In bovine zona glomerulosa cells, a rise in cGMP has been suggested to mediate the inhibitory effect of ANP on ACTH-stimulated aldosterone secretion by activating the cGMP-stimulated PDE2, which then rapidly degrades cAMP [115, 116]. Two recent studies suggested that cGKI could modulate basal steroidogenesis in Leydig cells through phosphorylation of StAR, a steroidogenesis rate-limiting enzyme that transports cholesterol to the inner mitochondrial membrane [117, 118]. Moreover, the PDE5-specific inhibitor sildenafil was shown to increase testosterone production in Leydig cells when applied for several days [119]. Another work conducted by Henke and colleagues investigated the impact of NO on aldosterone synthesis in primary cultures of bovine adrenal zona glomerulosa cells. The researchers came to the conclusion that NO in the adrenal gland attenuated aldosterone production independently of a NO-GC/cGMP-signalling pathway [120].

A.5 The HPA axis is involved in thermogenesis

Stress-hormone production, however, (ACTH, adrenaline, noradrenaline, see **A.4**) does not constitute an exclusive stress-response. Another type of (psycho-) physiological stress named cold-stress, triggers via the same initiating organ, the hypothalamus, the production of heat (thermogenesis). Unlike humans, mice are under standard housing conditions (22 °C) exposed to a continuous cold-stress ordeal [121, 122] and are therefore subjected to persistently-active thermogenic processes. During the initial stages of that cold-stress ordeal, the body attempts to minimise dermal heat-loss via a sympathetic system-mediated cutaneous vasoconstriction [123]. Concomitantly, the so-called shivering thermogenesis is also immediately recruited. It results from the repeated skeletal muscle contractions evoked by rhythmic firing of the α-motoneurons, innervating the skeletal muscle fibres [124].

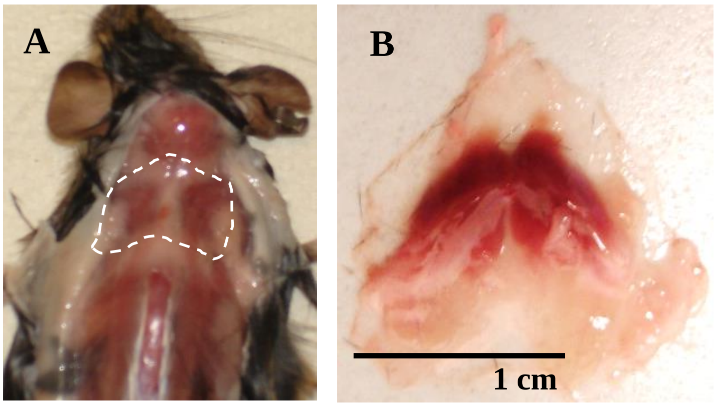

Figure 6. Photographic images of BAT and its location in a mouse.

A) The white-dashed line indicates the location of BAT in the interscapular region of a wild type mouse. B) BAT after excision with scissors. The high content of mitochondria in BAT is responsible for the characteristic brownish colour, which in turn, is responsible for its given name, BAT.

However, prolonged exposure to cold triggers the activation of a specialised thermogenic organ named brown adipose tissue (BAT). Once activated, BAT is then responsible for “warming up” the muscles and the nervous system, so as to prepare the animal for “fight or flight” [125]. In mice, BAT is located primarily in the interscapular region (**Figure 6**), yet smaller portions of it have also been observed in various sites such as the periaortic and perirenal region (own observation). Upon activation, BAT is capable of producing large amounts of heat through a protein found uniquely on the inner mitochondrial membrane of brown adipocytes [126, 127]. The so-called UCP-1, (or thermogenin) “uncouples” ATP synthesis from proton transfer, dissipating thereby the proton gradient generated by the respiratory chain as heat [126, 128].

The production of heat in brown adipocytes requires a complex β-adrenergic stimulation mediated via the sympathetic nervous system. Yet, the “central thermostat” lies away from the target organ, BAT. Numerous studies over the years have demonstrated that several hypothalamic regions are involved in thermoregulation, with the preoptic area of the hypothalamus (POA) playing there a pivotal role [124, 129, 130]. Warm- and cold-sensitive neurons located therein receive and process temperature inputs arriving from distant thermo-sensory neurons of the skin or the core body [124]. Under thermo-neutral conditions (i.e. when production or dissipation of heat is not required), GABAergic neurons of the POA tonically inhibit neurons of the dorsomedial hypothalamus (DMH) [124, 131]. Under cold conditions, the disinhibited GABAergic neurons of the DMH, signal to glutamatergic sympathetic premotor neurons of the raphe pallidus [131-133]. Further downstream, the thermo-excitatory signal passes through multiple serotoninergic neurons of the intermediolateral nucleus of the spinal cord, and eventually reaches the cholinergic preganglionic neurons of the stellate ganglion. In there, the release of acetylcholine culminates into secretion of noradrenaline by the nerve endings into BAT [126, 134]. Released noradrenaline finally reaches brown adipocytes and elicits through β3-adrenergic receptors a Gs-cAMP-protein kinase A (PKA) stimulatory signal. Activated PKA subsequently phosphorylates and activates hormone-sensitive lipase (HSL), which sequentially triggers lipolysis in brown adipocytes [126]. Free fatty acids are then directed to mitochondria through CD36, a fatty acid translocase, and subjected to β-oxidation. Based on the so far-known physiology, two nerve bundles enter the BAT bilaterally, one at the superficial and one at the subscapular region. Both consist of a few "thick" and numerous "thin" nerve fibres, as described by De Matteis *et al.* [135]. The thick nerves contain myelinated, as well as unmyelinated fibres, while the thin ones solely consist of unmyelinated fibres. The thin, unmyelinated fibres are highly positive for TH, and are able to secrete noradrenaline, the main activator of BAT thermogenesis [135]. In short, TH (tyrosine 3-monooxygenase) catalyses the initial and rate-limiting step in the biosynthesis of catecholamines, by converting L-tyrosine into L-3,4-dihydroxyphenylalanine (L-DOPA). L-DOPA can be then converted to dopamine by the enzyme DOPA decarboxylase. Dopamine thereafter can give rise to norepinephrine by the enzyme called dopamine β-hydroxylase [136, 137]. Although TH has been extensively studied and associated primarily with Parkinson's [138] and other severe neurological diseases [139], its role in BAT-related thermogenesis remains crucial.

Not only noradrenaline but also thyroid gland hormones have been found to positively influence thermogenesis occurring in BAT [140-143]. Alvarez-Crespo and colleagues, for instance, reported that central administration of T3 into wild type mice brought about an increase in their body temperature by 0.7 °C. This increase was later discovered to be mediated by upregulation and activation of UCP-1 [144], while Dauncey had come to a similar observation back in 1990 [140].

Until recently, albeit only the cAMP signalling was believed to participate in the sympathetic activation of BAT thermogenesis, current data propose that cGMP signalling as well plays a critical role in BAT biology [145-147]. In 2009, a study led by Haas *et al.* demonstrated that the NO/cGMP/cGKI pathway in preadipocytes was essential for proper brown adipocyte differentiation at later stages, and also for flawless mitochondrial biogenesis in vitro [148]. Interestingly, similar results were published by Zhang and colleagues in 2010. According to their results, sildenafil promoted adipogenesis of a 3T3L1 preadipocyte cell line in a cGK-dependent manner [149]. In another study, mice ubiquitously overexpressing human cGKI were leaner and displayed increased BAT activity as revealed by elevated fat oxidation, UCP-1 abundance and body temperature, compared to controls [150]. Furthermore, ANP and BNP seem to promote lipolysis in cell lines of human preadipocytes via the action of cGKI on HSL and perilipin A [151].

Contrarily to the widely-accepted view that claimed BAT to have only existed in new-born human babies, recent studies have now revealed its existence and functionality in adult humans too [152-154]. After its rediscovery, BAT and the associated thermogenesis have regained attention, this time rather as a possible target organ for combating obesity and the related comorbidities [126, 153-155]. A study conducted by Bartelt and colleagues in 2011, showed that the augmented BAT activity induced by a short-term cold exposure was effective in drastically accelerating the clearance of plasma triglycerides. According to the authors, this unexpected finding resulted from the elevated uptake of triglycerides into BAT, a process reliant on the local lipoprotein lipase activity and the transmembrane fatty acid receptor CD36 [156]. Interestingly, BAT is no longer merely considered as a major site of energy balance, but also as an active endocrine organ able to secrete anti-obesity-related peptides [126, 127, 157, 158]. In humans, BAT amounts have been inversely correlated with the individual’s body mass index (BMI) [159].

A.6 Genetically modified mice: Powerful tools to study gene function

Until now, elegant approaches have been implemented to study gene deletions in various tissues [160, 161]. Of those, transgenic mice still comprise a valuable tool for the investigation of signalling cascades. Their usage in science presents a number of considerable advantages over other animals. For example, a) large mouse colonies can be sustained in a defined space, due to their small size and the relatively low costs, b) a plethora of literature exists on the characterisation of mouse lines, and c) genetic modification techniques are immensely improved for mice in contrast to other animal models. Though, despite the fact that murine genes exhibit a great similarity to those of humans [162-164], the researcher has to always take into consideration that mice are by no means humans, and as a consequence, the conception and analysis of experiments involving mice have to be very well thought [164].

Undoubtedly, Cre/loxP-assisted site-specific recombination (SSR) comprises one of the most prominent systems for generating conditional genetic modifications in the mouse and can be implemented in order to generate mice lacking literally any protein of interest in a time- and tissue-specific manner (such as either form of cGK) [160, 165]. The Cre/loxP system relies on the cyclisation recombination (Cre) enzyme that is able to recombine two 34 bp-long, palindromic DNA sequences referred to as 'loxP' sites, named after the locus of crossing-over (X-over) in P1 bacteriophages [166]. After Cre-mediated recombination, the genetic sequence between the loxP sites can be either removed or inverted, depending on the orientation of the loxP sequence.

Global deletion of a gene can often result in severely debilitating phenotypes or even death at an early developmental stage, making thus the study of a gene's function and phenotype difficult. For example, global cGKI-deficient mice are hypertensive (under distinct experimental conditions) and display severe intestinal abnormalities, resulting in death at 3 to 6 weeks after birth [63]. To overcome this obstacle, a controlled genetic modification both in time and space (known as spatiotemporal control) is often desirable. To achieve the spatial control, tissue-specific promoters driving expression of Cre can be utilised, and ensure in that way a tissue-specific ablation of genes. To add temporal control of Cre expression along with its spatial control, Feil *et al.*, conceived a sophisticated method, which is nowadays globally used. They fused Cre recombinase with a mutated oestrogen receptor ligand-binding domain, which can be activated by the synthetic drug 4-hydroxytamoxifen (4-OHT), but not by endogenous oestrogen. The resulting Cre-ER^{T2} construct can be combined with essentially any tissue-specific promoter and allows for a precise control of the onset of recombination both in time and space [167-169]. Today, numerous Cre lines (known as 'Cre-zoo') with tissue-specific promoters are available for purchase facilitating in vivo research. Here, to analyse Cre expression, various fluorescent or LacZ Cre-reporter mice have been developed [170-172]. Most of these transgenes are specifically targeted into the Rosa 26 locus, located on the murine chromosome 6. The Rosa 26 locus presents a popular, widely-used locus in the murine genome, as it offers stable and ubiquitous expression the transgenes inserted in there [171].

A.7 Imaging techniques that boost scientific research

A.7.1 PET

PET is a powerful imaging technique particularly used in the clinics but also quite often applied for imaging studies with genetically modified mice. For that reason, dedicated small-animal PET scanners are utilised, which provide sufficient resolution and sensitivity for small-animal studies [173-176]. PET imaging relies on the usage of radioactive, positron-emitting isotopes that are incorporated into tracer molecules like organic compounds [177]. For instance, ^{18}F (with a half-life of 110 min) is commonly incorporated into glucose and injected into the animal via the tail vein, from where it is taken up by the tissues according to its pharmacokinetic and pharmacodynamic properties. After administration to the subject, radioactive decay of the isotope leads to the emission of a positron, which spontaneously recombines with an electron from the surrounding tissues. This recombination process (termed annihilation) yields two 511 keV γ-rays travelling into opposite directions, which are then detected by the PET scanner (**Figure 7**). After perception of a sufficient number of such γ-rays, the software reconstructs a three-dimensional image of the distribution and concentration of the PET tracer within the animals' tissues. In that way, the researcher is able to observe biochemistry in vivo in a non-invasive manner and in real-time. PET technology also enables the extraction of valuable information about a tissue's metabolic activity, or the global distribution of the PET tracer inside the body [178].

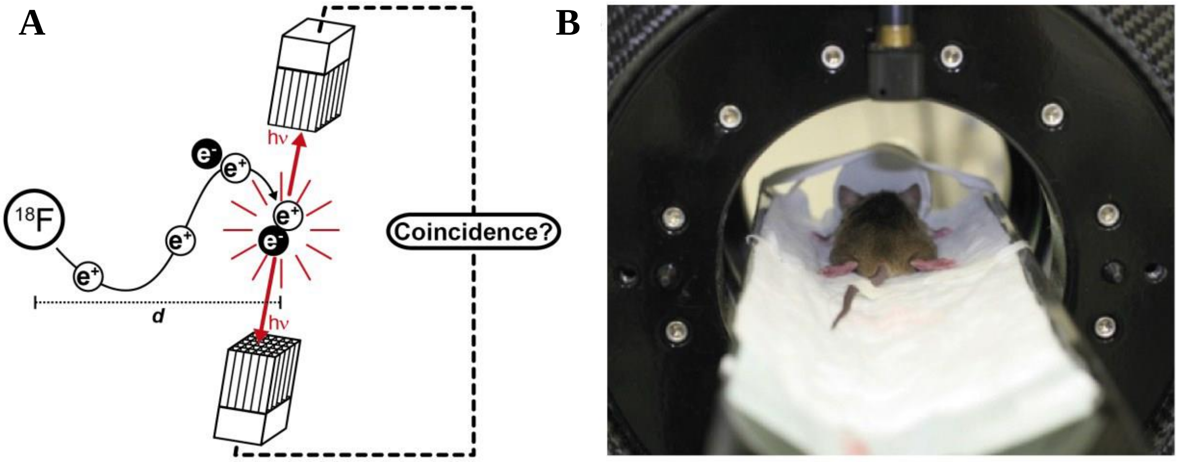

Figure 7. Working principle of PET.

A) Schematic representation of the working principle of a PET scanner. Radioactive decay of ^{18}F leads to emission of a positron (e^{+}) that travels through the tissue while losing energy until it approximates an electron (e^{-}). Both recombine in an annihilation reaction, yielding two γ-photons. Photons move into opposite directions and are detected by the PET scanner located around the subject. The scanner records events when two photons are coincidentally registered by detectors on opposite sides. *d* is the distance between the initial position of the radiolabelled tracer and the electron-meeting spot, where the annihilation reaction took place. B) Real image depicting an anaesthetised mouse placed on the bed of a small-animal PET scanner (Taken from [179]).

A.7.2 Live-cell imaging of cGMP levels using biosensors

End-point assays such as enzyme-linked immunosorbent assay (ELISA) or radioimmunoassays have been conventionally utilised to determine cGMP amounts in cells and tissues [180, 181]. However, the drawback of these techniques lies in the fact that they can only be performed in fixed cells or tissues, thus only providing end-point information, without a high temporal resolution of the dynamic processes happening in cells. [181, 182]. In recent years, live-cell microscopy has excelled and as a result, numerous biosensors have been developed for the visualisation of the spatiotemporal dynamics of signalling molecules in living cells and animals [183, 184].

Recently, a FRET-based cGMP biosensor, which was originally created by the Russwurm laboratory [185], was rearranged in a highly sophisticated manner by the Feil laboratory. The newly-configured cGMP biosensor enables the real-time assessment of cGMP levels with high spatiotemporal resolution in living cells, tissues, and mice [184]. In more detail, Thunemann and Wen *et al.* combined the FRET-based cGMP sensor with an EC_{50} of 500 nM (referred to as cGi500) (**Figure 8**) [185] with an existing double-fluorescent reporter mouse line (R26-mT/mG) [170]. The resulting construct encompassed a “floxed” tdTomato fluorescent protein (mT) upstream of the cGi500 cGMP biosensor. After Cre-mediated excision of the mT construct, the cGi500 can be expressed in tissues, depending on the Cre-line’s tissue specificity. The cGi500 cGMP biosensor is a ratiometric sensor whose working principle relies on the FRET phenomenon, firstly described by Theodor Förster in 1948 [186]. The sensor comprises the cGMP-binding domains of cGKI flanked by a cyan and yellow fluorescent protein (CFP and YFP). Without bound cGMP the two fluorophores are located in close proximity, allowing therefore for radiationless energy transfer from CFP (FRET donor) to YFP (FRET acceptor). However, cGMP binding to cGi500 induces a conformational change moving the two fluorophores apart and, thus, reducing FRET efficacy. An electron-multiplying charge-coupled device (EM-CCD) camera simultaneously records the emission of the YFP fluorophore at 535 nm and CFP fluorophore at 480 nm, which has been previously excited with a wavelength of

445 nm. Upon application, for instance, of a cGMP-elevating drug, transient elevation of cGMP provokes the reduction of YFP emission, while leading to elevation of CFP emission (**Figure 8**) [184]. Ultimately, the computed ratio of the CFP/YFP emission can be perceived as a measure of FRET efficiency, and indirectly, as a proxy for the intracellular cGMP levels.

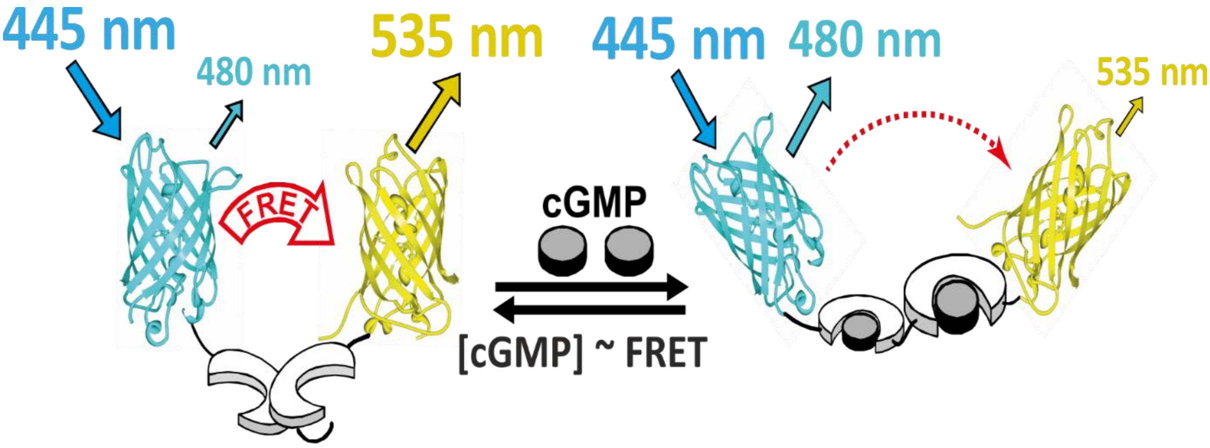

Figure 8. Working principle of the FRET-based cGMP biosensor cGi500.

cGi500 is a ratiometric cGMP biosensor consisting of the cGMP-binding domain of bovine cGKI flanked by two fluorophores; CFP and YFP. The left image depicts the cGi500 sensor when no cGMP is bound on it. In that state, FRET occurs with maximal efficiency, meaning that excitation of the sensor with a wavelength at 445 nm, results in an increased emission of the YFP at 535 nm. The right image shows the cGMP-bound state of the sensor. cGMP causes a conformational change of the sensor responsible for shifting CFP and YFP apart. In that case, FRET is no longer able to occur with high efficiency leading to the reduction of light emission of YFP at 535 nm, and the increase of emission of CFP at 480 nm. The emission ratio of both fluorophores at 480 nm and 535 nm (F480/F535) is used as a measure of FRET efficiency, and indirectly represents the intracellular cGMP levels. (Taken from [184]).

A.8 Aim of this work

The influence of the cGMP signalling pathway in the cardiovascular and neuronal system has long been established [187]. Recent data in our laboratory implicate cGMP signalling and in particular the cGMP-dependent protein kinase I (cGKI) in cold-stress induced thermogenesis occurring in BAT (unpublished data). BAT, in turn, has received a vast amount of attention in the last decades due to its very promising role in combating obesity and related comorbidities in western societies, as it can combust lipids to generate heat.

In the present project, we sought to investigate the role of cGKI in thermogenesis in mice. For that reason, we used a Nes-Cre line to conditionally ablate cGKI from the central and peripheral nervous system and exposed these mice to a cold-stress challenge. We then determined different body parameters as well as hormones and proteins involved in thermogenesis. We also performed extensive tissue analyses via the help of fluorescence microscopy.

In the course of this work we posed ourselves the following questions and designed experiments to help us answer them:

1. What is the localisation of cGKI in the tissues related to thermogenesis?
2. How does body temperature of control and mutant mice behave under cold-stress?
3. How does the body weight of control and mutant mice change longitudinally?
4. Is there a change of noradrenaline in BAT of these animals?
5. What are the expression levels of thermogenesis-related proteins in BAT?
6. What kind of cells that exist in BAT, might be implicated in cGMP-regulated thermogenesis?

B. Materials and Methods

B.1 Materials

B.1.1 Reagents and equipment

Devices and their specifications will be described accordingly in relevant experimental procedures. However, a list of all devices and equipment, as well as the supplying company is located in the appendix (p. 98). When mentioned in this section, centrifugation steps have been carried out with an Eppendorf 5417C/R centrifuge (Eppendorf AG, Hamburg, Germany) for small 1.5 and 2 mL reaction tubes and with an Eppendorf 5804R centrifuge with an A-4-44 rotor for larger 15 and 50 mL tubes. All chemicals and reagents were obtained from Carl Roth (Karlsruhe, Germany) unless otherwise stated. Reagents purchased from other companies are listed in the appendix (p. 98). Surgical instruments were purchased from Fine Science Tools (Heidelberg, Germany).

B.1.2 Commonly utilised solutions and buffers

Solutions and buffers were prepared with double deionised ultrapure water ddH_2O (Milli-Q Integral Water Purification System, Massachusetts, USA), if not stated otherwise. Per cent concentrations of liquid reagents are expressed as volume per volume (v/v). For solid reagents, they are given as weight percentage (w/v) and are expressed as mass per volume (with x (% concentration) = g (reagent mass) /100 ml). To adjust pH where necessary, 1 N NaOH or 1 N HCl were used. Recipes and storage conditions for commonly used solutions and buffers are presented below. Specific solutions and buffers needed for selected experiments throughout this project are presented in the according sections. Solutions were sterilised in an autoclave for 20 min at 121 °C (Ventilab 3000, Munich, Germany) unless otherwise stated.

- **0.5 M EDTA pH 8.0:** Dissolve 186.1 g disodium ethylenediaminetetraacetic acid dihydrate ($Na_2EDTA \times 2\ H_2O$) in 800 ml H_2O. EDTA will be dissolved after pH is adjusted to 8.0 by addition of NaOH pellets. Fill up with ddH_2O to 1 L, sterilise via autoclaving and store at RT.

- **10x TBE buffer:** 0.5 M Tris (108 g/L), 0.5 M boric acid (55 g/L), and 10 mM 0.5 M EDTA pH 8.0 (20 ml/L). Fill up with ddH_2O to 1 L and store at RT.

- **10x TE pH 8.0:** 100 mM Tris-Cl (100 ml/L 1 M Tris-Cl pH 8.0), 10 mM EDTA (20 ml/L 0.5 M EDTA pH 8.0), autoclave and keep at RT.

- **PBS pH 7.4:** 135 mM NaCl (7.89 g/L), 3 mM KCl (0.22 g/L), 8 mM Na_2HPO_4 (1.42 g/L $Na_2HPO_4 \times 2\ H_2O$), 2 mM KH_2PO_4 (0.27 g/L), ddH_2O to 1L, adjust pH to 7.4 with HCl or NaOH, autoclave and store at RT for future use.

- **1 M Tris-HCl pH 8.0:** Dissolve 121.14 g Tris in 1 L ddH_20, adjust pH to 8.0 with HCl, autoclave and store at RT.

- **10x TBS pH 8.0:** 100 mM Tris (12.11 g/L), 1.5 M NaCl (87.66 g/L), add ddH_2O to 1 L, adjust pH to 8.0 with HCl and store at RT for future usage.

- **TBS-T:** 100 ml 10x TBS, 0.1% Tween-20 (1 ml/L), ddH_20 to 1 L.

B.2 Mice and cell culture

B.2.1 Maintenance and breeding of mouse lines

Mice used in this project were housed and bred in the animal facility of the Interfaculty Institute of Biochemistry (IFIB, Tübingen, Germany) under standard conditions; ambient temperature: 20-22 °C, relative humidity: 50-55%, at a 12 h lights-on /12 h lights-off cycle. Single animals or groups of mice of the same gender were caged in Makrolon® standard cages type II (375 cm^2 for up to 3 mice) or cages type III (820-840 cm^2 for up to 8 mice), and had access to tap water and standard rodent chow (Altromin Spezialfutter GmbH & Co. KG, Lage, Germany and Sniff Spezialdiäten GmbH, Soest, Germany) *ad libitum*. For breeding, a singly-caged, reproductively-mature male mouse (aged $\geq$ 6 weeks) was placed together with 1-2 reproductively-mature female mice (age $\geq$ 8 weeks) in a type II cage. Prior to delivery, females were separated from males and transferred to a clean type III cage containing nesting material (Nestlets', Emsicon-Jung GmbH, Forstinning, Germany) and dedicated breeding chow (Sniff). Three weeks post-delivery, offspring were numbered by ear-tagging in accordance to the 'universal mouse numbering system' and then placed in fresh cages singly or in groups of the same sex. The ear biopsy obtained during the ear-punch was further used for routine PCR-based genotyping as described in **B.2.3**.

B.2.2 Nomenclature of mouse lines

Nes-Cre mice were generated by Rüdiger Klein and express Cre recombinase under the control of the rat Nestin promoter and enhancer [188]. The transgene insertion is random but analyses have located it on mouse chromosome 12. In this project, male hemizygous transgenic mice (Nes-$Cre^{tg/+}$) on a C57BL/6J background were used for breeding.

For the creation of cGKI-mutant mice, the exon 10 (responsible for the catalytic activity of the kinase) was flanked by two loxP sites (L2 allele). Excision of exon 10 from the L2 allele by Cre-mediated recombination of the loxP sites produces an L1 allele [60].

cGKI-brain KO mice (Nes-Cre$^{tg/+}$ x cGKI$^{L1/L2}$) and their corresponding control mice (Nes-Cre$^{tg/+}$ x cGKI$^{+/L2}$) were generated by mating a male Nes-Cre$^{tg/+}$ x cGKI$^{+/L1}$ with a female Nes-Cre$^{+/+}$ x cGKI$^{L2/L2}$ mouse.

Nes-Cre$^{tg/+}$ x R26-mT/cGi500$^{+/L2}$ or Nes-Cre$^{tg/+}$ x R26-Ai14$^{+/L2}$ mice were obtained by mating a male Nes-Cre$^{tg/+}$ mouse with a female R26-mT/cGi500$^{+/L2}$ [184] or R26-Ai14$^{+/L2}$ [172] mouse, respectively. R26-mT/cGi500(L1) mice, with a global expression of the cGi500 sensor, were generated as described in [184].

Npr2-LacZ mice had been generated by placing the LacZ gene in exon 1 of the Npr2 gene [189]. Npr2-LacZ x R26-cGi500(L1) were obtained by crossing an Npr2-LacZ mouse with a mouse that expresses the cGi500 globally.

B.2.3 Genotyping of mouse lines

Routine polymerase chain reaction (PCR) was performed to genotype mice. DNA was isolated from ear biopsies via overnight lysis at 55 °C. The identification of mutant or wild type mice relied on the presence or absence of specific amplicons upon visualisation of the PCR products on a 2% agarose gel. Reagents, buffers and the procedure are described below:

- **10x reaction buffer S:** 100 mM Tris-Cl pH 8.8, 500 mM KCl, 0.1% Tween-20, 15 mM $MgCl_2$ (PEQLAB), stored at -20 °C.
- **Proteinase K:** 50 mg/ml proteinase K in 1x TE, stored at -20 °C.
- **10x RT buffer:** 100 mM Tris-Cl pH 8.0 (1 ml 1 M Tris-Cl pH 8.0), 500 mM KCl (5 ml 1 M KCl), 15 mM $MgCl_2$ (0.15 ml 1 M $MgCl_2$), 2 mM of each dNTP (0.2 ml of each 100 mM dATP/dGTP/dCTP/dTTP), 3.65 ml ddH_2O. Store in 0.5 ml aliquots at -20 °C.
- **dNTPs:** 100 mM dATP, 100 mM dCTP, 100 mM dGTP, 100 mM dTTP (PEQLAB).
- **Primers:** dilute initial stock (100 µM) to 25 µM with ddH_2O, stored at -20 °C.
- **Taq polymerase:** (Bioron), stored at -20 °C.
- **6x loading dye:** add 0.125% (5 ml) bromophenol blue, 0.125% (6 mg) xylene cyanole, 40% (2 g) sucrose and 1x TBE to 50 ml.

1. Incubate ear biopsies in PCR lysis buffer at 55 °C overnight (50 µl lysis buffer/ ear biopsy; composition: 5µl 10x reaction buffer S, 1 µl Proteinase K and 44 µl ddH_2O).
2. On the next day, briefly vortex samples and centrifuge for 5 min at 13,000 rpm.

3. Transfer the supernatant into a new 0.5 ml PCR tube.
4. Inactivate proteinase K by heating up to 95 °C for 15 min.
5. Pipette 3 µl of the DNA-containing solution into new 0.5 PCR cups, store the remaining at -20 °C for future usages.
6. For PCR, prepare a PCR master mix that contains (per reaction) 2.5 µl 10x RT buffer, 0.3 µl of each primer (see Table 1, p. 101) 0.2 µl Taq polymerase and ddH_2O to 22 µl.
7. Dispense 22 µl of the master mix each time to PCR tubes that have been pre-loaded with 3 µl of the DNA. Always remember to prepare a positive (with DNA of known genotype) and a negative (with no DNA added) control.
8. Mix tubes well, spin down briefly, make sure the PCR mixture is at the bottom of the tube.
9. Run the respective PCR programme (see Table 1, p. 101).
10. After completion of the programme, add 5 µl of 6x loading dye to each tube and mix well.
11. Load 12 µl onto a 2% agarose gel and run at 130 V for about 1 h.
12. Visualise bands with an appropriate imaging device and document results.

Respective PCR programmes, primer sequences and PCR product sizes for each transgenic mouse line are to be found in Table 1 and 2 of the Appendix (p. 101-102).

B.2.4 Cell culture of primary BAT and adrenal gland cells

Over the last decades, primary cell cultures have become a valuable tool in everyday research. Directly isolated from the desired organs, they provide excellent means for every research field, as they resemble the "*close-to-native*" situation, as opposed to the permanent cells lines, which have undergone immortalising mutations allowing for their capability of continuous expansion. Primary cells are therefore a valuable tool to investigate complex cellular mechanisms such as signal transduction pathways. Here, to shed more light into the biochemistry of the cGMP signalling pathway in BAT and adrenal gland, we utilised mice expressing the FRET-based cGMP biosensor under the action of Nes-Cre recombinase.

B.2.4.1 Isolation of primary cells

Mice used for cell culture experiments were euthanized and BAT and adrenal glands were rapidly removed and placed in ice-cold PBS. Fat around the tissues was detached with fine scissors under a binocular microscope. Cells isolated enzymatically from these organs were cultivated on 12 mm coverslips in a 24-well plate under standard conditions (37 °C, 5% CO_2) in Dulbecco's modified eagle medium (DMEM) supplemented with 10% fetal calf serum (FCS) and penicillin/streptomycin (all purchased from Life Technologies). Medium change was performed once on day 3. Cell growth and prosperity were monitored daily under a microscope (Zeiss, Axiovert 40C) and representative images of the cells were acquired with a SONY Cyber-shot VX DSC-W17 which bore an ocular adaptor. On day 7, coverslips were removed from the multi-well plate and subjected to FRET-based cGMP measurements.

- **10 mg/ml Collagenase:** Dissolve 100 mg collagenase (Sigma-Aldrich) in 10 ml Ca^{2+}-free medium. Store in 0.5 ml aliquots at -20 °C.
- **10 mg/ml Hyaluronidase:** Dissolve 100 mg hyaluronidase (Sigma-Aldrich) in 10 ml Ca^{2+}-free medium. Storage in 0.5 ml aliquots at -20 °C.
- **100 mg/ml BSA:** Dissolve 0.5 g BSA in 5 ml Ca^{2+}-free medium and sterilise by filtration. Store in 0.5 ml aliquots at -20 °C.
- **100 mg/ml DTT:** Dissolve 0.5 g dithiothreitol (DTT) in 5 ml Ca^{2+}-free medium. Sterilise by filtration, and store in 0.5 ml aliquots at -20 °C.
- **7 mg/ml Papain:** Dissolve 100 mg papain (Sigma-Aldrich) in 14.29 ml Ca^{2+}-free medium. Store in 0.5 ml aliquots at -20 °C.
- **Ca^{2+}-free medium (pH 7.4):** 85 mM Na L-glutamate (15.91 g Na L-glutamate monohydrate), 60 mM NaCl (3.51 g), 10 mM HEPES (2.38 g), 5.6 mM KCl (0.42 g), 1 mM $MgCl_2$ (0.20 g $MgCl_2$ x 6 H_2O), ddH_2O to 1 L. Adjust pH to 7.4 with HCl, autoclave, and store at 4 °C. Warm up to 37 °C right before use.
- **Cell culture medium:** Add 50 ml FBS and 5 ml of 100x Pen/Strep to 500 mL DMEM, store at 4 °C. Warm up to 37 °C before use.
- **Enzyme working solution A:** 0.7 mg/ml papain (100 µl of 7 mg/ml papain), 1 mg/ml DTT (10 µl of 100 mg/ml DTT), 1 mg/ml BSA (10 µl of 100 mg/ml BSA). Fill up with 880 µl Ca^{2+}-free medium. Always prepare shortly before use and warm up to 37 °C in a water bath.
- **Enzyme working solution B:** 0.5 mg/ml collagenase (50 µl of 10 mg/ml collagenase), 0.5 mg/ml hyaluronidase (50 µl of 10 mg/ml hyaluronidase), 1 mg/ml BSA (10 µl of 100 mg/ml BSA). Fill up with 890 µl Ca^{2+}-free medium. Always prepare shortly before use and warm up to 37 °C in a water bath.

1. Euthanize mouse with CO_2 and harvest BAT or adrenal gland in ice-cold PBS. One BAT usually yields ~2.5-3 m cells and is sufficient for 8-10 wells of a 24-well plate. Adrenal gland yield is much lower than that of BAT, and therefore 3-5 mice have to be utilised for an adrenal gland cell culture. Typically a pair of adrenal glands yields ~200,000 cells that can be seeded on 2 coverslips of a 24-well plate of 100,000 cells each.
2. Free tissues from excess surrounding fat under a binocular microscope with fine scissors.
3. Prepare enzyme working solution A and B and warm up in advance at 37 °C in a water bath.
4. Mince tissues with fine scissors and transfer to a 1.5 ml-reaction tube containing 1 ml of enzyme working solution A (for 1 BAT or for 2 adrenal glands).
5. Incubate tissues at a 37 °C water bath (1 h for BAT, 20 min for adrenal glands). Invert tubes periodically to aid digestion.
6. Briefly centrifuge tubes at 3000 rpm for 5 min at RT.
7. Discard supernatant carefully and replace with 1 ml warm enzyme solution B.

8. Incubate at 37 °C for 15 min. Every 3 min pipette up and down to mechanically assist digestion, until at the end no big tissue fragments are left in the tube.
9. Transfer cell suspension into a fresh 15 ml falcon tube and add 4 ml of pre-warmed cell culture medium to stop the digestion.
10. Centrifuge for 8 min at 3000 rpm to pellet cells. Then discard supernatant carefully avoiding any disruption to the pellet, and thus loss of cells.
11. Resuspend the pellet in 1 ml warm cell culture medium.
12. To count the cell number, mix 18 µl of cell suspension with 2 µl of trypan blue, which stains dead cells.
13. Count viable cells in a Neubauer chamber under a microscope. Count all 4 large corner squares (V = 0.1 µl) consisting of 16 small squares each and calculate the mean of the 4 large squares. The cell number is then given by the formula: cell number = average cell number of 4 large squares x 10^4 x volume of cell suspension.
14. Seed cells in pre-warmed cell culture medium in a 24-well plate at a density of:
    i. 200,000- 300,000 cells/ well of a 24-well plate for BAT cultures, and
    ii. 100,000- 200,000 cells/ well of a 24-well plate for adrenal gland cultures.
15. Monitor cell growth and prosperity daily under a microscope. Perform medium change once on day 3 and let cells grow to at least 80% confluency before FRET imaging on day 7.

B.2.5 In vivo analysis of mouse lines

B.2.5.1 Body weight analysis of Nes-Cre mouse lines

To investigate the influence of the Nes-Cre transgene on body weight, mice of both sexes and different genotypes were weighed weekly over a period of 13 weeks. Nes-Cre mice [188] display a mild hypopituitarism due to the enhancing elements of the Nes-Cre transgene [190]. To rule out the possibility that body weight confounds our cold-stress response results, we analysed the body weight of Nes-Cre mice that were crossed with a “floxed” cGKI mouse line.

1. Body weight measurements were performed weekly in the animal facility of the interfaculty institute of biochemistry 1 h after lights off.
2. The use of a fine-scale is mandatory throughout the experiment.
3. Place a clean plastic beaker on the scale and tare it.
4. Transfer each mouse in the beaker, wait a few seconds until it calms and note down its weight. Transfer the mouse back to its cage.
5. Repeat the procedure with all the mice to be weighted. At regular points, clean the beaker with 70% ethanol and a paper towel.

B.2.5.2 Cold-stress assay

Exposure to cold at 4 °C is able to trigger a unique hypothalamic pathway that instead of activating the pituitary-adrenal gland-axis, leads to heat production through BAT. Since mice are housed at ~21 °C, which is well below their thermoneutrality zone at 30 °C, they are under constant cold-stress [121, 122]. Prolonged exposure to cold activates non-shivering thermogenesis occurring in BAT. Acute cold exposure, as that performed in the experiments at 4 °C, rapidly initiates heat production in BAT. Cold-stress experiments have been used to assay the functionality of BAT and possible deficits in thermoregulation. We stressed male and female cGKI-brain KO and control mice for a variable amount of time, and monitored their body temperature rectally every hour. One day before the experiment mice were caged individually. One hour before as well as during the experiment bedding and food was removed of the cage. Food withdrawal was implemented in order to exclude confounding effects through food-induced thermogenesis [191, 192]. At the end of each experiment, mice were decapitated and tissues of interest were harvested for further analyses.

1. Well before the experiment, weight-match experimental and control animals.
2. Maintain mice individually in single cages one day prior to the experiment, with food and water *ad libitum*. Transfer cages to a quiet room, where no other researchers or animal caretakers enter. Care should be taken to avoid inducing excess stress to the animals.
3. On the day of the experiment, remove food, water, and bedding 1 h before the start, and transfer the cages into the 4 °C cold room in 15 min intervals.
4. Measure the body temperature rectally with the use of a digital thermometer. Insert the thermometer probe 5 mm deep into the rectum and monitor the temperature after 2-3 sec. when the animal has calmed down. Marking the probe with a pen will ensure identical probe insertion in each experimental animal.
5. At the end of the experiment, instantly decapitate the mouse with large scissors.
6. Excise and cut BAT into halves. Free from surrounding fat and weigh both halves. Fix one half for 2 h in 4% PFA/PBS in ice for immunological staining and snap freeze the other half in liquid nitrogen for noradrenaline ELISA or Western blot. Store samples at -80 °C until further processing.
7. Later on, harvest the adrenal glands and WAT, and freeze away after having weighed them. Store at -80 °C until needed.
8. Obtain a tail-tip piece for re-genotyping.
9. Proceed with the next mouse as before.

B.3 Ex vivo analysis of tissue samples

B.3.1 Histological methods

B.3.1.1 Preparation of tissues for paraffin and cryosectioning

Tissue sectioning and subsequent staining with antibodies or specific dyes is a widely-applied technique in biochemistry and enables thorough scrutiny of the (sub)-cellular characteristics of a given tissue. A critical step in tissue preparation for either paraffin or cryo embedding is undoubtedly the fixation. Its role is to terminate all biochemical processes occurring in the cell, and at the same time to disable microorganisms around it, which otherwise would degrade tissue. Thus, by inactivating enzymes that could ultimately lead to cell degradation via autolysis or proteolysis, fixation preserves cell morphology, close to the natural one. A lot of fixatives have been described; with the two most commonly utilised in the laboratory being formaldehyde and glutaraldehyde. Formaldehyde is usually sold as a 37% aqueous solution, where it exists as a hydrate called methylene glycol. Methylene glycol polymerises and forms an insoluble precipitate called paraformaldehyde [193]. 4% paraformaldehyde in phosphate-buffered saline (4% PFA/PBS) constitutes a wise choice for the most fixation purposes.

Later, in this part, two commonly-used techniques will be described: paraffin and cryosectioning. While both of them are very robust methods, each one encompasses advantages and disadvantages depending on the downstream application. Although paraffin sections usually retain a better preservation of the morphology of the tissue, these often require extensive fixation and labour processing. Cryosectioning, on the other hand, is less labour, does not necessarily require fixation, antigens are less masked, and also allows for finer sections. However, the necessary equipment (cryostat) is usually more expensive than the one needed for paraffin sections.

B.3.1.1.1 <u>Paraffin sections</u>

To prepare tissues for paraffin embedding and subsequently sectioning, the downstream application has to be considered in advance, in order to choose the most appropriate fixative. For paraffin sections, both glutaraldehyde and formaldehyde can be used without any major problems. Nevertheless, fixation conditions need to be adjusted to the specimen characteristics (size, thickness, shape) [194]. For example, incomplete fixation (under fixation) may lead to rapid proteolytic degradation of the target proteins, thus compromising specific antibody binding to the epitope. Excessive fixation (over fixation), in contrast, may cause severe protein-protein crosslinks that will eventually render epitopes completely inaccessible to antibodies.

- **4% paraformaldehyde in PBS (4% PFA/PBS):** weigh 20 g of paraformaldehyde, add ddH_20 to 500 ml. Slight stirring while heating may help dissolve PFA. Use directly or aliquot and store at -20 °C.

- **Cell fix:** 2% formaldehyde (27 ml of 37% aqueous solution of formaldehyde), 0.2% glutaraldehyde (4 ml of 25% glutaraldehyde), add PBS pH 7.4 to 500 ml.

1. Euthanize mice and harvest the desired organs in ice-cold PBS.
2. Fix organs for 2 h with a sufficient amount of the appropriate fixative depending on your downstream application. Fixation time may require adjustment according to the tissue size.
3. Wash tissues 3 x 10 min in PBS to ensure adequate fixative removal.
4. Dehydrate tissues in a series of aquatic solutions of increasing alcohol concentration:
    - 60% ethanol/ddH_2O at RT for 1 h
    - 70% ethanol/ddH_2O at RT for 1 h
    - 80% ethanol/ddH_2O at RT for 1 h
    - 90% ethanol/ddH_2O at RT for 1 h
    - 2 x 100% ethanol at RT for 20 min
    - 2 x 100% toluene at RT for 20 min
5. Pass tissues through 3 changes of liquid paraffin (Paraplast®X-TRA, Roth) at 57 °C. Allow tissues to completely soak into paraffin for at least overnight.
6. Embed tissue in fresh liquid paraffin using an embedding system that consists of a metallic cassette and a plastic mould.
7. After paraffin has hardened, tissues can be either directly processed or stored at RT until sectioning.
8. Section the tissue with a microtome (HM335E, MicromInternational) at a 10 µm thickness.
9. Allow paraffin sections to flatten out in a warm water bath. Water temperature should not exceed 40 °C to avoid paraffin melting.
10. Mount paraffin sections on a poly-L-lysine coated glass slide (Polysine™, *Menzel-Gläser*), by carefully placing the slide into the water bath, underneath the floating paraffin section. Allow sections to dry overnight at RT or for a few hours at 37 °C.
11. To further proceed with the histological staining of the paraffin sections, these require initially to be deparaffinised and rehydrated.

Deparaffinisation and rehydration of paraffin sections

1. Immerse sections 2 times in 100% toluene for 10 min at RT to remove paraffin.
2. Rehydrate tissues in a series of aquatic solutions of decreasing alcohol concentration:
    - 2 x 100% ethanol at RT for 5 min
    - 90% ethanol/ddH_2O at RT for 5 min
    - 80% ethanol/ddH_2O at RT for 5 min

  - 70% ethanol/ddH_2O at RT for 5 min
  - 60% ethanol/ddH_2O at RT for 5 min
3. Wash slides in PBS for immunohistochemical staining or in dH_2O for Haematoxylin-Eosin staining for 5 min at RT.
4. Proceed with staining as described in B.3.2

B.3.1.1.2 Cryosections

Sections of frozen tissue were used in this project to reveal cellular (co-) localisation of proteins of interest by means of immunofluorescent staining. Tissue harvest remains similar as in paraffin sections preparation. Fixation was routinely accomplished with 4% PFA, as other fixation buffers containing glutaraldehyde should be avoided because they increase tissue's background autofluorescence.

1. Euthanise mice and harvest organs in ice-cold PBS.
2. Fix organs for 2 h with a sufficient amount of 4% PFA/PBS. Fixation time should be adjusted depending on tissue size.
3. Wash tissues 3 x 10 min in PBS to remove fixative residues.
4. Cryoprotect tissues in 30% sucrose at 4 °C, overnight.
5. Place tissues in self-made aluminium moulds, fill in with Tissue-Tek® O.C.T compound (Sakura Finetek) and allow them to freeze down in a Styrofoam box containing dry ice.
6. Once the Tissue-Tek has hardened, tissue can be either processed directly or stored at -20 °C until sectioning.
7. Frozen tissue sections were made with a cryostat (HM525, *MicromInternational*) at a 10 µm thickness and mounted on appropriate slides (SuperFrostPlus® for all other tissues and SuperFrostPlus® Gold for BAT sections, *Menzel-Gläser*).
8. Dry slides at 37 °C for a few hours before immunofluorescent staining or store at -20 °C.

B.3.2 Immunohistochemistry

To explore the localisation of cGKI in murine BAT, we performed immunohistochemistry on deparaffinised and rehydrated tissue sections. Citrate buffer was implemented to unmask crosslinked epitopes generated by the fixation with aldehydes. The primary antibody against cGKI was incubated overnight at 4 °C in a humidified chamber. A secondary biotinylated antiserum was then used, raised against the host species of the primary antibody. The immunoreaction of the primary antibody was amplified by the addition of a preformed avidin-biotinylated horseradish peroxidase H complex (ABC complex; VECTASTAIN® Elite ABC Kit, *Vectorlabs*) [195]. Finally, the signal was made visible by incubating the slides with 3,3'-

diaminobenzidine (DAB), a chromogenic substrate that is converted to a brown insoluble dye by horseradish peroxidase. When mouse primary antibodies were utilised, unspecific binding of the secondary antibodies was blocked with the Vector Mouse on Mouse Kit (M.O.M.™ Kit, *Vectorlabs*).

- **Wash buffer:** TBS-T (see **B.1.2**)
- **Peroxidase blocking solution:** 300 µl of 30% H_2O_2, 130 µl of 10% Methanol/PBS, and 570 µl PBS pH 7.4.
- **Antigen retrieval solution pH 6.0:** 10 mM trisodium citrate dihydrate ($Na_3C_6H_5O_7$ x 2 H_2O), fill up with ddH_2O to 1 L, adjust pH to 6.0 with HCl.
- **Blocking solution:** 10% normal goat or donkey serum in wash buffer, depending on the host species of the secondary antibody.
- **Primary antibody solution:** For antibody dilutions see appendix (Table 3, p. 103). Primary antibodies were diluted in wash buffer, supplemented with 5% normal serum of the host species of the secondary antibody.
- **Secondary antibody solution:** Biotin-conjugated antiserum against the host species of the primary antibody, diluted 1:200 in wash buffer, supplemented with 5% normal serum of the host species of the secondary antibody. For antibody dilutions see appendix (Table 4, p. 103).
- **Vectastain ABC solution:** Mix together 10 µl solution A (avidin), 10 µl solution B (biotin-horseradish peroxidase H complex), and 480 µl PBS pH 7.4. Vortex briefly and incubate in the dark for 30 min at RT. Right before use, add 500 µl of wash buffer.
- **DAB staining solution:** Mix 800 µl of 0.1% 3,3’-diaminobenzidine (DAB) stock solution with 800 µl PBS. Add 1 µl of 30% H_2O_2. To prepare a 0.1% DAB stock solution, dilute 40 mg DAB in 40 ml PBS. Store at -20 °C.

1. Obtain 10 µm-thick paraffin sections. Deparaffinise, rehydrate and wash in PBS for 5 min at RT.
2. Block endogenous peroxidase activity by incubating slides in peroxidase blocking solution for 20 min at RT.
3. Wash slides in PBS for 5 min.
4. Perform antigen retrieval by incubating slides in a plastic container filled with antigen retrieval solution for 15 min at RT. Then transfer the container into a microwave, bring buffer to boiling and finally allow it to cool down at RT.
5. Briefly wash slides in wash buffer for 5 min at RT.
6. Minimise unspecific binding of secondary antibody by incubating slides with blocking solution (approximately 500 µl of blocking solution per slide) for 2 h at RT.
7. Discard blocking solution and draw barriers around the sections with a hydrophobic marker.
8. Apply the primary antibody solution (approximately 500 µl per slide). Incubate at 4 °C overnight in a humidified chamber. Always remember to dedicate a few tissue sections as a negative control, to determine background noise. Merely replace the first antibody in that instance with just blocking buffer.

9. On the next day, collect and save the primary antibody. Wash slides in wash buffer 3 times for 10 min at RT.
10. Add the appropriate biotinylated secondary antibody solution and incubate for 1 h at RT.
11. Prepare a sufficient amount of Vectastain ABC solution and incubate for 30 min at RT in the dark.
12. Discard secondary antibody and wash slides in wash buffer 3 times for 10 min at RT.
13. Apply the Vectastain ABC solution onto the sections (approximately 500 µl per slide) and incubate for 30 min at RT.
14. Discard the ABC solution and wash slides in wash buffer 3 times for 10 min at RT.
15. Add DAB staining solution onto the slides (approximately 500 µl per slide) and monitor colour development closely.
16. Once the brown hue of the desired intensity has been developed, immerse slides into dH_20 to terminate the colouring reaction.
17. Counterstain nuclei with Hoechst 33258 (0.1% in wash buffer) for 15 min at RT.
18. Wash slides in dH_20 for 5 min.
19. Mount cover glasses with Aquatex®, mounting agent (*Merck*) and allow them to dry for a few hours at RT in the dark.
20. Analyse staining under a microscope capable of acquiring bright-field images.

B.3.3 Immunofluorescent staining

Immunofluorescent staining remains a powerful, versatile method, which is routinely carried out in research and diagnostic laboratories. It aids in detection and visualisation of diverse protein complexes or the DNA in tissue sections or cells [196]. It makes use of fluorophore-labelled secondary antibodies, which can be easily raised against the conserved Fc portion of the host species of the primary antibody. Simply put, for instance, the commonly used goat anti-rabbit AlexaFluor488 secondary antibody has been produced in the goat, against the conserved Fc domain of a rabbit antibody. Additionally, it bears a fluorophore able to absorb light at a max. of 488 nm and to emit in the green spectrum. This technique allows for the visualisation of a plethora of primary antibodies originating from the same species. In this project, immunofluorescence has been used to detect the expression of various proteins in BAT and the adrenal gland, and to correlate their localisation in regard to cGKI.

- **Wash buffer:** TBS-T (see **B.1.2**)
- **Blocking solution:** 5% normal goat or donkey serum in wash buffer, depending on the host species of the secondary antibody.
- **Primary antibody solution:** For antibody dilutions see appendix (Table 3, p. 103). Primary antibodies were diluted in wash buffer, supplemented with 5% normal serum of the host species of the secondary antibody.

- **Secondary antibody solution:** Alexa Fluor®-conjugated antisera against the host species of the primary antibody, diluted 1:500-1:1000 in wash buffer, supplemented with 5% normal serum of the host species of the secondary antibody (Table 4, p. 103).

1. Obtain cryosections of 10 µm thickness as described above.
2. Incubate slides for 5 min in PBS to remove O.C.T. residues from around the tissue.
3. Block unspecific binding sites by incubating with a sufficient amount of blocking solution for 1 h at RT.
4. Discard blocking solution and frame tissues with a hydrophobic barrier marker.
5. Incubate slides with the primary antibody solution at 4 °C overnight in a humidified chamber. Devote a few tissue sections as a negative control, to determine background noise. For that, replace the first antibody with blocking solution.
6. Wash slides 3 times for 10 min at RT with wash buffer.
7. Incubate slides with the secondary antibody solution for 1 h at RT.
8. Wash 2 times for 10 min with wash buffer.
9. Apply Hoechst 33258 (1:1000 in wash buffer) for 15 min at RT.
10. Wash sections 3 times for 10 min at RT.
11. Carefully mount cover glasses on slides with Shandon Immu-Mount (*Thermo Fisher Scientific*).
12. Allow slides to dry in dark at RT before proceeding with the microscopy.
13. Obtain high-quality images with an epifluorescent or confocal microscope that is equipped with the appropriate excitation and emission filters as well as with a high-resolution camera. Microscope setups used for this project are presented in section B.7.
14. Perform initial observation of the slide with low (~30 %) excitation light intensity, to avoid photobleaching of the tissue samples.
15. Before acquiring images, adjust excitation light intensity to higher levels (~80-100 %) and exposure time (usually 500- 1500 ms) depending on the intensity of the secondary fluorescently labelled antibody.

B.4 Protein analysis

B.4.1 Protein extraction from tissue samples

To explore and compare the expression levels of various proteins in BAT of control and mutant mice, total protein was extracted and assayed with antibodies. Harvested organs were snap-frozen by immersion in liquid nitrogen and either processed directly or stored at -80 °C for future use.

- **Protein lysis buffer:** containing 50 mM Tris-HCl pH 8.0 (500 µl of 1 M Tris-HCl pH 8.0), 100 mM NaCl (250 µl of 4 M NaCl), 5 mM EDTA (100 µl of 0.5 M EDTA), 2% SDS (1 ml of 20% SDS), and 1 protease inhibitor cocktail tablet (cOmplete Tablets, Mini *EASYpack*, ref.: 04693124001, *Roche*). Add 8150 µl ddH_20. Always prepare fresh right before use.

1. Pipette a sufficient amount of protein lysis buffer (300-500 µl per BAT, 2 adrenal glands) in a Fast Prep™ tube. Add a small quantity of sand, place the tissue on the sand, and at last the sphere, so that the tissue lies in-between.
2. Homogenise tissue in a Fast Prep®-24 instrument (MP Biomedicals) 2 times, for 20 sec (6.5m/sec).
3. Incubate at 94 °C for 5 min to denature protein.
4. Centrifuge at 14,000 rpm for 10 min at 4 °C.
5. Transfer the supernatant into a fresh 1.5 ml Eppendorf tube. Note down the volume.

B.4.2 Determination of total protein concentration

Total protein concentration was measured with the Lowry assay [197]. Under alkaline conditions, divalent copper (Cu^{2+}) reacts with the peptide bond causing its reduction to monovalent ion (Cu^+). In a second reaction, the reduced (Cu^+) and the aromatic residues of a protein (tyrosine, tryptophan, cysteine) react with the Folin-Ciocalteu reagent (a mixture of phosphotungstic acid and phosphomolybdic acid), causing its reduction and thus production of a molecule (molybdenum/tungsten) with an intense blue colour that absorbs light at 650 nm. The intensity of the colour is proportional to the amount of protein in a solution. Therefore, the total protein concentration in an unknown sample can be deduced by comparing the absorption of that unknown sample, to the absorption of a sample of known protein concentration (such as the BSA standard). The Lowry assay was carried out in triplicates in 96-well plates using the Micro-Lowry-Total-Protein Kit (ref. TP0300, *Sigma*). Tissue lysates were diluted 1:10 with ddH_20, before proceeding with the Lowry assay.

1. As protein concentration in initial lysate might be too high, make pre-dilutions of the lysates by pipetting 5 µl of tissue lysate into 45 µl of ddH_2O in an Eppendorf reaction tube (pre-dilution 1:10).
2. Add 5 µl of the pre-diluted tissue lysate in a 96-well plate and fill up with 95 µl ddH_20 (each sample in triplicate). Use 5 µl of protein lysis buffer (filled up to 100 µl with ddH_2O) as a negative control, and 100 µl of ddH_2O as blank.
3. Pipette 100 µl of each BSA standard (12.5, 25, 50, 100, 200, 400 µg/ml) into the 96-well plate.
4. Add 100 µl Lowry Reagent Solution to each well.
5. Use the microplate reader to briefly shake the 96-well plate, and incubate in the dark for 20 min at RT.

6. Add 50 µl Folin-Ciocalteu Phenol Reagent Working Solution to each well, briefly shake the 96-well plate in the microplate reader, and incubate in the dark for 30 min at RT.
7. Measure the OD at 650 nm with a microplate reader.
8. Generate the BSA standard curve (y-axis: OD_{650}, x-axis: µg protein/well) and calculate the protein concentration of the unknown samples.

B.5 SDS-PAGE and Western blotting

Sodium dodecyl sulphate-polyacrylamide gel electrophoresis (SDS-PAGE) is a technique commonly performed in the biochemical laboratory, to separate proteins by their molecular mass [198]. SDS, an anionic detergent, binds to proteins (at a ratio of 1.4 g SDS/ 1 g protein) and eliminates intrinsic protein charge, while the reducing agent β-mercaptoethanol, cleaves disulphide bonds, critical for proper protein folding. After the action of both, proteins abolish their tertiary and secondary structure (denaturation) and acquire negative charge, which makes their separation solely dependent on their molecular weight, as they travel along in the polyacrylamide gel towards the anode (positive pole). The procedure commences with the preparation of two polyacrylamide gels in a Mini-PROTEAN® 3 system (*Bio-Rad*): a 4% stacking gel which lies on top of an 8-12% resolving gel. Both have different pH values and thus, different, very important functions. The stacking gel takes advantage of the high electrical field zone created by the presence of the Cl^- and Glycine in it, and is used to "stack" all proteins in one tight band in between the Cl^- and Glycine, so that all proteins can enter the resolving gel virtually at the same time, making their migration truly a matter of their molecular size and not of any other possibly confounding factor. In the resolving gel, proteins migrate towards the positive pole only based on their molecular mass. Once electrophoresis has come to an end, proteins can be blotted on a Polyvinylidene fluoride (PVDF) membrane in a semi-dry manner with application of an electric charge. Membrane can be then used to detect proteins with specific antibodies (Western blotting).

In this project, gels were prepared with a thickness of 0.75 mm and 10 or 15 wells respectively, depending on the number of samples intended to load. After having determined protein concentration, this was adjusted to 5 µg/µl including 5x Lämmli sample buffer. Typically, 10-30 µg of protein were loaded onto the gel, after a short denaturation step at 95 °C for 5 min.

B.5.1 SDS-PAGE

- **5x Lämmli sample buffer:** 32% Tris pH 6.8 (3.2 ml of 1 M Tris pH 6.8), 40% Glycerol (4ml), 15% SDS (1.5 g), 0.1% Bromophenol blue (10 mg), 25% β-mercaptoethanol (2.5ml), fill up with ddH$_2$O to 10 ml. Aliquot and store at -20 °C.

- **4x Tris-SDS pH 6.8:** 0.5 M Tris (3.02 g), 0.4% SDS (0.2 g), ddH$_2$O to 50 ml. Adjust pH with 10 M NaOH. Store at 4 °C.

- **4x Tris-SDS pH 8.8:** 1.5 M Tris (18.2 g), 0.4% SDS (0.4 g), ddH$_2$O to 100 ml. Adjust pH with 10 M NaOH. Store at 4 °C.

- **10x SDS running buffer:** containing 0.25 M Tris (15.1 g), 2 M glycine (72 g), 1% SDS (5 g), and ddH$_2$O to 500 ml. Storage at RT.

1. Prepare all necessary glass plates needed for the gels and clean them sequentially with ddH$_2$O and 70% ethanol/dH$_2$O.
2. Assemble glass plates in the Mini-PROTEAN® 3 system clamps.
3. First prepare the solution for the resolving gel, according to Table 5 (p. 104) and pour between the plates. Leave approximately 1 cm space below the rim of the small glass plate.
4. Pipette 1-2 ml isopropanol above the resolving gel and allow it to polymerise for approximately 1 h.
5. Discard isopropanol and carefully clean any excess.
6. Prepare and pour the stacking gel solution on top of the resolving gel and immediately place the comb in position. Allow it to polymerase for about 1 h.
7. Prepare samples to load. These should have been already adjusted to a concentration of 5 µg/µl, including 5 x Lämmli sample buffer. Heat samples to 95 °C for 5 min to denature proteins.
8. In the meantime, assemble the electrophoresis apparatus. If only one set of glasses is going to be used, seal the opposite side with the mock plastic plate. Insert the gel holder into the gel running chamber and fill up the inner space with 1x SDS running buffer. After having excluded any leaks, fill up the outer space with 1x SDS running buffer and remove the combs.
9. Load 4 µl of the Page Ruler™ prestained protein ladder (Fermentas, *Thermo Fisher*) and then carry on with the protein samples.
10. Run the gel at 100 V for 5 min until the samples reach the bottom of the stacking gel.
11. Run at 150 V until the blue front reaches the bottom of the resolving gel.

B.5.2 Western blotting

- **Anode buffer I, pH 10.4:** 0.3 M Tris (36.3 g), 20% methanol (200 ml), ddH$_2$O to 1 L. Store at RT.

- **Anode buffer II, pH 10.4:** 0.025 M Tris (3.03 g), 20% methanol (200 ml), ddH$_2$O to 1 L. Store at RT.

- **Cathode buffer, pH 7.6:** 0.025 M Tris (3.03 g), 40 mM 6-amino-hexanoic acid (5.2 g), 20% methanol (200 ml), ddH$_2$O to 1 L. Store at RT.

- **5% milk powder in TBS-T:** 5% milk powder (blotting grade; 25 g), TBS-T to 500 ml. Always prepare fresh according to the quantity needed.
- **1% milk powder in TBS-T:** 1% milk powder (blotting grade; 5 g), TBS-T to 500 ml. Prepare fresh, as needed.
- **Primary antibody solution:** primary antibody diluted in TBS-T, supplemented with 5% BSA and 0.05% sodium azide (NaN_3).
- **Secondary antibody solution:** secondary HRP-conjugated antibody diluted (1:5000) in 1% milk powder.

1. Prepare 16 Whatman papers per blot in the approximate size of the resolving gel.
2. Soak 4 pieces in anode buffer I, 4 pieces in anode buffer II, and 8 pieces in cathode buffer.
3. Cut PVDF membrane (Immobilon™-P Transfer Membrane, *Millipore*) at the size of the resolving gel, activate briefly in methanol and wash it thoroughly in anode solution II.
4. Assemble the blot in a MAXI-Semi-Dry-Blotter (*Roth*) in the following order:
    - Weight (approximately 0.5 kg)
    - (Top: cathode)
    - 8 Whatman papers soaked in cathode solution
    - Gel (excluding the stacking gel)
    - PVDF membrane
    - 4 Whatman papers soaked in anode solution II
    - 4 Whatman papers soaked in anode solution I
    - (Bottom: anode)
5. Remove any bubbles after having placed every layer, by rolling over a plastic pipette.
6. Blot at 55 mA per blot for approximately 1 h.
7. Disassemble the blotting apparatus, cut membrane accordingly if necessary, and label the marker bands with a pencil.
8. Block the membrane with 5% milk powder in TBS-T for 1 h at RT.
9. Wash 3 x 3 min. in 1% milk powder in TBS-T at RT.
10. Wash once again in TBS-T for 5 min.
11. Incubate membrane in a 50 ml falcon tube with the primary antibody solution (see Table 3, p. 102) overnight at 4 °C with constant rotation.
12. On the next day, wash the membrane 3 times for 3 min with 1% milk powder in TBS-T with light agitation.
13. Incubate in the secondary antibody solution for 1 h at RT with light agitation.
14. Wash for 5 min in 1% milk powder in TBS-T.
15. Wash twice for 3 min in TBS-T.
16. Develop the blot with the commercially available ECL reagent (Amersham ECL Western Blotting Detection Reagent, *GE Healthcare*). Mix solution A and B at a ratio of 1:1 (typically, 400 µl of each solution, always prepare right before use). You may need to dilute this mixture with TBS-T, depending on the expected signal intensity.

17. Place the membrane into a clean, clear plastic container and cover with the ECL reagent (800 µl per membrane).
18. Acquire images with an appropriate imager (ChemiDoc™ MP, Imaging System, *Bio-Rad* / FluorChem® FC3, *Biozym Scientific GmbH*).

B.6 Noradrenaline measurement in BAT

To determine the levels of noradrenaline in BAT of control and mutant mice, under basal and stress conditions, we used a commercially available noradrenaline research ELISA™ kit (BA E-5200, ImmuSmol, Pessac, France). This competitive ELISA kit makes use of the microtiter plate format, where the antigen (noradrenaline) is bound on the solid phase. Noradrenaline present in the sample and that bound on the solid phase compete for a “fixed” number of noradrenaline-binding antibody sites. After incubation with the antibody, free sample-antigen, and unbound antigen-antiserum complexes are washed away. Antiserum bound on the solid phase-adhered noradrenaline is detected by an anti-rabbit, peroxidase-linked antibody with TMB (3,3’,5,5’-tetramethylbenzidine) as a chromogenic substrate. The absorption of the reaction product is read at 450 nm and the noradrenaline concentration is inversely proportional to the colour intensity of the chromogen. Unknown noradrenaline levels in a sample can be extrapolated by comparison to a standard curve generated with samples of known concentration, after correcting for the dilution factor. To extract and preserve noradrenaline from BAT, halved, snap-frozen tissue was homogenised in a Fast Prep®-24 instrument, in a lysis solution containing 0.01 N HCl in the presence of EDTA (final concentration 1 mM) and sodium metabisulfite (final concentration 4 mM). Under these conditions, noradrenaline is positively charged, a fact that reduces binding to proteins and optimises solubility, as stated by the supplier. For determination of noradrenaline in BAT, lysates were diluted 1:10 prior to loading on the ELISA microtiter plate. Samples were measured in duplicates according to the manufacturer’s instructions. The detection limit was at 1 ng/ml and the intra-assay coefficient of variation for human EDTA-plasma was 8.4 % in the medium range concentrations.

- **Noradrenaline lysis buffer:** consisting of 0.01 N HCl (pipette 2 µl of 37% HCl in 1998 µl ddH_2O), 80 µl of 100 mM sodium metabisulfite (dilute 1.9 g sodium metabisulfite in 100 ml dH_20) and 15 µl of 5% EDTA/PBS.

- **5% EDTA/PBS:** Dissolve 5 g of EDTA in 100 ml of PBS.

1. Prepare Fast Prep™ tubes (M tubes, MP Biomedicals, CA, USA). Fill in a small amount of lysing sand (Garnet Matrix A Bulk, MP Biomedicals,), one 1/4” ceramic sphere (MP Biomedicals) and 150 µl of noradrenaline lysis buffer. Occasionally, higher amounts of noradrenaline lysis buffer (150-300 µl) are needed, depending on the tissue volume.
2. Quickly thaw snap-frozen tissues on ice and place in Fast Prep™ tubes already containing the lysing sand, the ceramic sphere, and the noradrenaline lysis buffer. Label tubes on the side, because homogenisation will destroy marker labelling on the tube cap.
3. Homogenise tissue in a Fast Prep®-24 instrument (MP Biomedicals) 2 times, for 30 sec at 6.5m/sec. Occasionally, when tissue is not dissolving, additional homogenisation runs might need to be performed.
4. Centrifuge samples at 10,000 rpm for 10 min at 4 °C.
5. Transfer supernatant into fresh Eppendorf tubes. Note down the supernatant volume of each tube, as this will be important for noradrenaline normalisation.
6. Place tubes in ice for immediate, or store at -80 °C for future determination of noradrenaline.
7. Dilute original BAT lysates 1:10 with ddH_2O before commencing noradrenaline determination with the help of the BA E-5200 kit (ImmuSmol, France). Prepare dilutions with 20-50 µl final volume. Use 10 µl of the diluted lysates to load on the microtiter plate. Duplicates are advisable.
8. Determine noradrenaline concern ration according to the manufacturer’s instructions. Process takes two working days.
9. Generate a standard curve with the OD values of the known samples (standard). With the help of the standard curve extrapolate noradrenaline concentration in the unknown samples.
10. Apply correction factor(s) according to the instructions of the manufacturer.
11. Normalise noradrenaline content of BAT accordingly (e.g. x noradrenaline/ mg tissue. Lysate volume and BAT weight in mg is here necessary).

B.7 FRET-based cGMP imaging in cultured cells and tissue slices

FRET-based cGMP imaging was performed with cGi500-expressing cultured cells or acute vibratome tissue slices. To image cGMP dynamics in cultured cells, in real-time, we used an inverted Axiovert 200 microscope bearing 1.0/1.6x Optovar lens (Carl Zeiss, Germany), equipped with fluorescence-grade objectives (Plan-NeoFluar 10x/0.30; EC Plan NeoFluar 40x/1.30 Oil, Carl Zeiss, Germany). The light source (Oligochrome, TILL Photonics, Germany) bore a 445/20 nm CFP excitation filter (AHF, Germany), combined with a 470 nm dichroic mirror (AHF) located in the microscope. Simultaneous recording of CFP and YFP signals from samples was achieved with a cooled electron-multiplying charged-coupled device (EM-CCD) camera (Retiga 2000R, QImaging, Canada), after having been separated by a DUAL-View beam splitter (Micro-Imager, Photometrics, USA) with a 05-EM insert (516 nm dichroic mirror, 480/30 nm, and 535/40 nm emission filters). Cells grown on 12 mm-coverslips were mounted with silicon on a superfusion chamber (RC-26, Warner Instruments, USA) held down on a magnetic platform (Warner Instruments, USA). Steady and continuous cell superfusion at a rate of 1 ml/min (37 °C) with imaging buffer was done by an FPLC pump (Pharmacia P-500, GE Healthcare) through FPLC injection valves (Pharmacia IV-7, GE Healthcare) with 2 ml sample loops. Liquid waste was collected from the opposite side of the inlet tube, with a needle connected to a vacuum pump (Laboport N86, KNF Neuberger, Germany). cGMP-elevating drugs were diluted and supplied at the indicated concentration into the imaging buffer.

For live-cell imaging on vibratome slices, we used a spinning-disk microscope. In short, the setup consisted of an upright Examiner Z1 microscope (Zeiss, Germany), a Yokogawa CSU-X1 spinning-disk, confocal scanner, three diode lasers (445 nm, 488 nm and 561 nm), three water immersion objectives (W NACHROMAT 10x/0.3, W Plan-APOCHROMAT 20x/1.0 DIC (UV) VIS-IR, W Plan-APOCHROMAT 40x/1.0 DIC VIS-IR; all purchased from Zeiss, Germany) and one air objective (EC Plan-NEOFLUAR 2.5x/0.085; Zeiss). For FRET-based cGMP imaging, we excited the donor fluorophore CFP with the 445 nm laser. A Dual-View beam splitter (Micro-Imager, Photometrics, USA) with a 505 nm dichroic mirror, and with 470/24 nm and 535/30 nm emission filters was used for the simultaneous acquisition of CFP and YFP. Signals were recorded with an electron-multiplying charge-coupled device (EM-CCD) camera (QuantEM 512SC, Photometrics) at a frame rate of 5 Hz and an exposure time of 300 msec. The system was controlled by VisiView software (Visitron Systems, Germany). During real-time imaging, the tissue was continuously superfused with carbogen-gassed Ringer buffer or Ringer buffer containing the drugs of interest, at a flow rate of 1 mL/min at 37 °C. A custom-built superfusion system was used consisting of a FPLC pump (Pharmacia P-500, GE Healthcare), FPLC injection valves (Pharmacia V-7, GE Healthcare), a magnetic platform (Warner Instruments, USA), a superfusion chamber (RC-26, Warner Instruments), a Slice Hold-Down (SHD-26H/10, Warner Instruments), and a sample loop (2 mL). Buffer was removed from the chamber via the help of a vacuum pump with an adjustable vacuum (Laboport N86, KNF Neuberger, Germany).

B.7.1 FRET-based cGMP imaging in cultured cells

BAT and adrenal gland-isolated cells from mice expressing the cGi500 biosensor, were cultured for 7 days on 12 mm coverslips under standard conditions, as described in **B.2.4**. Serum starvation was not performed at any point of the experiment. On the day of the FRET measurement, coverslips were removed from the 24-well plate, fixed on the superfusion chamber and subjected to FRET imaging using an epifluorescence microscope.

- **Imaging buffer (pH 7.4):** 140 mM NaCl (8.18 g), 5 mM KCl (0.373 g), 1.2 mM $MgCl_2$ (0.296 g $MgCl_2$), 2.0 mM $CaCl_2$ (0.222 g), 5 mM HEPES (1.19 g). Add dH_2O to 1 L, adjust pH to 7.4 with NaOH, autoclave, store in the dark at RT. Right before use, add 1 ml 1 M D-glucose to 1 L imaging buffer (final concentration ~10 mM D-glucose).

- **100 µM ANP:** Dissolve 0.1 mg ANP (1-28, rat; Sigma-Aldrich) in 327 µl H_2O, store in 50 µl aliquots at -20 °C.

- **100 µM CNP:** Dissolve 0.5 mg CNP (Sigma-Aldrich) in 2.275 ml H_2O, store in 50 µl aliquots at -20 °C.

- **100 mM DEA/NO:** Dissolve 50 mg 2-(N, N-diethylamino)-diazenolate-2-oxide diethyl ammonium salt (DEA/NO, Axxora) in 2.42 ml ice-cold 10 mM NaOH, store in 50 µl aliquots at -20 °C.

1. cGMP measurements are carried out in a dark, air-conditioned room ($T \approx 21$ °C).
2. Before starting the FRET experiment, make sure that the F_{480} and F_{535} channels of the beam splitter are perfectly aligned. If not, align them with the help of the specific slide.
3. Connect sample loops of appropriate volume at the injection valves, (2 ml loops were used throughout the experiments with a superfusion rate of 1 ml/min). Connect the imaging buffer to the FPLC pump and wash the superfusion system including the sample loops with imaging buffer for 10 min at 5 ml/min.
4. Take out of the 24-well plate the coverslip on which the cGi500 expressing cells are growing, place it carefully in a 35 mm culture dish filled with imaging buffer and transfer it to the imaging room.
5. Assemble the superfusion chamber. Place silicon grease on the chamber frame and the chamber plate to seal it. Carefully mount the coverslip with the cells facing the inside of the chamber. Place the chamber plate on top of the coverslip, add 500 µl imaging buffer to cover the cells to prevent them from drying out, and finish the chamber assembly. Clean the bottom of the glass coverslip with a tissue and 70 % ethanol. Place the chamber onto the microscope stage.
6. Connect the inlet and outlet tubing and start the perfusion at a rate of 1 ml/min. Inspect the system for any leaks. Strictly avoid any buffer leakage on the microscope objectives.
7. Use the YFP filter set to select a field of view (FOV) with fluorescent cells of appropriate brightness. Select a niche where a sufficient number of cells are present, with moderate sensor

expression and normal cell morphology (the sensor localization should be homogeneously distributed in the cytosol without localized depositions (‘bright spots’).

8. Acquire a snapshot image of the fluorescent cells in the FOV. Select regions of interests (ROIs) to be imaged as well as a background (bg) region without fluorescent cells.
9. Adjust camera optimal settings: pixel binning, gain, exposure time and acquisition rate, and commence the experiment.
10. Obtain a stable baseline by recording images during superfusion with imaging buffer only.
11. Prepare dilutions of cGMP-elevating drugs in imaging buffer to their final concentrations. Typical final concentrations are: DEA/NO 20-500 nM, ANP and CNP 10-250 nM. Prepare at least 3 ml buffer, to counteract for dead volumes of the superfusion system (tubing, syringes). With the help of a syringe, load the compounds via the injection valves into the respective sample loops.
12. Apply the drug of interest by switching the respective valve. Concurrently, note down the application time (as well as starting frame). To terminate the superfusion of the drug, switch the valve back to the loading position and note down the time (and end frame). Wash the sample loops with imaging buffer before loading the next drug solution.
13. Upon drug application, follow the F_{480}/F_{535} ratio changes, to recognise cGMP transients. Always examine changes in single traces (CFP and YFP channels) to confirm genuine cGMP signals.
14. At the end of the imaging session, flush the entire superfusion system including the injection valves, sample loops and all connective tubing with H_2O, and subsequently with 20% ethanol.

B.7.2 FRET-based cGMP imaging in acute tissue slices

FRET-based cGMP live imaging was conducted in acute BAT slices from mice of both sexes expressing the cGi500 cGMP biosensor under the control of Nes-Cre. This technique exploits the advantages of the cells being in their native environment and avoids possible artefacts arising from extensive cell culture (cell-cell interactions, cell differentiation). Tissue slices at a thickness of 300 µm were generated with a vibratome in ice-cold PBS solution. Sections were placed on the superfusion chamber and held down in place with a mesh and a Slice-Hold-Down harp. Imaging was performed with a 40 x water objective.

- **Ringer buffer:** weight and dissolve in ddH_20 in this order: 126 mM NaCl (7.4 g), 2.5 mM KCl (0.186 g), 1 mM $MgCl_2$ (0.096 g), 1 mM $CaCl_2$ (0.12 g), and 20 mM D-glucose (3.6 g). At last add 1.25 mM NaH_2PO_4 (0.15 g) and 26 mM $NaHCO_3$ (2.2 g). Add ddH_20 to 1 L. Use right after preparation or store at 4 °C for future use.

1. Spinning-disk, FRET-based cGMP measurements were performed in dark, in an air-conditioned room.

2. Before euthanizing the experimental animal, prepare and organise all necessary material and buffers (Ringer buffer, PBS, box with ice, fine scissors, forceps, perfusion chamber, mesh, and slice-hold-down harp).
3. Euthanize the mouse with the appropriate genotype. Then, spray the interscapular region with 70% ethanol, excise BAT and place it in a small culture dish (35 mm) containing ice-cold PBS.
4. Position a new blade into the blade holder of the vibratome. Fill in the outer reservoir with ice and the inner with PBS. Tape the tissue holder, put a drop of instant adhesive and place the halved BAT on it.
5. Cut the tissue at a thickness of 300 µm. While cutting, use a forceps to finely lift up and separate the slice from the tissue chunk. Leave slices in PBS after cutting.
6. Assemble the superfusion chamber, position the slice on the glass coverslip and place the nylon mesh and the harp on top.
7. Situate the superfusion chamber on the microscope stage, connect all the tubing (inlet, outlet) and start the superfusion with carbogen-gassed Ringer’s buffer at a rate of 1 ml/min. Check for any leaks.
8. Use a 40x water objective and the confocal GFP setting to locate the area where the measurement will be performed.
9. Thereafter, switch to the FRET settings and execute the measurement as described in section B.7.1.
10. After the end of the experiment, discard the tissue slices, clean the superfusion chamber with 70% ethanol and run 20% ethanol through the superfusion tubing.

B.7.3 Analysis of FRET data

FRET-based cGMP imaging data were acquired as .tiff videos and analysed as previously described [184] with the help of Fiji (NIH, USA), Microsoft Excel (Microsoft, USA), and OriginPro (OriginLab Corp., USA) software. Intensities of F_{480} signals (CFP emission at 480 nm, cyan traces in respective graphs) and F_{535} signals (YFP emission at 535 nm, orange traces in respective graphs) from fluorescent ROIs were background-corrected using a non-fluorescent ROI and subsequently employed to compute the F_{480}/F_{535} ratio R (black traces in respective graphs). Baseline R_0 was obtained by averaging the F_{480}/F_{535} ratio R recordings from the beginning of each measurement t_0, until the first drug application t_1. Ratio changes ($\Delta F_{480}/F_{480}$, $\Delta F_{535}/F_{535}$, and the corresponding $\Delta R/R$ traces) were then obtained by normalisation to the baseline R_0. Necessary statistical analyses and graphical presentation were performed using Origin software.

1. For the analysis of FRET data, use Fiji, Microsoft Excel and OriginPro software.

2. Check the CFP, YFP videos for significant X, Y movements or focus drifts. Use the StackReg option of Fiji (Plugins →Registration →StackReg) to correct sample movement.
3. Select fluorescent ROIs and a background ROI. Read the ROI intensities in F_{480}, F_{535} channels.
4. Subtract background intensities from F_{480}, F_{535} channels and build the background-corrected F_{480}/ F_{535} ratio R.
5. Calculate the baseline, by averaging the F_{480}/ F_{535} ratio from the initiation of the experiment, until the first drug application.
6. Use this baseline to normalise the F_{480}/ F_{535} ratio and to obtain the relative change ratios $\Delta F_{480}/ F_{480}$, $\Delta F_{535}/ F_{535}$, as well as the ΔR/R.
7. To exclude non-genuine cGMP transients, always inspect the single traces F_{480}, F_{535}. CFP and YFP traces in a real cGMP transient should move to the opposite direction upon addition of the cGMP-elevating drug. Cells showing aberrant traces (low signal-to-noise ratios, non-separation of CFP and YFP signals) should be excluded from later evaluation steps.
8. To graphically present the FRET data, group cells with the same reaction pattern and build the mean ± SEM of the $\Delta F_{480}/ F_{480}$, $\Delta F_{535}/ F_{535}$, as well as the ΔR/R values.
9. When needed; to estimate the peak height and the area under the curve of ΔR/R traces, use the Peak Analyser of OriginPro. The baseline, the tip of the peak, as well as the borders of the area under the curve are determined manually.

B.8 PET imaging and analysis of PET tracer uptake in cold-stressed cGKI-brain KO mice

To investigate the function of BAT under cold-stress, we performed small animal PET scan analysis. Under acute cold exposure, brown adipocytes take up glucose and fatty acids from the bloodstream to generate heat via UCP-1 [199, 200]. The use of small-animal PET imaging to visualise BAT activity has been previously described [201, 202]. PET imaging with $[^{18}F]$FDG was carried out in the Laboratory for Preclinical Imaging and Imaging Technology, Department of Preclinical Imaging and Radiopharmacy, Werner Siemens Imaging Center Tübingen (Tübingen, Germany) with a dedicated small-animal PET scanner (Inveon, Siemens Healthcare, USA). At the time of the scanning, mice were 66 and 72 week-old and weighted 26.7 ± 1.2 g (cGKI-brain KO; mean ± SEM) and 29.6 ± 2 .0 g (controls; mean ± SEM). The body weight of mice of the two groups did not differ significantly. PET tracer $[^{18}F]$FDG (8.8 ± 0.2 MBq in 0.5 ml) was injected into 1.5% isoflurane in pure oxygen-anaesthetised mice via the tail vein. Animals were cooled down for 3 h after tracer injection, in a self-made cooling apparatus consisting of plastic beakers and flexible piping with cold circulating water. Tracer uptake in anaesthetised mice (with ketamine (100 mg per kg body weight) and xylazine (10 mg per kg body weight)) was assessed 3 h after injection. Acquisition lasted for 10 min. For data analysis, an Inveon Research Workplace software (Siemens Preclinical Solutions) was used. To examine [^{18}F]FDG uptake in isolated organs, animals were killed and dissected organs were subjected to biodistribution analysis. For biodistribution analysis, organ radioactivity was measured in a γ-counter (Wallac 1470 WIZARD). The fraction of injected tracer dose per gram tissue (%ID per g) was calculated by normalising decay-corrected counts to ID and sample wet weight. Execution and data analysis of the PET scan experiment was performed by Dr Martin Thunemann, Dr Andrea Gerling, and Dr Marcel Krueger.

B.9 Statistical analysis of data

Data presented in this work are expressed as group means ± SEM. Analysis has been carried out using OriginPro 2017 (OriginLab, USA). Significance between two groups was assayed with an unpaired Student’s t-test. For comparison of more than two groups (conditions or time points), a two-way ANOVA, followed by suitable multiple-testing corrections or a repeated-measures ANOVA was performed. Statistical significance is indicated by the p-value, where $p < 0.05$ denotes statistically significant differences between two groups. *: $p \leq 0.05$, **: $p \leq 0.01$, ***: $p \leq 0.001$.

C. Results

C.1 cGKI is expressed in tissues involved in thermogenesis

To decipher the role of cGKI in stress-related thermogenesis, we utilised mice lacking cGKI in the central and peripheral nervous system (for background information and breeding scheme see **B.2.2**). We subjected them to cold-stress and measured thereafter their body temperature with a digital thermometer and the noradrenaline content in BAT via an immunoassay. To shed light on cGKI expression in thermogenic tissues (BAT, hypothalamus), we used a specific, home-made, polyclonal antibody raised in rabbit (from now on referred to as cGKIc), that recognises both cGKI isoforms, cGKIα and cGKIβ [203].

C.1.1 Expression of cGKI in hypothalamus and BAT assayed by Western blot

As the main site of thermoregulation is located in the deep nuclei of the hypothalamus, we initiated our studies by assaying the expression of cGKI in extracts of this tissue. Situated centrally at the base of the brain, above the optic chiasm, the hypothalamus receives and processes thermal inputs from various body regions and dictates the mode of action to distant executive organs such as the BAT or the dermis. Later on, we analysed lysates from BAT.

Western blot analysis of lysates from hypothalamus and BAT of wild type mice (**Figure 9**) revealed a specific immunosignal at approximately 76 kDa, which corresponded to the molecular weight of cGKI. That signal was absent from hypothalamic and BAT tissue extracts of global cGKI KO mice (*lanes 1, 5*), confirming thus the specificity of the antibody. Albeit unequal amounts of protein were loaded, wild type hypothalamus and BAT exhibited high levels of cGKI (*lanes 2, 6*). cGKI-brain KO mice, on the other hand, showed ablation of cGKI in the isolated hypothalamus (*lane 3*). BAT extracts from the same mouse mutants presented a very low level of cGKI (*lane 7*) as compared to their control mice, suggesting that Nes-Cre does recombine at almost a 100% degree in BAT. In the respective control mice (*lane 4, 8*), which possessed only one functional cGKI allele, the amount of cGKI both in the hypothalamus and in BAT was roughly half of that present in the wild type tissues (*comparison of lanes: 2, 4 and 6, 8*).

These Western blot data indicated that cGKI is abundantly expressed in the hypothalamus and BAT, and efficiently ablated in our cGKI-brain KO mouse model.

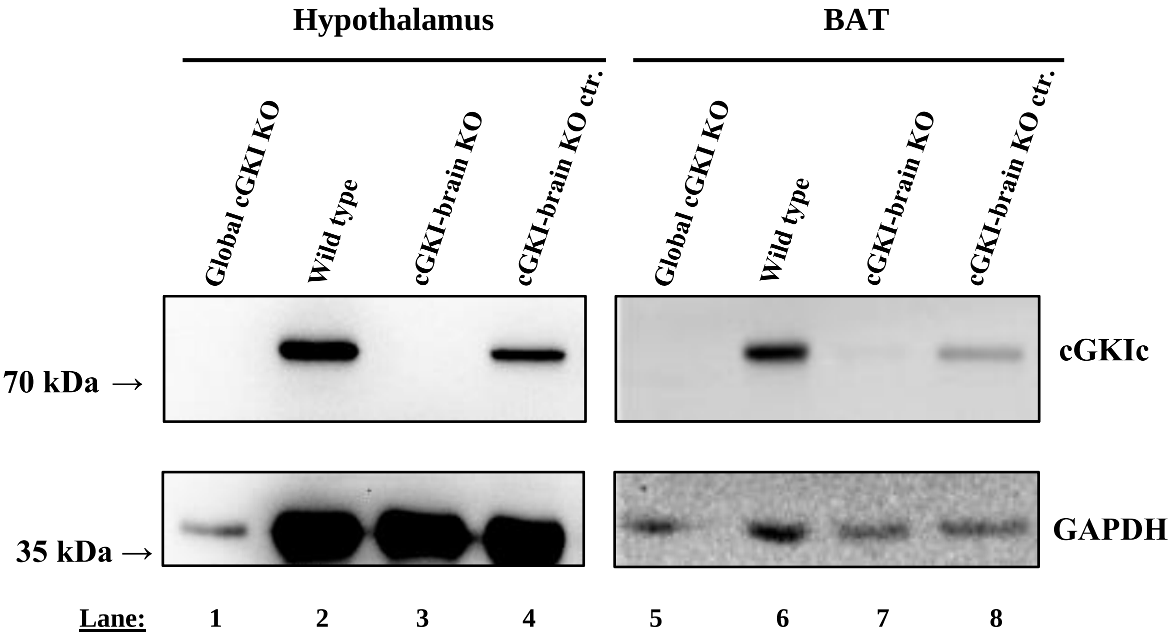

Figure 9. Western blot analysis of cGKI in hypothalamus and BAT extracts of mice of various genotypes.

30 µg of protein from a global cGKI KO (cGKI$^{L1/L1}$, 9-10 week-old male), a cGKI-brain KO (Nes-Cre$^{tg/+}$ x cGKI$^{L1/L2}$, 40 week-old male) and its corresponding control (Nes-Cre$^{tg/+}$ x cGKI$^{+/L2}$, 40 week-old male), as well as from a wild type mouse (cGKI$^{+/+}$, 8 week-old male) was separated on 12% SDS gels and electroblotted onto a PVDF membrane. cGKI (~78 kDa) and GAPDH (~37 kDa) were detected after overnight incubation at 4 °C with the corresponding antibodies.

C.1.2 cGKI localisation in hypothalamus and BAT sections

Because Western blot analysis only provides information about the amount of a specific protein in a tissue, but not its exact localisation, we employed immunostaining methods in wild type hypothalamus and BAT sections to deepen our insights regarding the exact localisation of cGKI in these tissues.

The overall expression of cGKI in the hypothalamus as revealed by our immunohistochemical stainings was rather low, in line with our Western blot results (see **Figure 9**). In detail, stronger positive signals were confined to a small number of neurons located at the compact part of the dorsomedial hypothalamic nucleus (DMC), collaterally of the third ventricle (3V). According to the literature, DMC represents a well-known region for its implication in thermogenesis [129, 130, 132] (**Figure 10 A, B**). As sections approach closer to the rostral side of the hypothalamus, cGKI expression becomes more prominent at the central and dorsal part of the dorsomedial hypothalamic nucleus (DMD) (**Figure 10 C**). Lower expression levels were observed in the arcuate hypothalamic nucleus and in the central and ventrolateral part of the ventromedial hypothalamus (VMHC, VMHDM) (**Figure 10 D**).

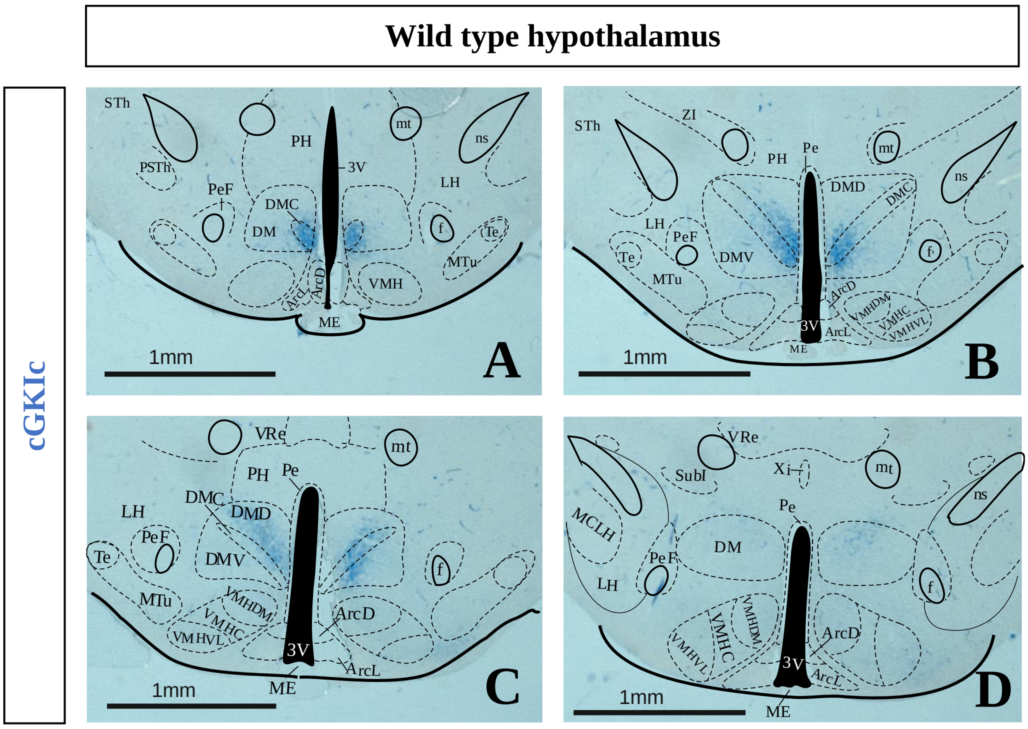

Figure 10. cGKI expression in wild type murine hypothalamus.

Representative immunohistochemistry images of wild type murine hypothalamus (of both genders, 4-12 week-old) depicting cGKI expression in blue. Hypothalamic nuclei are annotated on the image. 10 µm-thick paraffin, coronal sections were stained overnight with the cGKI common antibody and visualised by the avidin-biotin method using the Vector® Blue alkaline phosphatase substrate, as a chromogen. Hypothalamus section of various interaural planes. (A) interaural ca. 1.74 mm. (B) interaural ca. 1.86 mm. (C) interaural ca. 1.98 mm. (D) interaural ca. 2.10 mm. Scale bars: 1 mm. [3V: third ventricle, STh: subthalamic nucleus, PSTh: parasubthalamic nucleus, PeF: perifornical nucleus, PH: posterior hypothalamic area, DM: dorsomedial hypothalamic nucleus, DMC: dorsomedial hypothalamic nucleus; compact part, ArcD: arcuate hypothalamic nucleus; dorsal part, ArcL: arcuate hypothalamic nucleus; lateral part, ME: median eminence, VMH: ventromedial hypothalamic nucleus, Mtu: medial tuberal nucleus, Te: terete hypothalamic nucleus, f: columns of the fornix, LH: lateral hypothalamus, mt: mammillothalamic tract, ns: nigrostriatal bundle, Pe: periventricular hypothalamic nucleus, ZI: zona incerta, VMHDM: ventromedial hypothalamic nucleus; dorsomedial part, VMHC: ventromedial hypothalamic nucleus; central part, VMHVL: ventromedial hypothalamic nucleus; ventrolateral part VRe: ventral reuniens thalamic nucleus]. *(Images prepared and provided by Dr Susanne Feil* [57]*).*

Isolated interscapular brown adipose tissue (iBAT) from wild type mice of either gender was also examined for the exact localisation of cGKI by means of immunofluorescence. **Figure 11 A** shows strong cGKI expression in the VSMC layer of the small blood vessels. These possessed the typical ring-shaped form, seen in cGKI stainings of larger vessels. Moreover, high amounts of cGKI were detected in small, conical cells with little cytoplasm and fine, long processes. Interestingly, these cGKI-positive cells (**Figure 11 A**, white arrows) were equally scattered among brown adipocytes, in which we did not detect cGKI expression. The same results were also obtained with another method. By means of immunohistochemistry on BAT paraffin sections, we observed cGKI-expression in the exact same structures, as with the immunofluorescence (**Figure S1**). Next, we analysed cGKI expression on BAT cryosections from cGKI-brain KO mice. Our immunostainings revealed that cGKI-brain KO mice lacked the bulk of cGKI in BAT. Only a small number of the conical, cGKI-positive cells retained cGKI after the action of Nes-Cre (**Figure 11 B**, white arrow). cGKI in the VSMCs of blood vessels was also recombined. The lower left part of **Figure 11 B** depicts one such vessel, where VSCMs that have retained cGKI after the action of Nes-Cre, are indicated by the white arrow. Peripheral nerve bundles innervating BAT were also intensely positive for cGKI, as depicted in **Figure 11 C**. Here, βIII-tubulin was used in double-stainings with cGKI to visualise nerve bundles (**Figure 11 E, F**). **Figure 11 G** shows at least partial colocalisation of cGKI and βIII-tubulin in the nerve bundles of BAT. We believe that this lack of complete colocalisation might be due to inappropriate cutting angle, that did not favour the simultaneous exposure of cGKI- and βIII-tubulin-positive structures of the nerve bundle. Last but not least, cGKI-brain KO nerve bundles found in BAT completely lacked cGKI, as shown in **Figure 11 D, H**.

In sum, we have found that cGKI is expressed in parts of the hypothalamus, significant for thermogenesis, such as in the dorsomedial hypothalamic nuclei. In BAT, cGKI is highly expressed in the nerve bundles, in VSCMs and also in small, conical cells with long, fine processes. Our data, however, do not provide any evidence for cGKI expression in brown adipocytes themselves.

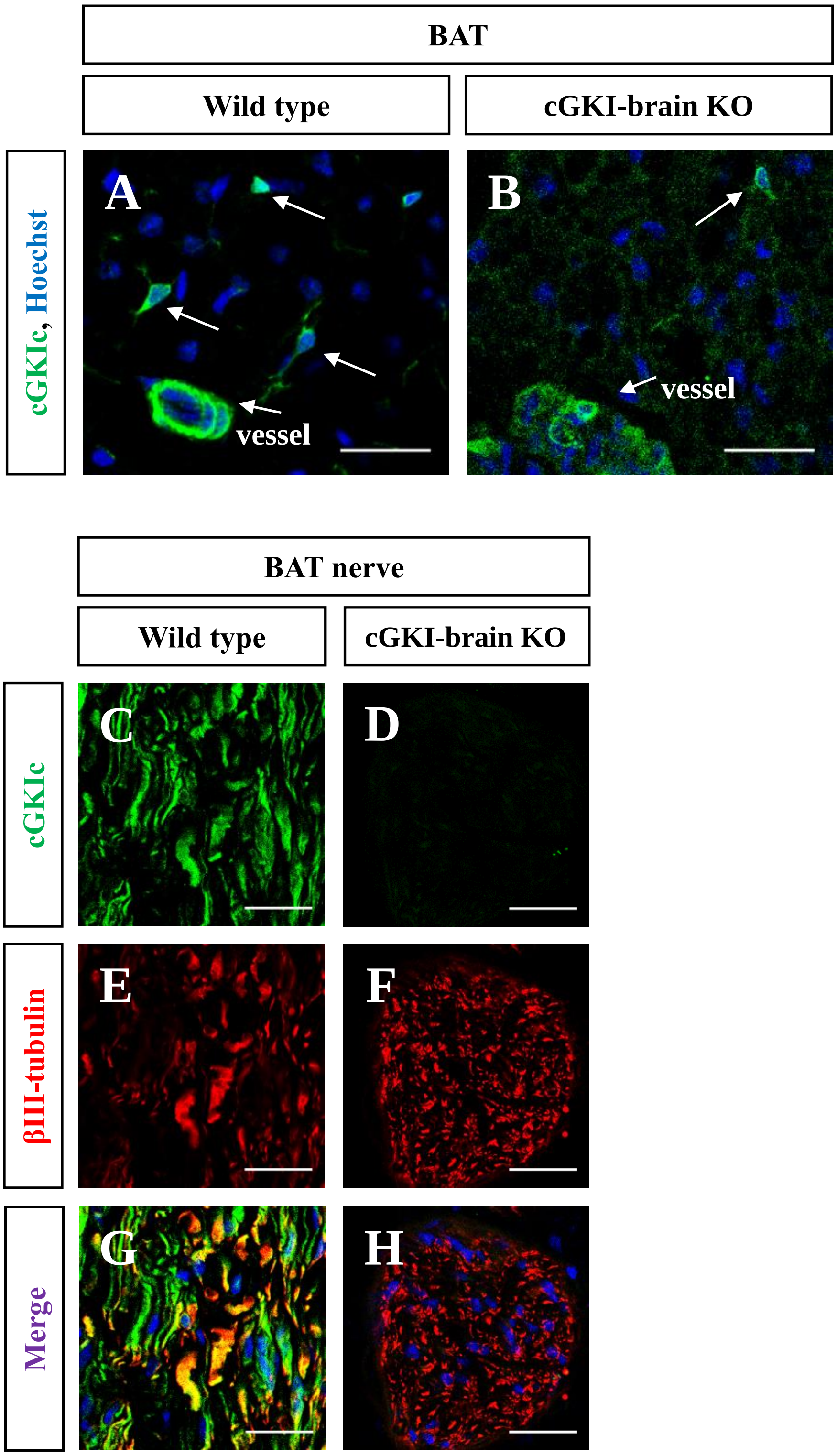

Figure 11. cGKI localisation in wild type murine BAT and in the nerve bundle within it.

Representative immunofluorescence images of 10 µm-thick BAT cryosections from a 6 week-old, male, wild type (A, C, E, G), and a 6 week-old, male, cGKI-brain-KO mouse (B, D, F, H). Sections were immunostained with an anti-cGKI primary and AlexaFluor® 488 secondary antibody. The neuronal marker βIII-tubulin (combined with a red secondary AlexaFluor® 555 antibody) has been used to visualise nerve bundles in BAT. Hoechst 33258 was used to make nuclei visible (blue stain, G, H). Scale bars: 25 µm.

C.2 Recombination activity of Nes-Cre in BAT and adrenal gland

Numerous reporter mice exist to study the recombination pattern of any Cre-transgenic mouse line. In this project, we employed a reporter mouse model, which makes use of fluorescent labelling of cells to analyse the recombination activity of Nes-Cre. This mouse model termed R26-Ai14 expresses the red fluorescent tdTomato protein after Cre-mediated excision of an upstream stop cassette [172].

We used 10 µm-thick cryosections from a Nes-Cre$^{tg/+}$ x R26-Ai14$^{+/L2}$ mouse (Nes-Cre-recombined structures appear in red) and subsequently stained them with our cGKI common antibody (in green). Our expression analysis in BAT cryosections, revealed an overlap of Nes-Cre and cGKI in three structures: i) the sympathetic nerve-bundles innervating BAT, ii) the VSMCs of the small blood vessels irrigating this tissue, and iii) the characteristic, conical cells with the fine, long processes scattered among brown adipocytes. However, Nes-Cre did not recombine all of the characteristic, conical, cGKI-positive cells in BAT (**Figure 12** merge, white arrows).

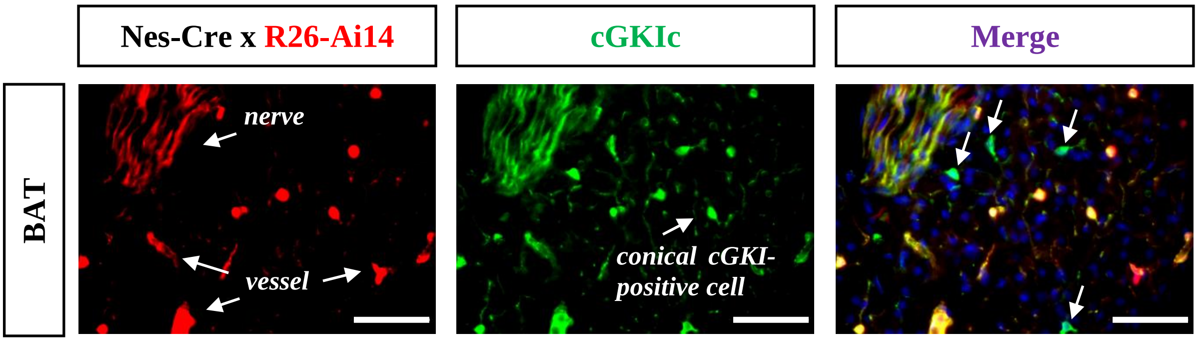

Figure 12. Colocalisation studies of Nes-Cre and cGKI in BAT.

Representative epifluorescence microscope image series of 10 µm-thick cryosections of BAT. Nes-Cre expression is denoted by the intrinsic red fluorescence of tdTomato of the Ai14 reporter mouse (Nes-Cre$^{tg/+}$ x R26-Ai14$^{+/L2}$, 9 week-old female). Sections were sequentially stained with the cGKIc antibody and visualised in green with an AlexaFluor® 488 secondary antibody. Nuclei were stained with the Hoechst 33258 dye (blue stain in merge). Scale bars: 50 µm.

Next, we analysed the expression of cGKI in the wild type adrenal gland. 10 µm-thick cryosections of an adrenal gland revealed strong expression of cGKI in the adrenal gland capsule, in VSMCs of small blood vessels, as well as in small, conical cells of the adrenal gland cortex, scattered among the CORT-producing cells (**Figure 13 A**, dashed-line box). Subsequent examination of adrenal glands from a cGKI-brain KO mouse demonstrated expression of cGKI in the exact same structures as in the wild type tissue (**Figure 13 B**).

A Western blot of adrenal gland-tissue extracts from control and cGKI-brain KO animals revealed a rather low recombination rate in that tissue. That low recombination rate of Nes-Cre in the adrenal gland was denoted by the relatively strong cGKI band in the cGKI-brain KO mice in comparison to control animals (**Figure 13 C**).

In-depth immunofluorescent analysis of the adrenal gland demonstrated strong activity of Nes-Cre (shown in red) in the adrenal gland medulla (probably in chromaffin cells), the main site of catecholamine production (**Figure 13 F**, left panel). However, cGKI seemed not to be present in those cells, or generally in the medulla (**Figure 13 F**, middle panel). On the other hand, our analyses showed strong expression of cGKI in the fibrous cap surrounding the adrenal gland, and also in characteristic, small, conical cells of the cortex, scattered among CORT-producing cells, but not in the latter (**Figure 13 E**, middle panel). Interestingly, we observed no red fluorescence in the adrenal cortex or the adrenal capsule. The absence of red fluorescence in those sites indicated the lack of Nes-Cre activity in those structures (**Figure 13 E**, left panel).

In summary, we have investigated in this section the expression and activity pattern of cGKI and Nes-Cre, respectively, in BAT and the adrenal gland. Our data from BAT demonstrated that cGKI and Nes-Cre colocalised, at least, partially. In sections of the adrenal gland, however, that colocalisation of cGKI and Nes-Cre was not evident.

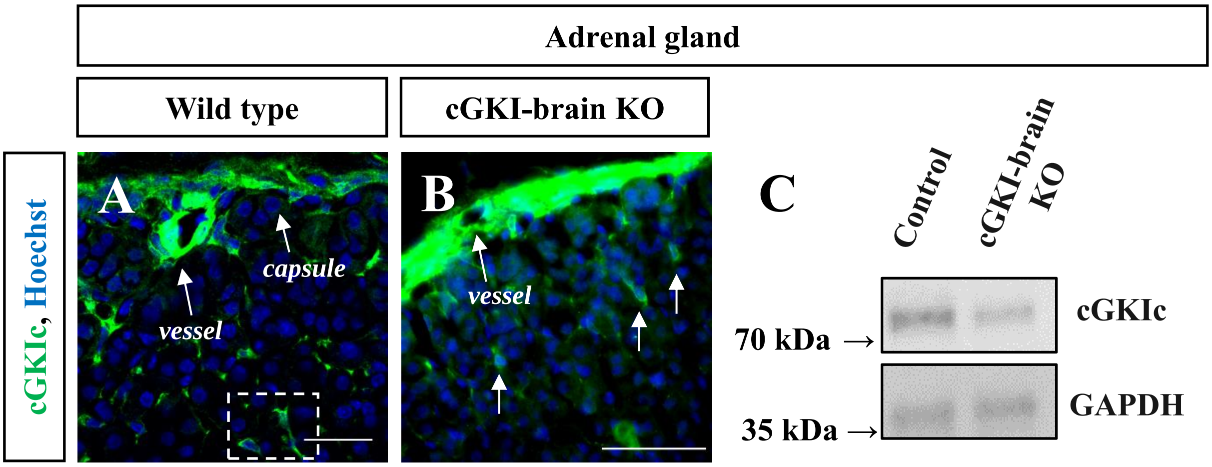

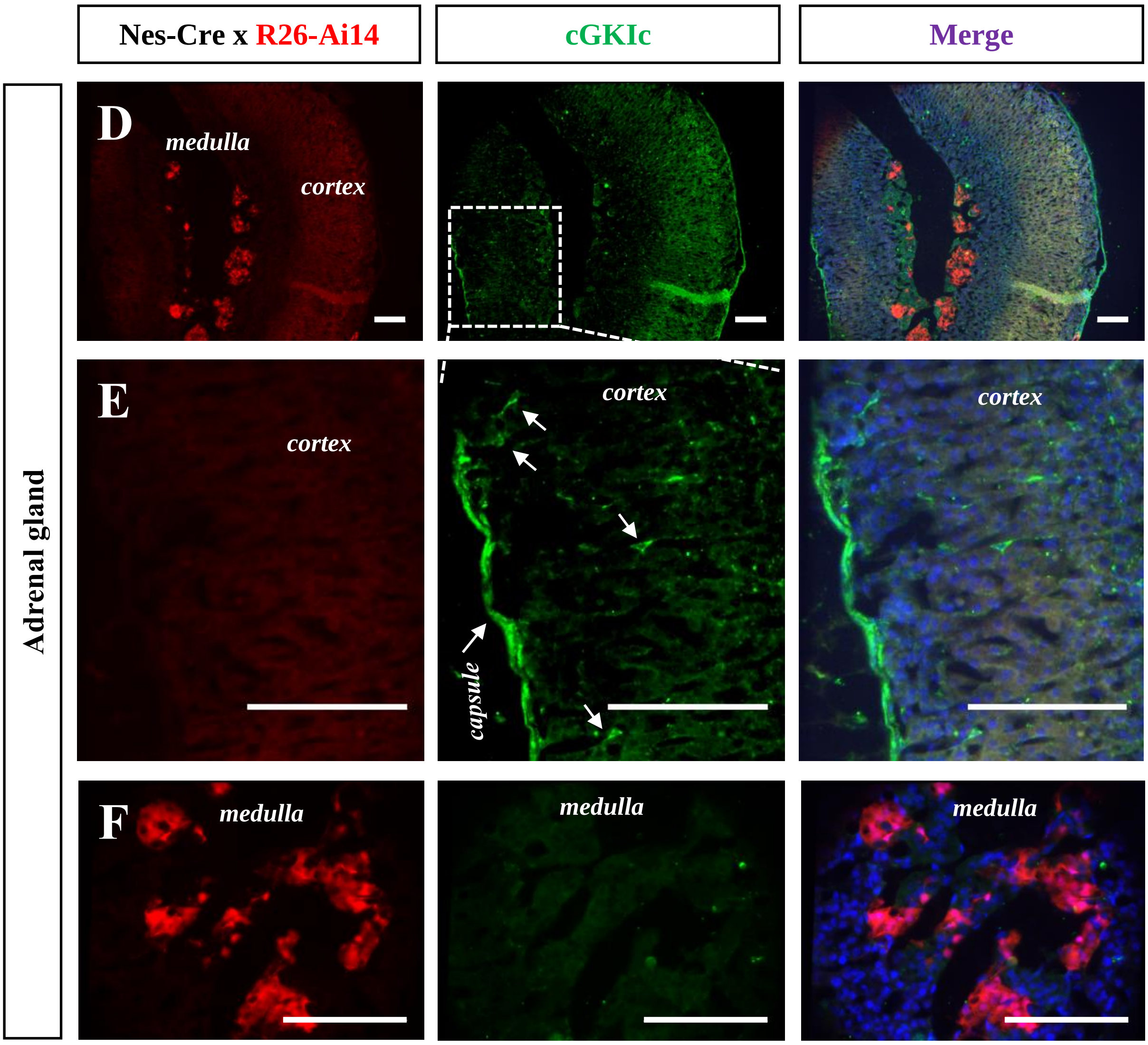

Figure 13. Expression of cGKI in the adrenal gland and colocalisation studies with Nes-Cre.

(A), (B) Representative immunofluorescence images of adrenal gland sections from a 5 week-old, male, wild type and a 9 week-old, male, cGKI-brain KO mouse. 10-µm thick cryosections were stained overnight with an anti-cGKI common primary antibody that recognises both cGKIα and cGKIβ isoforms and visualised with an AlexaFluor® 488 secondary antibody. The Hoechst 33258 dye was used to visualise nuclei (in blue). (C) Western blot analysis of cGKI in adrenal gland-tissue extracts from cGKI-brain KO and control (Nes-Cre$^{tg/+}$ x cGKI$^{+/L2}$) animals (both males, 40 week-old). 30 µg of protein was separated on 10% SDS gels and electroblotted onto a PVDF membrane. cGKI (~78 kDa) and GAPDH (~37 kDa) were detected after overnight incubation at 4 °C with the corresponding antibodies. (D), (E), (F) Immunofluorescence images from 10 µm-thick adrenal gland cryosections of a 9 week-old, female Nes-Cre$^{tg/+}$ x R26-Ai14$^{+/L2}$ mouse. Nes-Cre expression is denoted by the intrinsic red fluorescence of tdTomato of the Ai14 reporter mouse. The sections were sequentially probed with the cGKIc antibody and visualised in green with a fluorescent-coupled secondary antibody (AlexaFluor® 488). Blue fluorescence of nuclei was achieved via incubation with the Hoechst 33258 dye. (D) Low magnification image series of the adrenal gland (adrenal medulla and cortex). (E) Higher magnification of the adrenal cortex region shown in the dashed white square, responsible for corticosterone production. (F) Higher magnification of the adrenal medulla, where catecholamines are produced. Scale bars: (A) 25 µm, (B) 50 µm, (D-F) 100 µm.

C.3 In vivo examination of cGKI-brain KO mice

To investigate the role of cGKI in the physiology of cold-stress-induced thermogenesis, we subjected cGKI-brain KO mice to a cold-stress ordeal of variable length and monitored their body temperature. At the end of the experiments, BAT was harvested to analyse its noradrenaline levels via the help of an ELISA test. Additional physiological parameters such us their body and BAT weight were taken into account into our analyses.

C.3.1 Body temperature of male mice under a 6-h-cold-stress challenge

To evaluate the role of cGKI in thermogenesis, we subjected male, cGKI-brain KO mice and their litter-matched controls to a 6-hour cold-stress ordeal at 4 °C. We measured their body temperature every hour, anally, with the help of a digital thermometer. Mice exhibited almost identical body temperatures at the start of the experiment with cGKI-brain KO and control mice demonstrating temperatures of 35.2 and 35.3 °C, respectively. Within only 0.5 h from the beginning of the experiment, the body temperature of both groups rapidly dropped to ~31 °C. However, control mice were able to stabilise their body temperature at ~32 °C until the 3rd hour. cGKI-brain KO mice exhibited significantly lower body temperatures at the time point of 3 hours of cold-stress, compared to control animals. Afterwards, the body temperature of both groups dropped. cGKI-brain KO mice displayed a profound decrease in their body temperature in the following hours, compared to the body temperature of control mice. (**Figure 14 A**). At the end of the cold-stress experiment, a pair of mice (a cGKI-brain KO mouse and its litter-matched control) were let to recover over the weekend in a clean cage with fresh bedding, water and rodent chow *ad libitum*. The last time point (rec) presented on the graphic of **Figure 14 A**, displays the ability of the cGKI-brain KO mouse to regain and retain a body temperature similar to that of a control mouse.

At later stages (4th hour afterwards), the body temperature of mutant mice did not reach a significant difference at the 5% level. We believe that this could be probably attributed to the low number of experimental and control animals (n=3 for each group). However, the body weight of the control mice was significantly higher compared to that of cGKI-brain KO mice. Our studies of their BAT weight and the ratio of BAT/body weight revealed no significant differences between the two groups (**Figure 14 B**).

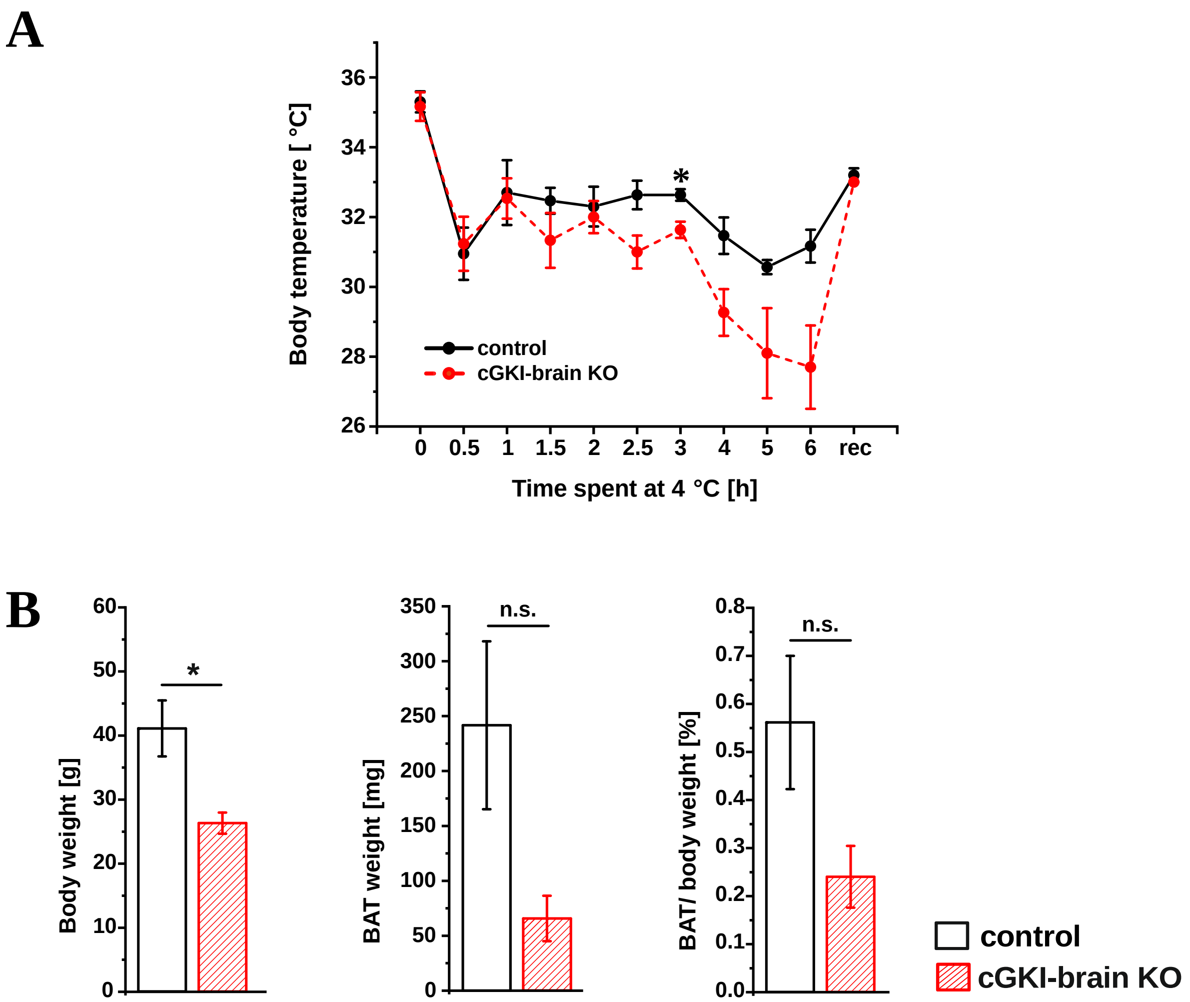

Figure 14. Body temperature of <u>male</u> cGKI-brain KO and control mice under cold-stress.

(A) Body temperature of 3, 40-44 week-old cGKI-brain KO **(red line)** and 3, 40-44 week-old control mice (Nes-Cre$^{tg/+}$ x cGKI$^{+/L2}$, **black line**) was measured rectally with a digital thermometer in half-hour and then hourly intervals. Rec denotes the recovery point of approx. 36 h after the experiment. (B) Body and iBAT weight, as well as the ratio of iBAT/body weight of the mice participated in the cold-stress experiment. Data are presented as mean values of 3 mice with S.E.M. For comparison of two groups, a Student's t-test was applied. Body temperature differences between cGKI-brain KO and control mice were assayed with the use of a Student's t-test. n.s. not significant, *, $p<0.05$.

C.3.2 Body weight analysis: A longitudinal study

In the previous cold-stress experiment (see **C.3.1**), litter-matched, male mice demonstrated an unexpected body weight difference, which had not been formerly taken into consideration. To test if cold-stress experiments might be affected by potential body weight differences between genotypes, we conducted a longitudinal study of the body weight of both sexes and all possible genotypes. For that reason, the body weight of mice was monitored for 13 weeks after they had been genotyped at week 4.

We found no significant body weight differences between the genotypes Nes-Cre$^{+/+}$ x cGKI$^{+/L2}$ and Nes-Cre$^{+/+}$ x cGKI$^{L1/L2}$ or Nes-Cre$^{tg/+}$ x cGKI$^{+/L2}$ at any week in both genders. However, cGKI-brain KO mice of both sexes were significantly lighter than Nes-Cre$^{+/+}$ x cGKI$^{+/L2}$ mice almost from the beginning of the study (week 6-13) and also compared to Nes-Cre$^{+/+}$ x cGKI$^{L1/L2}$ mice (week 5-13). Interestingly, cGKI-brain KO mice of either gender demonstrated no significant body weight difference in comparison to their control mice (genotype: Nes-Cre$^{tg/+}$ x cGKI$^{+/L2}$) at any time during the study (**Figure 15**).

These data indicated that the presence/expression of the Cre transgene in Nes-Cre mice, but not the knockout of cGKI, led to a reduction of body weight.

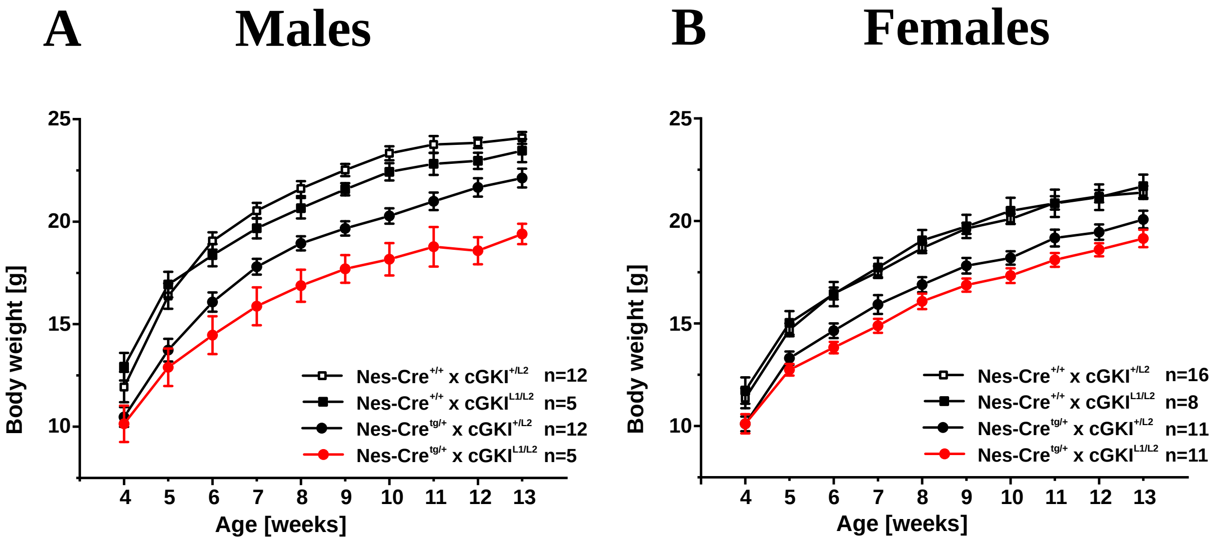

	Nes-Cre$^{+/+}$ cGKI$^{L1/L2}$	**Nes-Cre$^{tg/+}$ cGKI$^{+/L2}$**	**Nes-Cre$^{tg/+}$ cGKI$^{L1/L2}$**
Nes-Cre$^{+/+}$ cGKI$^{+/L2}$	**n.s.**	**n.s.**	*** (week 6-13)**
Nes-Cre$^{+/+}$ cGKI$^{L1/L2}$		*** (week 5)**	*** (week 5-13)**
Nes-Cre$^{tg/+}$ cGKI$^{+/L2}$			**n.s.**

Nes-Cre$^{+/+}$ cGKI$^{L1/L2}$	**Nes-Cre$^{tg/+}$ cGKI$^{+/L2}$**	**Nes-Cre$^{tg/+}$ cGKI$^{L1/L2}$**
n.s.	**n.s.**	*** (week 6-13)**
	n.s.	*** (week 5-13)**
		n.s.

Figure 15. Analysis of the body weight of Nes-Cre x cGKI mice over time.

The body weight of 80 mice of either gender and all genotypes was monitored over a period of 13 weeks. Measurements started at week 4 after the young litter had been genotyped. Panel (A) shows the body weight of 34 male mice of all genotypes and panel (B) that of 46 females for the first 13 weeks after birth. The tables at the bottom row depict the statistical comparisons between genotypes. Data are presented as mean ± SEM. To assess for statistical significance, a 2-way ANOVA test with repeated measures was performed and corrected with Bonferroni's corrections for multiple testing. n.s. not significant, *, $p<0.05$.

C.3.3 Body temperature of female mice under a 6-h-cold-stress challenge

After having monitored and analysed the body weight of mice with and without the Nes-Cre transgene, further cold-stress experiments were solely conducted with female mice, as they showed less body weight variances.

Female mice were subjected to a 6-hour cold-stress test and their body temperature was monitored anally every hour. Both cGKI-brain KO and control mice commenced the experiment with their body temperature lying roughly at 35 °C. Within the first hour, the body temperature of both genotypes plunged to around 28 °C. Paradoxically, at this time point, control mice exhibited significantly lower body temperatures than cGKI-brain KO mice. From the 1st until the 4th hour, cGKI-brain KO and control mice exhibited quite similar body temperatures. Starting at the 5th hour, and until the end of the experiment at the 6th hour, the body temperature of cGKI-brain KO mice remained well below that of the control mice. At these time points, cGKI-brain KO animals exhibited significantly lower body temperatures compared to their control counterparts (**Figure 16 A**). That difference could not have been attributed to differences in their body or BAT weight. The body weight (controls: 24.27 ± 0.43 g versus cGKI-brain KO: 22.58 ± 0.61 g), BAT weight (controls: 29 ± 4.04 mg versus cGKI-brain KO: 27.17 ± 0.87 mg), as well as the ratio of BAT/body weight of the control mice (0.12 ± 0.016 %) compared to cGKI-brain KO mice (0.12 ± 0.005 %) was not different (**Figure 16 B**).

To sum up, we monitored the body temperature of cGKI-brain KO and control mice under cold-stress. Our data, so far, indicate that cGKI-brain KO mice of either gender were unable to maintain their body temperature when subjected to a cold-stress challenge for several hours.

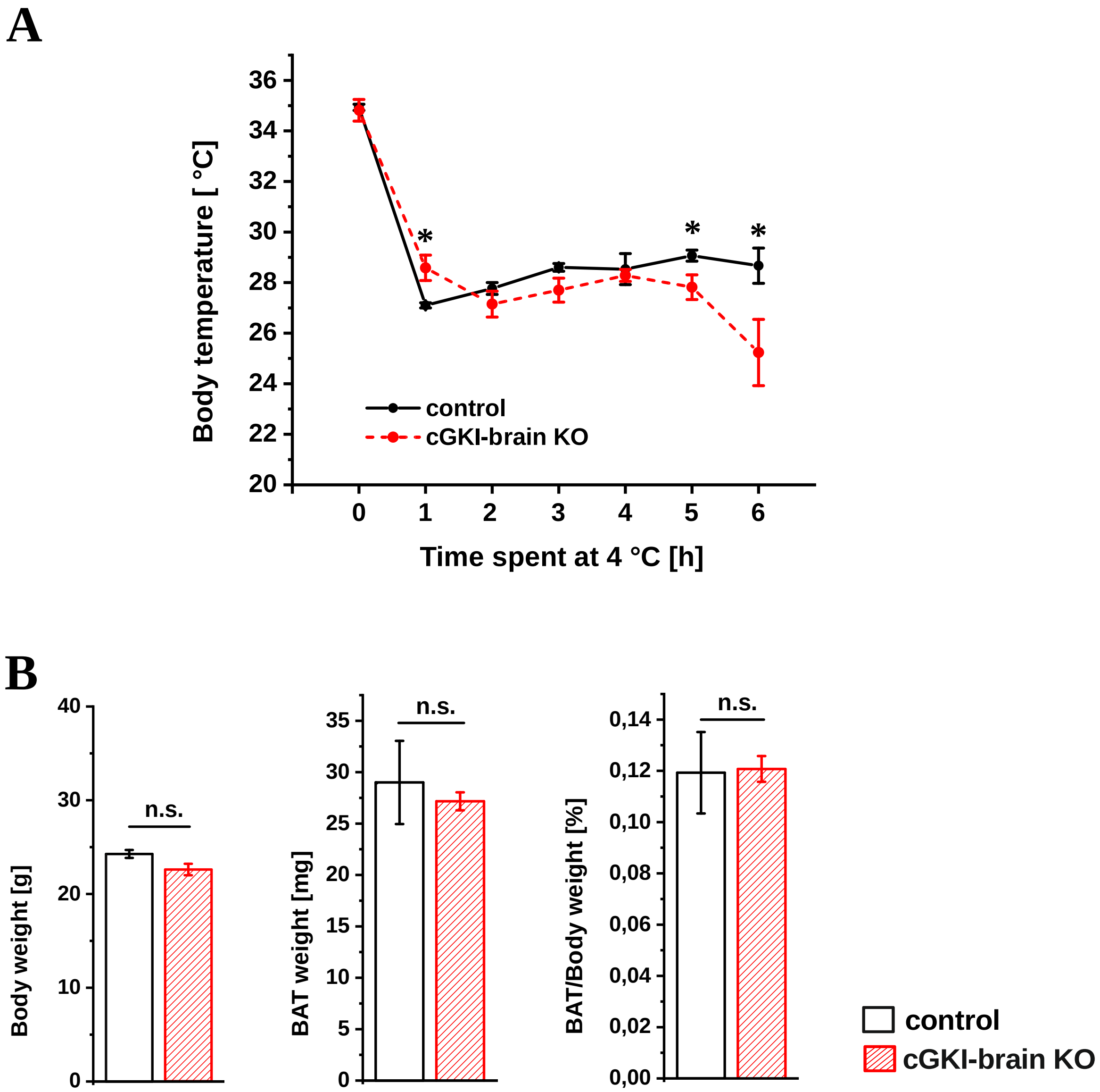

Figure 16. Cold-stress experiment in 27-30 week-old, female cGKI-brain KO and control mice at 4 °C.

(A) Mean body temperature of 6 cGKI-brain KO and 3 control mice during a 6-hour cold-stress ordeal. Data are presented as mean body temperature ± SEM. Statistical significance was assayed with the use of a Student's t-test. (B) Body parameters of the mice participated in the cold-stress experiment. Bar graphs represent mean ± SEM values. Statistical significance between two groups was tested with a Student's t-test. n.s. not significant, *, $p<0.05$.

C.3.4 PET scan analysis of cold-stressed mice

To further elucidate the cellular mechanism underlying the "freezing" phenotype of cGKI-brain KO mice, we studied the uptake of radiolabelled glucose ([^{18}F]FDG) in cold-stressed animals via small-animal PET scan (see **A.7.1** and **B.8**). In line with the rapid drop of their body temperature under the cold-stress test, cGKI-brain KO mice exhibited significantly reduced [^{18}F]FDG uptake in BAT (3.22 ± 0.03 ID/mg tissue), compared to controls (2.76 ± 0.06 ID/mg tissue) (**Figure 17 A**, **B**). **Figure 17 A** presents the difference in tracer uptake in a colour intensity map (iBAT is outlined in white-dashed line). The ratio of BAT to body weight was not different (0.19% and 0.18%, respectively) between the two groups (**Figure 17 C**). Tissue biodistribution analysis revealed similar [^{18}F]FDG uptake in other metabolically-active tissues such as the brain and the heart, in mutant and control mice (2.08 ± 0.22 vs 1.95 ± 0.21 ID/mg tissue and 8.93 ± 1.23 vs 9.95 ± 1.31 ID/mg tissue, respectively) (**Figure 17 D**).

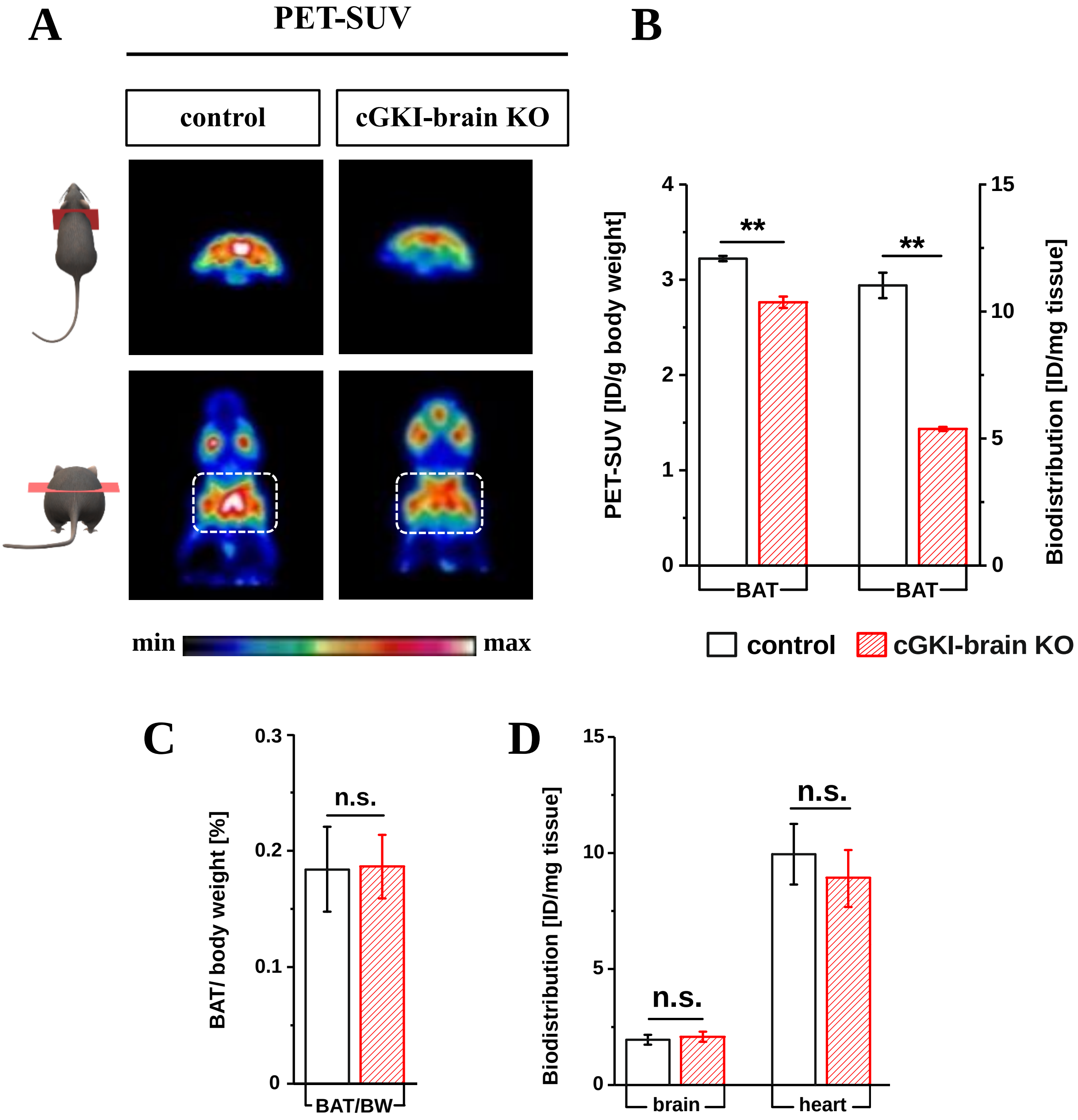

Figure 17. Examination of [^{18}F]FDG uptake in tissues of cold-stressed mice via PET.

3 cGKI-brain KO and 3 control mice (66-72 week-old) of both genders were injected with 7.82-9.39 MBq of radiolabelled glucose [^{18}F]FDG and subjected to cold-stress for 3 h. The uptake of radiolabelled FDG was determined via a small-animal PET scanner. (A) Standardised uptake values (SUV) of BAT of control and mutant mice. The BAT is shown in a transversal plane in the upper row, and in a coronal plane outlined in a white-dashed box in the lower row. (B) Evaluation of the PET scan images (SUV) and biodistribution of BAT. (C) Ratio of BAT/body weight between control and mutant animals. (D) Biodistribution analysis of trace uptake of other metabolically-active organs such as the brain and the heart. Data represent mean values ± SD. Statistical significance between two groups was tested with a Student's t-test. n.s. not significant, ** $p \leq 0.01$ *(Data acquired, analysed, and provided by Dr Martin Thunemann, Dr Andrea Gerling, and Dr Marcel Krüger.).*

C.4 In-depth scrutiny of BAT

Based on our previously-presented cold-stress studies, cGKI-brain KO mice manifested a deficit in maintaining a steady body temperature under cold-stress as compared to control mice. Furthermore, glucose uptake analysis of cold-stressed mice using a small-animal PET scanner pinpointed a possible impairment of the main thermogenic organ, i.e. the BAT. Therefore, we decided to have a closer look at this particular organ and assess its noradrenaline levels and thermogenesis-associated proteins.

C.4.1 Noradrenaline levels in BAT under basal and cold-stress conditions

Thermogenesis in mammals relies on noradrenaline release into BAT, from the sympathetic neurons. To determine whether the impairment in body temperature regulation observed in the cGKI-brain KO mice results from noradrenaline deficits in their BAT, we assayed this hormone in unstressed and cold-stressed animals.

Unstressed, 9-10 week-old, female cGKI-brain KO mice demonstrated significantly lower amounts of noradrenaline in their BAT (0.05 ng/ mg tissue) compared to their control counterparts (0.093 ng/ mg tissue, **Figure 18 A**). This difference in noradrenaline content in BAT is unlikely to have occurred due to differences in their body weight. That is because we had matched experimental and controls animals according to their body weight. Hence, there was no difference in the body weight of both groups (**Figure 18 B**). Similarly, the halved-BAT weight, as well as the ratio of half BAT to body weight of cGKI-brain KO animals was not different from that of controls (**Figure 18 C**, **D**).

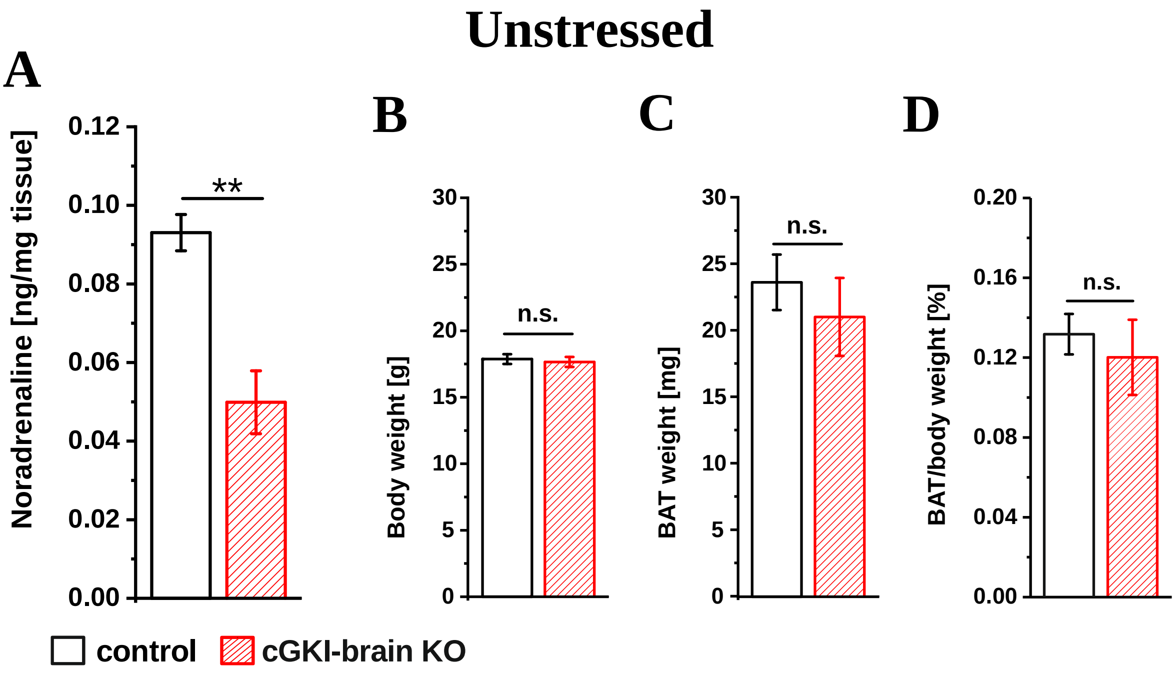

Figure 18. Noradrenaline levels in BAT of female cGKI-brain KO and control mice under basal conditions.

(A) Normalised noradrenaline levels in BAT of 5, 9-10 week-old control (Nes-Cre$^{tg/+}$ x cGKI$^{+/L2}$) and 5 cGKI-brain KO mice. (B) Body weight of experimental and control animals. (C) Weight of half BAT. (D) Ratio of the half-BAT weight to body weight. Data presented as mean values ± SEM. Statistical significance was assayed via a Student's t-test. n.s. not significant, ** $p \leq 0.01$

To assess the noradrenaline content of BAT after a cold-stress challenge, 27-30 week-old, female mice underwent a 6-h-cold-stress test. Their body temperature was monitored anally and has been presented in **C.3.3**. At the end of the experiment, the BAT was excised and processed to determine noradrenaline levels within it (for protocol, see **B.6**).

Our investigation revealed that 6 hours of cold-stress significantly elevated noradrenaline levels in BAT of control mice (0.43 ng/ mg tissue, **Figure 19 A**), as compared to unstressed mice (0.093 ng/ mg tissue, **Figure 18 A**). By examining the 6-h cold-stress experiment separately, we came to the conclusion that cGKI-brain KO mice tended to possess slightly lower quantities of noradrenaline in their BAT (0.34 ng/ mg tissue) in comparison to control mice (0.43 ng/ mg tissue) (**Figure 19 A**). However, this difference did not reach significance at the 5 % level, probably due to the low number of experimental animals (3 control and 6 knockout mice), and the high variance of noradrenaline levels in knockout mice. Importantly, the body weight, the whole-BAT weight, and the ratio of whole-BAT to body weight were not significantly different between the two groups (**Figure 19 B**, **C**, and **D**).

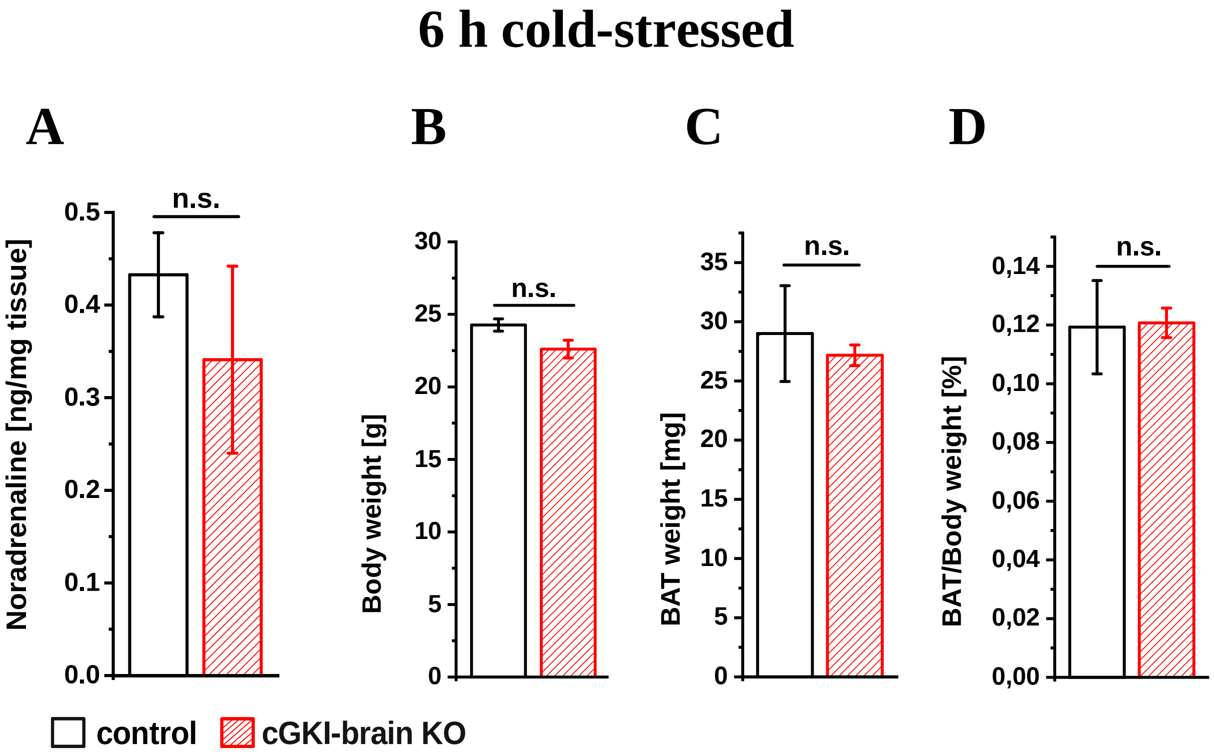

Figure 19. Noradrenaline levels in BAT of female cGKI-brain KO and control mice after 6 h of cold-stress.

(A) 6 27-30 week-old cGKI-brain KO and 3 control, female mice were subjected to a 6-hour cold-stress challenge. Noradrenaline in their BAT was assayed with a competitive ELISA kit and normalised to the weight of BAT tissue (mg). (B) Body weight of experimental and control animals. (C) Weight of whole-BAT. (D) Ratio of BAT weight to body weight. Data are presented as mean values ± SEM. Statistical significance was assayed with a Student’s t-test. n.s. not significant.

C.4.2 Western blot analysis of thermogenesis-related proteins in BAT

To shed light on the potential cellular mechanism underlying the cold-stress vulnerability of cGKI-brain KO mice, we studied the levels of proteins of the thermogenic machinery (UCP-1, TH), via a Western blot analysis.

Since noradrenaline in BAT was significantly different between control and KO animals under basal conditions (see **C.4.1**), we investigated the levels of UCP-1 and TH in this tissue, as these could account for the body temperature differences between the two animal groups. 9-10 week-old, unstressed cGKI-brain KO female mice presented no significantly different UCP-1 (1.31 ± 0.12 a.u.) and TH (0.60 ± 0.11a.u.) levels in comparison to controls (1.94 ± 0.56 a.u., and 1.15 ± 0.34 a.u., respectively). Their BAT weight was also not significantly different between the two groups. Similarly, 6 hours of cold-stress did not alter the amounts of UCP-1 or TH in the BAT of mutant animals compared to controls (UCP-1: 0.76 ± 0.07 a.u. vs 0.99 ± 0.15 a.u., and TH: 0.48 ± 0.03 a.u. vs 0.66 ± 0.11 a.u.). Likewise, the weight of the whole-BAT was not altered in the two groups (**Figure 20 B**).

These data indicated a malfunction of BAT in cGKI-mutant mice. Our analyses revealed significantly lower amounts of noradrenaline in BAT of cGKI-brain KO mice under basal conditions. Yet, the levels of UCP-1 and TH were not different between the two groups.

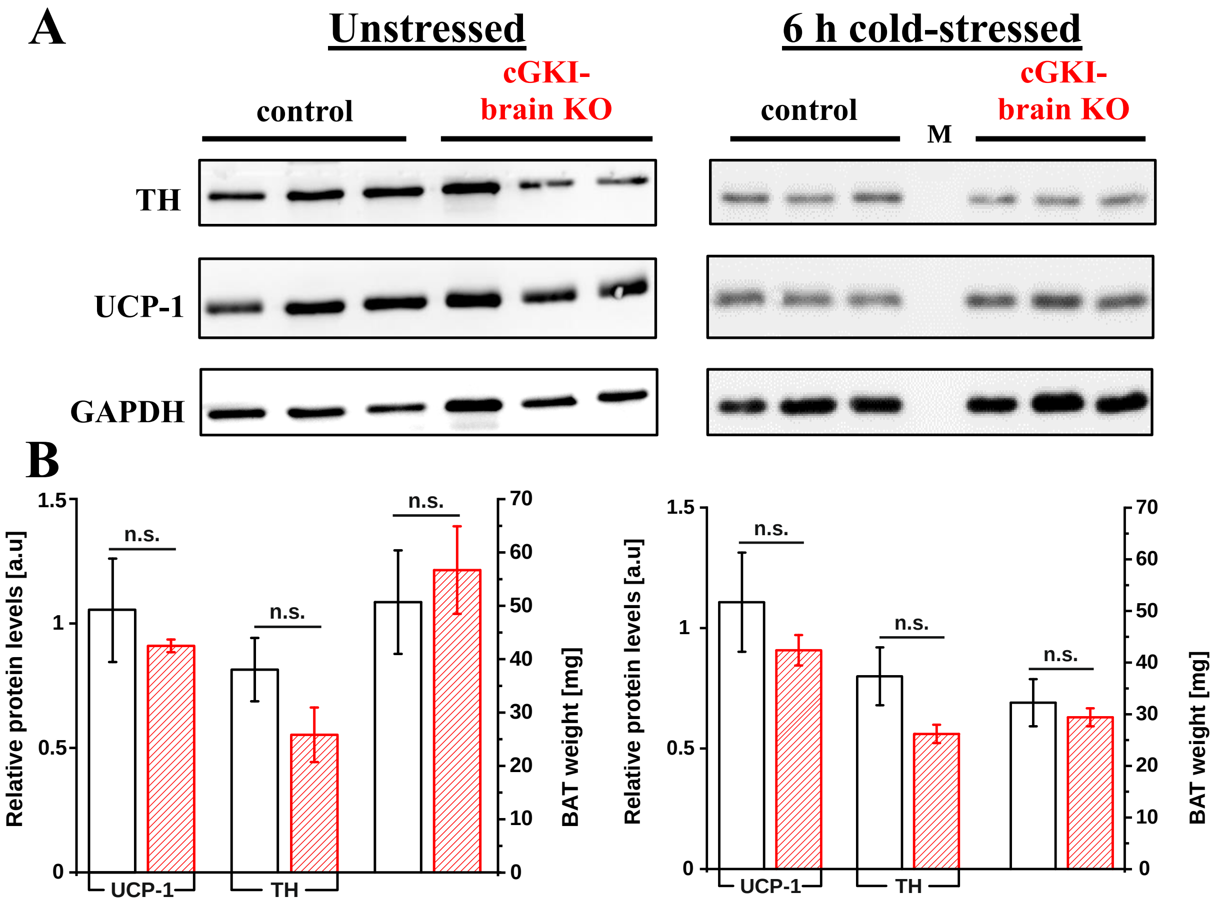

Figure 20. Western blot analysis of UCP-1 and TH in BAT of unstressed and cold-stressed female mice.

(A) Western blot images showing analysis of BAT samples of 9-10 week-old, unstressed, female mice (controls: Nes-Cre$^{tg/+}$ x cGKI$^{+/L2}$, n= 3, and cGKI-brain KO, n= 3), and of 24-34 week-old, female mice after 6 hours of cold-stress (controls: Nes-Cre$^{tg/+}$ x cGKI$^{+/L2}$, n= 3, and cGKI-brain KO, n= 5). 25 µg of protein were separated on 12% SDS gels and electroblotted on a PVDF membrane. The top row shows the levels of TH (≈ 62 kDa), the middle row of UCP-1 (≈ 32 kDa), and the bottom one that of GAPDH (≈ 37 kDa). (B) Densitometric evaluation of UCP-1 and TH levels shown in the Western blot in A and weight of whole-BAT of animals participated in the experiment. Analysis was performed with ImageJ. The same square was used to determine the intensity of bands across the images. Background was subtracted from values, TH and UCP-1 intensities were normalised to the intensities of the respective GAPDH band. Data represent mean values ± SEM. Statistical significance was tested with a Student’s t-test. n.s. not significant.

C.5 Analysis of cell populations found in BAT and the adrenal glands

Our staining experiments have previously revealed numerous cGKI-positive cells scattered among brown adipocytes of BAT and CORT-producing cells of the adrenal cortex (see **C.1.2** and **C.2**, respectively). We performed additional, ex vivo experiments such as FRET-based cGMP measurements and antibody stainings of cryosections, to shed light on the identity and possible function of these cell populations in the two organs.

C.5.1 FRET-based cGMP measurements in BAT and adrenal gland cultures.

The experiments described in this section were carried out with primary cultures from BAT or adrenal glands, generated from mice expressing the FRET-based cGMP biosensor cGi500 (discussed in sections **A.7.2** and **B.2.2**).

C.5.1.1 FRET-based cGMP measurements in BAT cultures from Npr2-LacZ x R26-cGi500(L1) mice

BAT was harvested from Npr2$^{LacZ/+}$ x R26-cGi500$^{+/L1}$ or Npr2$^{LacZ/LacZ}$ x R26-cGi500$^{L1/L1}$ mice (see **B.2.2**) and cells were isolated according to the protocol presented in section **B.2.4.1**. Dissociated, single cells were grown on coverslips on standard Dulbecco’s Modified Eagle Medium (DMEM) for 6 days, while the FRET measurement was performed on exactly day 7, as described in section **B.7.1**. Cells were stimulated sequentially with three different cGMP-elevating drugs: 500 nM of DEA/NO, 250 nM of ANP, and 250 nM of CNP. **Figure 21 A** shows a field of view from a typical FRET measurement, where the ROIs (and at the same time, the cell borders) are indicated in various colours according to the cell’s response. All recorded cells responded to stimulation with 250 nM CNP by generating cGMP (82/82). 57 cells (70%) responded to CNP only (**Figure 21 A**, **Group A**), 13 cells (16%) also to ANP along with CNP but not to DEA/NO (**Figure 21 A**, **Group C**), and 12 cells (14%) to DEA/NO, ANP, and CNP (**Figure 21 A**, **Group B**).

As expected, cells that bore a mutated gene of Npr2, the CNP receptor (Npr2$^{LacZ/LacZ}$), did not respond to CNP stimulation (**Figure 21 B**). However, all recorded cells generated cGMP after stimulation with 500 nM of DEA/NO (27/27), while one cell (cell no: 9) exhibited cGMP transient signals after sequential addition of 500 nM of DEA/NO and 250 nM of ANP (**Figure 21 B**).

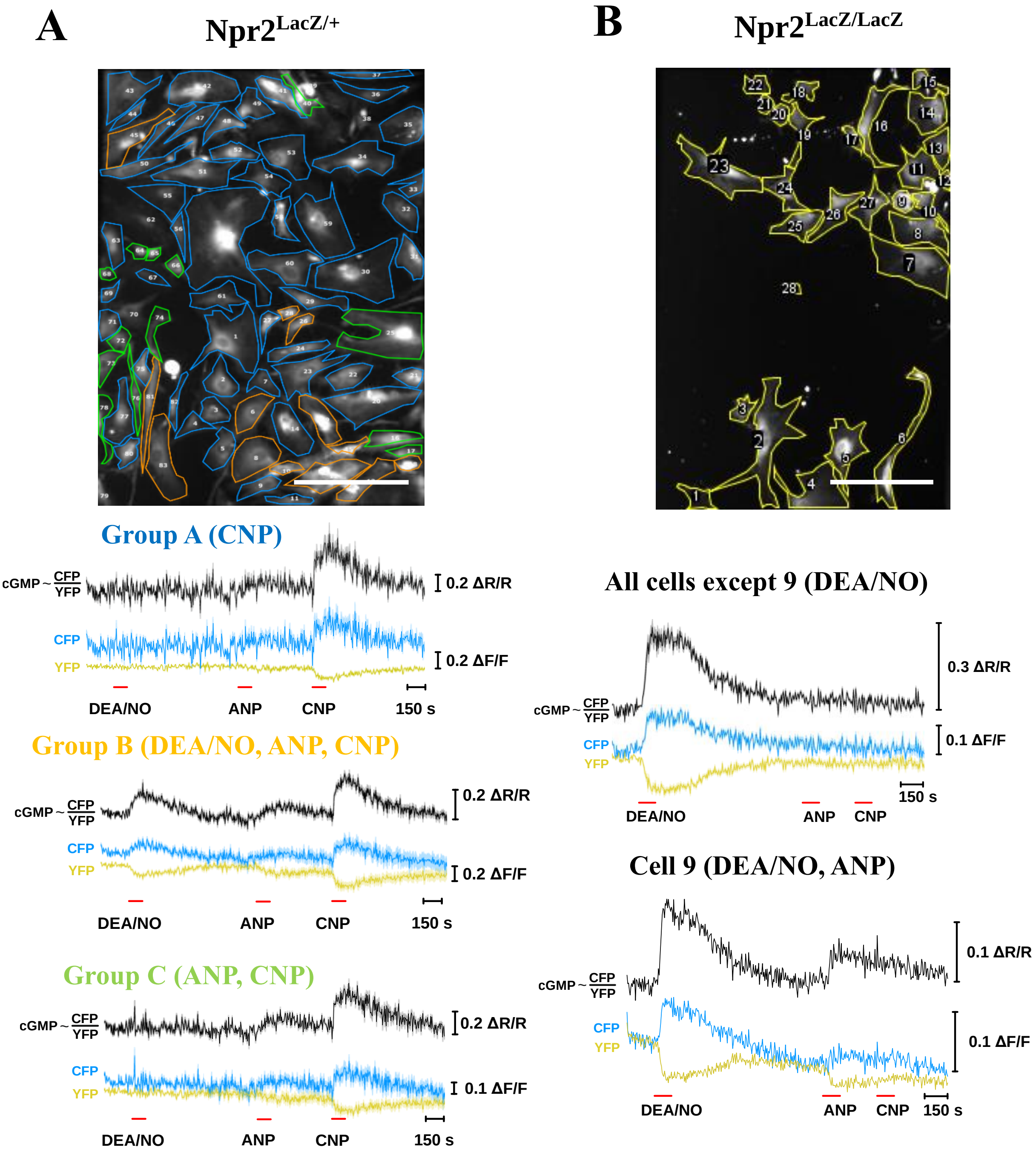

Figure 21. FRET-based cGMP measurement over time in cell cultures isolated from the BAT of Npr2-LacZ x R26-cGi500 mice.

Cells were isolated from BAT of 3-4 week-old, male Npr2$^{LacZ/+}$ x R26-cGi500$^{+/L1}$ or Npr2$^{LacZ/LacZ}$ x R26-cGi500$^{L1/L1}$ mice and cultured as described previously (see **B.2.4.1**). FRET measurements were conducted on day 7 with no serum starvation at any point prior to them. cGMP-elevating drugs (DEA/NO 500 nM, ANP 250 nM and CNP 250 nM) were added to imaging buffer in the indicated final concentration. Black, cyan, and yellow traces represent the CFP/YFP ratio, equal to cGMP, CFP emission, and YFP emission, respectively. Scale bars represent the change in fluorescence of the single fluorophores CFP or YFP (ΔF/F) or their ratio (CFP/YFP; ΔR/R reflecting [cGMP]i). Cells with similar responses were pooled, analysed and presented together as mean values (central trace) ± SEM (faded area). (A, top row) Field of view (10X). The ROIs are outlined in different colours in accordance with the cell's response. (A, bottom row) FRET-based cGMP measurements under continuous superfusion with imaging buffer. Group A represents a cluster of 57/82 cells that showed cGMP elevation after stimulation with CNP, group C 13/82 cells that additionally exhibited an ANP-induced cGMP signal and lastly, group B consisting of 12/82 cells that were able to elicit a cGMP signal upon stimulation with all three cGMP-elevating drugs (n=82 cells measured on one coverslip obtained from one culture). (B, top row) Field of view (10X) with marked ROIs. (B, bottom row) Depicted here is a group of 26/27 cells that showed cGMP elevation after stimulation with DEA/NO only. A single cell (no. 9) additionally exhibited an ANP-induced cGMP signal along with the DEA/NO-evoked cGMP elevation (n=27 cells measured on one coverslip obtained from one culture). Scale bars 50 µm.

C.5.1.2 FRET-based cGMP measurements in BAT cultures from Nes-Cre$^{tg/+}$ x R26-mT/cGi500$^{+/L2}$ mice

After having examined the responses of "wild type" cells in BAT cultures (Npr2$^{LacZ/+}$), cultures, where Nes-Cre drives the expression of the FRET-based cGMP sensor cGi500 were established to investigate the response pattern of the recombined cells. Stimulation with cGMP-elevating drugs was done as previously. Just before the end of each experiment, a control stimulation with 500 nM of DEA/NO was performed to ensure viability of the cells. Below, typical response patterns from two experiments are presented (**Figure 22**). At the end (**Figure 23**), a statistical analysis of all performed experiments is given.

BAT-derived, Nes-Cre-positive cell populations exhibited a fairly variable response pattern. **Figure 22** depicts two experiments, in which cells can be clustered into groups, based on their cGMP generation upon stimulation with DEA/NO, ANP and CNP. In the left panel A, nearly all cells (14/15) reacted to DEA/NO and CNP, while one single cell reacted to DEA/NO only (**Figure 22 A**). In the right panel B, cells showed preference for either ANP or CNP, along with their response to DEA/NO. For instance, 3/7 cells reacted strongly to DEA/NO and moderately to CNP, but very weakly, if at all, to ANP (**Figure 22 B**, **Group A**), while 4/7 cells showed preference for ANP along with a strong response to DEA/NO (**Figure 22 B**, **Group B**).

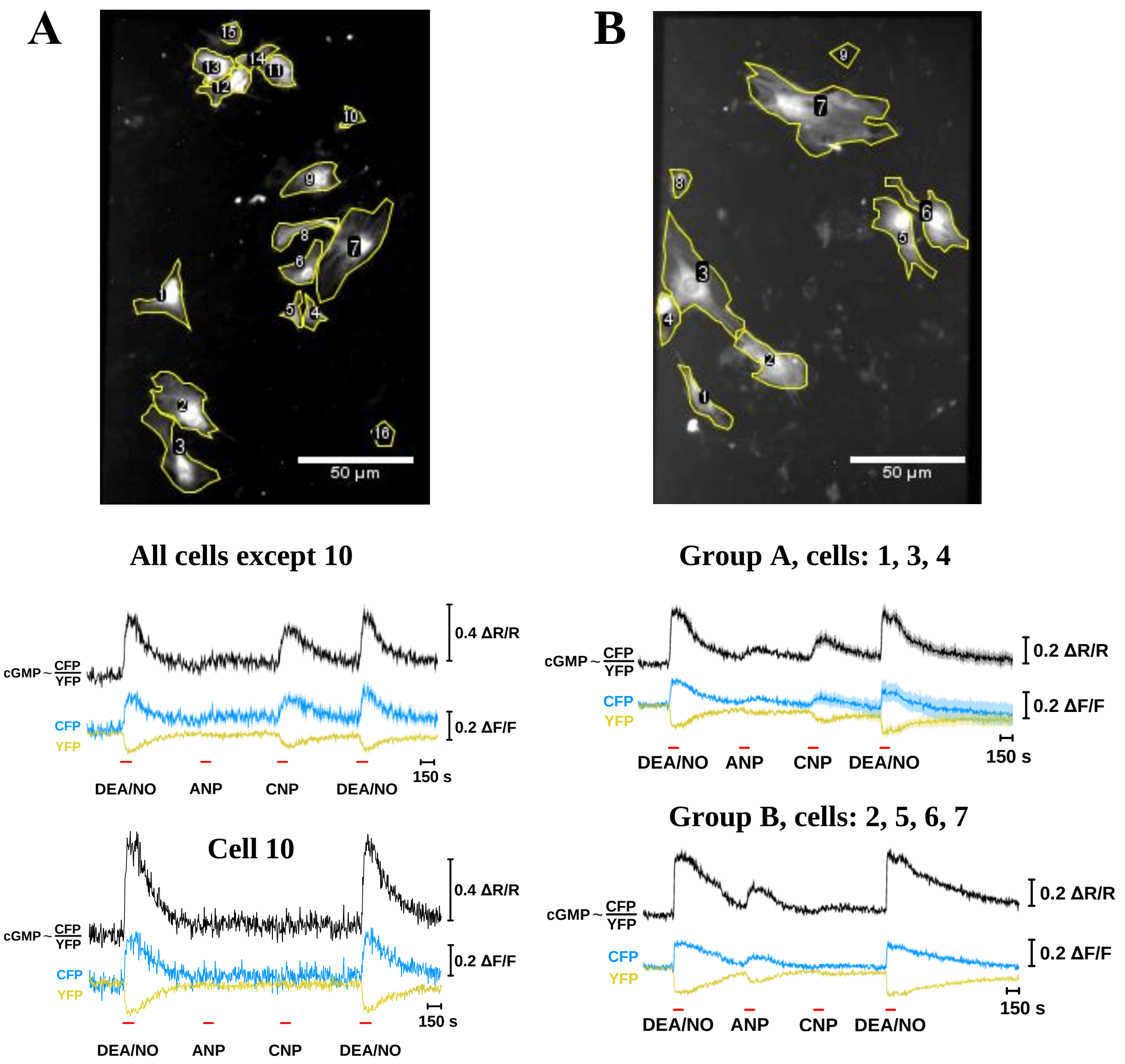

Figure 22. FRET-based cGMP measurement over time in a cell culture isolated from BAT of a 9 week-old Nes-Cre$^{tg/+}$ x R26-mT/cGi500$^{+/L2}$ female mouse.

FRET measurements were conducted on day 7 with no serum starvation at any point prior to them. The confluence of cells on the coverslip was at around 80%, while recombination appeared to be approximately 4%, after determination of the recombined (green) cells on the total cells on a coverslip. Recombined cells were grown in an “islet” pattern, probably clonally from a founder cell. The following cGMP-elevating drugs DEA/NO 500 nM, ANP 250 nM and CNP 250 nM were added to the imaging buffer in the indicated final concentration. Black, cyan, and yellow traces represent the CFP/YFP ratio equal to cGMP, CFP emission, and YFP emission, respectively. Scale bars represent the change in fluorescence of the single fluorophores CFP or YFP (ΔF/F) or their ratio (CFP/YFP; ΔR/R reflecting [cGMP]i). Cells with similar response were pooled, analysed and presented together as mean values (central trace) ± SEM (faded area). (A and B, top row) Field of view of the coverslip measured, where the ROIs are marked. (A and B, bottom row) FRET-based cGMP measurements under continuous superfusion with imaging buffer. Scale bars 50 µm.

Overall, FRET-based cGMP measurements in BAT cultures showed a complex response pattern. Literally, every response combination was possible to occur. In **Figure 23** below, all experiments were summarised in a pie chart. It becomes apparent that the vast majority of the cells (64%) responded to CNP, either with or without a DEA/NO and ANP response. Interestingly, 16% of the cells were able to generate cGMP solely after addition of DEA/NO, while another 5% of the total cells were weakly responsive to ANP along with DEA/NO.

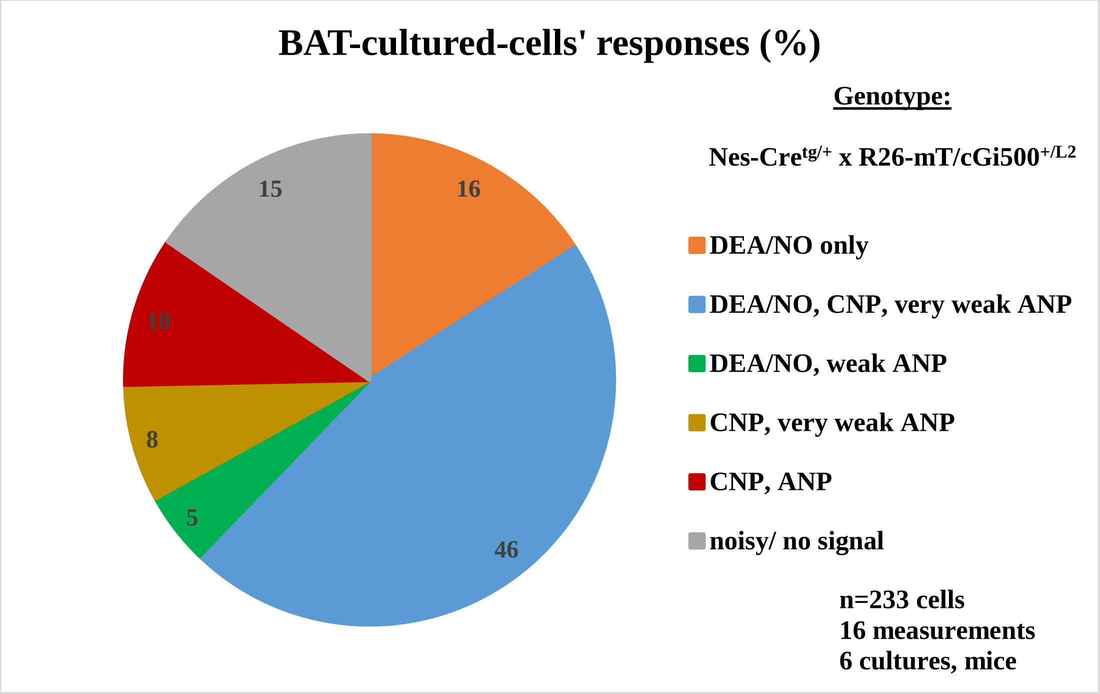

Figure 23. Overview of the responses of BAT-cultured cells from Nes-Cre$^{tg/+}$ x R26-mT/cGi500$^{+/L2}$ mice.

Cells were classified into various categories according to their response to the cGMP-stimulating drugs DEA/NO, ANP, CNP. The vast majority of cells responded to stimulation with CNP along with or without ANP and DEA/NO. A moderate amount of cells (16%) only presented elevated cGMP levels upon addition of 500 nM of the NO-donor DEA/NO, while the least cells (5%) had a preference to ANP combined with a DEA/NO reaction. Overall, a total of 233 cells, from 16 coverslips, originating from 6 independent cell cultures have been analysed.

C.5.1.3 FRET-based cGMP measurements in adrenal gland cultures from a R26-cGi500$^{+/L1}$ mouse

To be able to compare with the BAT cultures, we established cell cultures from the adrenal glands of mice. Cultured cells from the adrenal glands of a 44 week-old, female mouse that expressed the cGi500 sensor globally (**Figure 24 A**) exhibited a marked ANP preference. ANP transients were accompanied by responses to DEA/NO and CNP, as shown in **Figure 24 B**, **Group A**, or by only DEA/NO signals (**Group B**). A third **Group C** exhibited weak cGMP signals upon stimulation also with CNP.

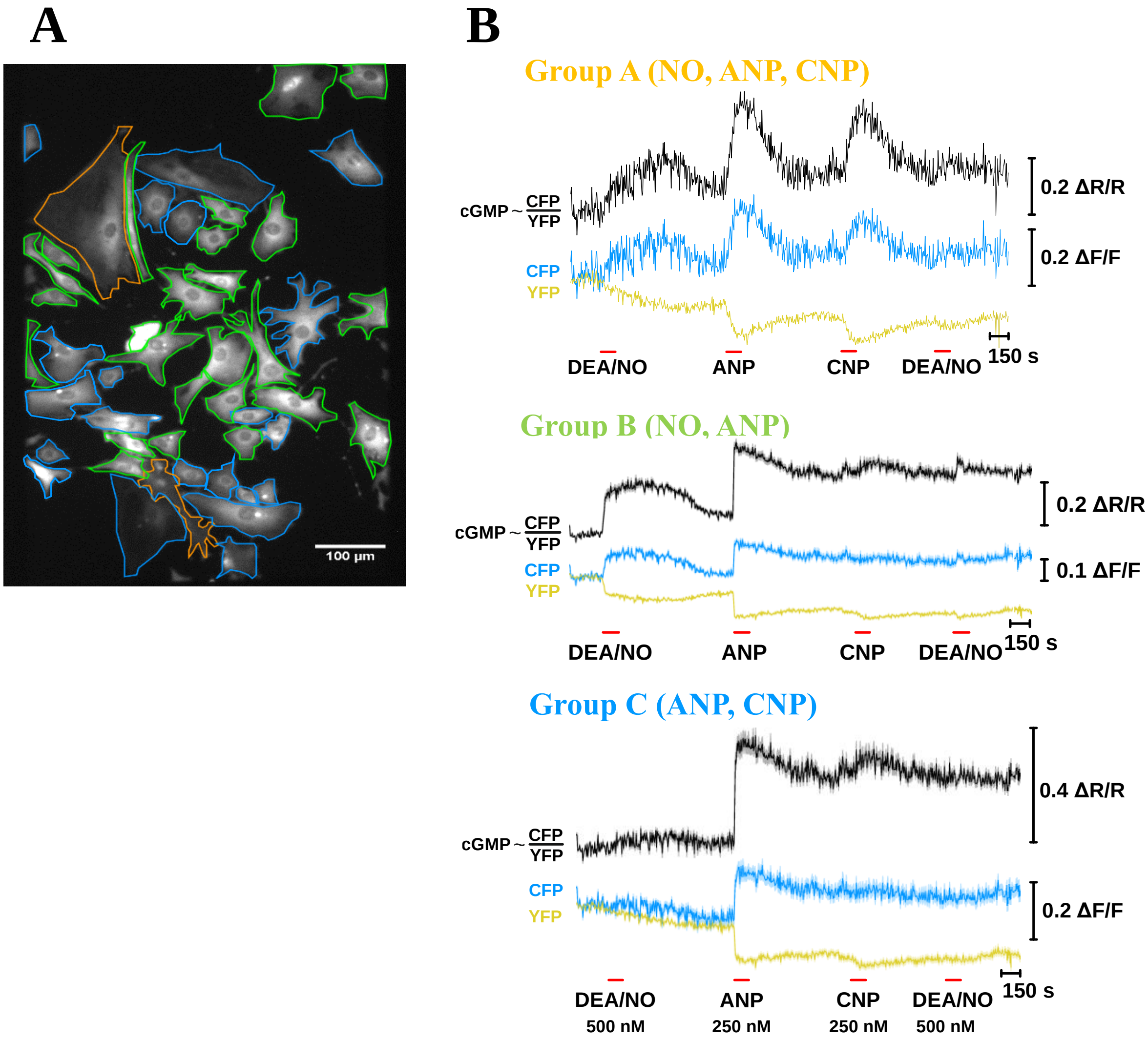

Figure 24. FRET-based cGMP measurement over time in a cell culture from the adrenal glands of a 44 week-old R26-cGi500$^{+/L1}$ female mouse.

(A) Field of view of the coverslip measured, where the ROIs are marked in different colours according to the cell's response pattern. (B) FRET measurements under continuous superfusion with imaging buffer. The following cGMP-elevating drugs DEA/NO 500 nM, ANP 250 nM and CNP 250 nM were added to the imaging buffer in the indicated final concentrations. Black, cyan, and yellow traces represent CFP/YFP ratio equal to cGMP, CFP emission, and YFP emission, respectively. Scale bars represent the change in fluorescence of the single fluorophores CFP or YFP (ΔF/F) or their ratio (CFP/YFP; ΔR/R reflecting [cGMP]i). Cells that showed similar responses, were pooled, analysed, and presented together as mean values (central trace) ± SEM (faded area). Scale bar: 100 µm. These preliminary data represent one single experiment, of one culture, and therefore need to be replicated, before someone can draw conclusions about the responses of adrenal gland cells.

C.5.1.4 FRET-based cGMP measurements in vibratome sections of BAT

Cells can undergo severe phenotypic modulations under culture conditions, by up- or down-regulating a number of their genes in order to adjust to their new conditions. For that reason, cell cultures do not always reflect the native situation, namely the behaviour of a certain cell when being in its natural (micro)-environment. To mimic those conditions, we performed FRET-based cGMP measurements on vibratome slices with the use of spinning-disk, confocal microscopy.

BAT, vibratome slices from a Nes-Cre$^{tg/+}$ x R26-mT/cGi500$^{+/L2}$ mouse were stimulated with all three cGMP-elevating drugs, as in the previous experiments. An unambiguous change of the FRET signal by about 15% compared to the baseline, was observed after addition of 100 µM of the NO-donor DEA/NO (**Figure 25**). Here, it is worth noting that these recordings were very difficult, due to the rapid movement of the tissue after the DEA/NO addition, which drifted the setup out of focus. Thus, albeit we haven't observed a clear cGMP response to either ANP or CNP, these results must be treated with caution.

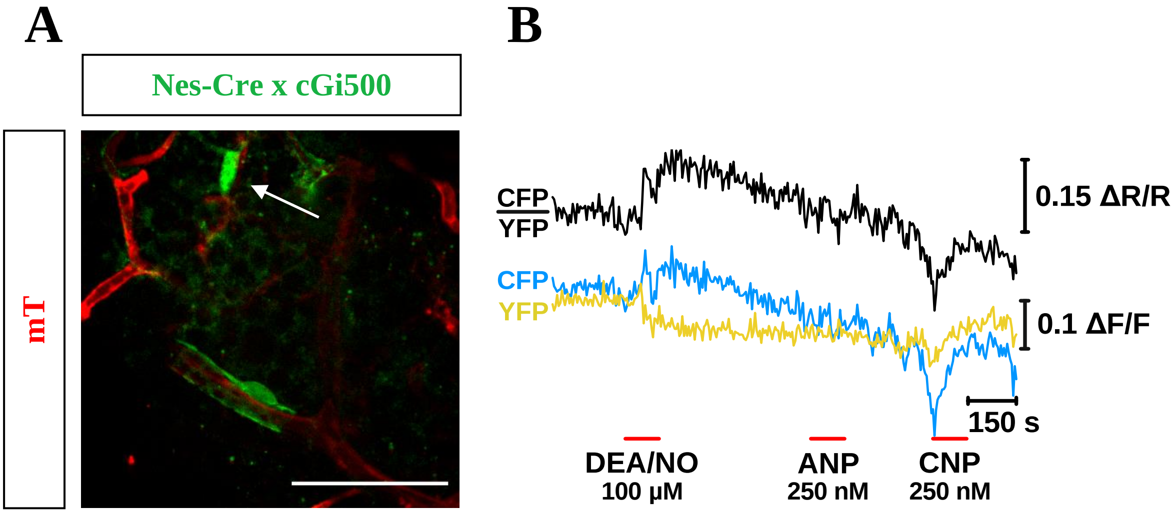

Figure 25. Representative FRET-based cGMP measurement over time on a vibratome, BAT slice of a 33 week-old, Nes-Cre$^{tg/+}$ x R26-mT/cGi500$^{+/L2}$ male mouse.

The FRET measurement was performed on a 300 µm-thick vibratome, BAT slice from a 33 week-old male Nes-Cre$^{tg/+}$ x R26-mT/cGi500$^{+/L2}$ mouse. (A) A confocal spinning-disk image showing the field of view of the area measured. Nes-Cre-positive cells are shown in green, while in red is shown the fluorescence of the mT of the non-recombined structures. (B) FRET-based cGMP measurement performed with a spinning-disk, confocal setup with 40 X magnification under continuous superfusion with pen-warmed Ringer's buffer (60 ml/h). The specimen was illuminated for 200 ms with a laser beam capable of emitting at 445 nm (31% laser intensity). Images of CFP and YFP emission were acquired with a QUANTEM camera at 5-sec intervals. Black, cyan, and yellow traces represent CFP/YFP ratio equal to cGMP levels, CFP emission, and YFP emission, respectively. Scale bars represent the change in fluorescence of the single fluorophores CFP or YFP (ΔF/F) or their ratio (CFP/YFP; with ΔR/R reflecting [cGMP]i). 100 µM of DEA/NO and 250 nM of either ANP or CNP were applied to the slice by addition into the buffer solution. The white arrow pinpoints a Nes-Cre-positive cell among brown adipocytes. ANP and CNP did not elicit a clear signal. In total 8/12 conical cells showed similar results. Depicted here a representative experiment from 12 vibratome slices obtained from 5 independent experiments. Scale bar 40 µm.

C.5.2 Characterisation of cGKI-positive cells in BAT and adrenal gland via immunostaining

Fluorescent immunostaining techniques were employed in an attempt to characterise the conical, cGKI-positive cells that were found in BAT between brown adipocytes and in the adrenal cortex, scattered among the CORT-producing cells.

C.5.2.1 Colocalisation studies of cGKI with various markers in BAT

Different markers were applied in co-stainings with cGKI, to identify the cell type of cGKI-positive cells in BAT. An anti-αSMA antibody presented clear, positive signals in a blood vessel found in BAT, shown in **Figure 26 A**. In that blood vessel, αSMA expression colocalised with cGKI expression (**Figure 26 C**). Yet, there was no colocalisation of αSMA with cGKI in the conical cells (**Figure 26 C**, white arrows). Next, the neuronal markers 3A10 and RMO were used. These stained the sympathetic nerve bundles innervating BAT nicely, as seen in **Figure 26 D**, **J,** and colocalised with cGKI therein (**Figure 26 F**, **L**, lower part, white arrows). However, the conical cells were not double-positive for 3A10, RMO and cGKI (**Figure 26 F**, **L**, upper part, white arrows). The endothelial cell marker CD31 revealed the dense network of the microvasculature present in BAT (**Figure 26 G**), however, again, conical, cGKI-positive cells exhibited no double stain with CD31 (**Figure 26 I**).

These data indicated that the conical, cGKI-positive cells in BAT were not of smooth-muscle, neuronal, or endothelial cell origin.

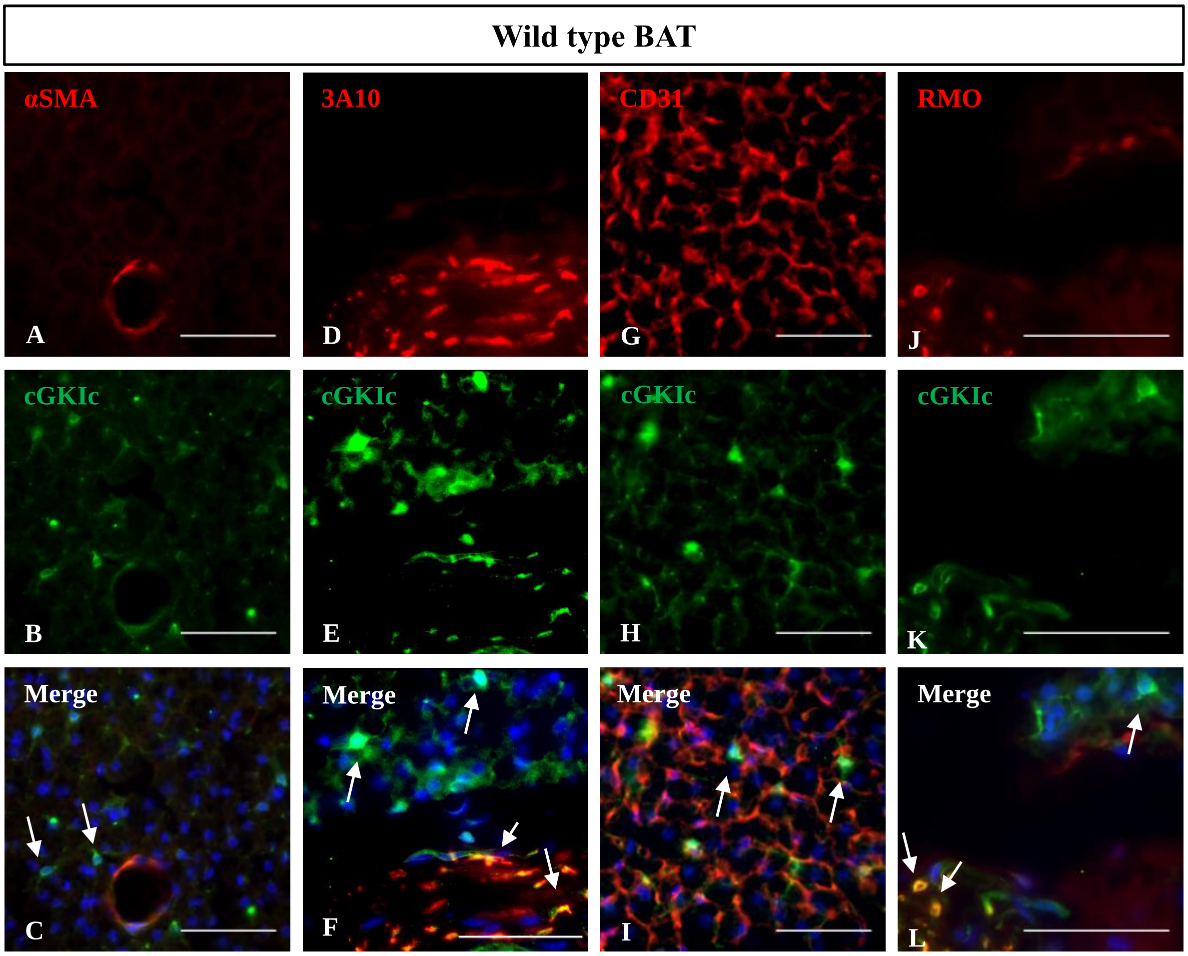

Figure 26. Colocalisation studies in wild type BAT.

Cryosections of wild type BAT of both genders were stained with an anti-cGKI common antibody (here visualised in green with an AlexaFluor® 488 secondary antibody) and markers for different cell types (visualised in red, with appropriate AlexaFluor® 555 secondary antibodies). Nuclei seen in blue, in row C-L, were counterstained with Hoechst 33258. Scale bars 50 µm

C.5.2.2 cGKI-positive cells in BAT express markers for pericytes

In our FRET experiments, Nes-Cre-positive cells on vibratome sections demonstrated cGMP-signals upon stimulation with DEA/NO. Here, with the use of an antibody against the NO-GC, we showed that cGKIα completely colocalised with NO-GC in blood vessels (**Figure 27 C**), and in the conical cells (**Figure 27 F**). The latter also expressed the platelet-derived growth factor receptor beta (PDGFRβ), which is commonly used as a marker for pericytes (**Figure 27 L**) [204, 205]. PDGFRβ was confined to the periphery of the cell (PDGFRβ is a membrane receptor) (**Figure 27 J**), while cGKIα stained the cytosol evenly (**Figure 27 K**). Blood vessels in BAT also demonstrated expression of PDGFRβ in the external vessel layer (tunica externa) (**Figure 27 G**), while cGKI was detected in the vascular media that contains VSMCs (**Figure 27 H, I**).

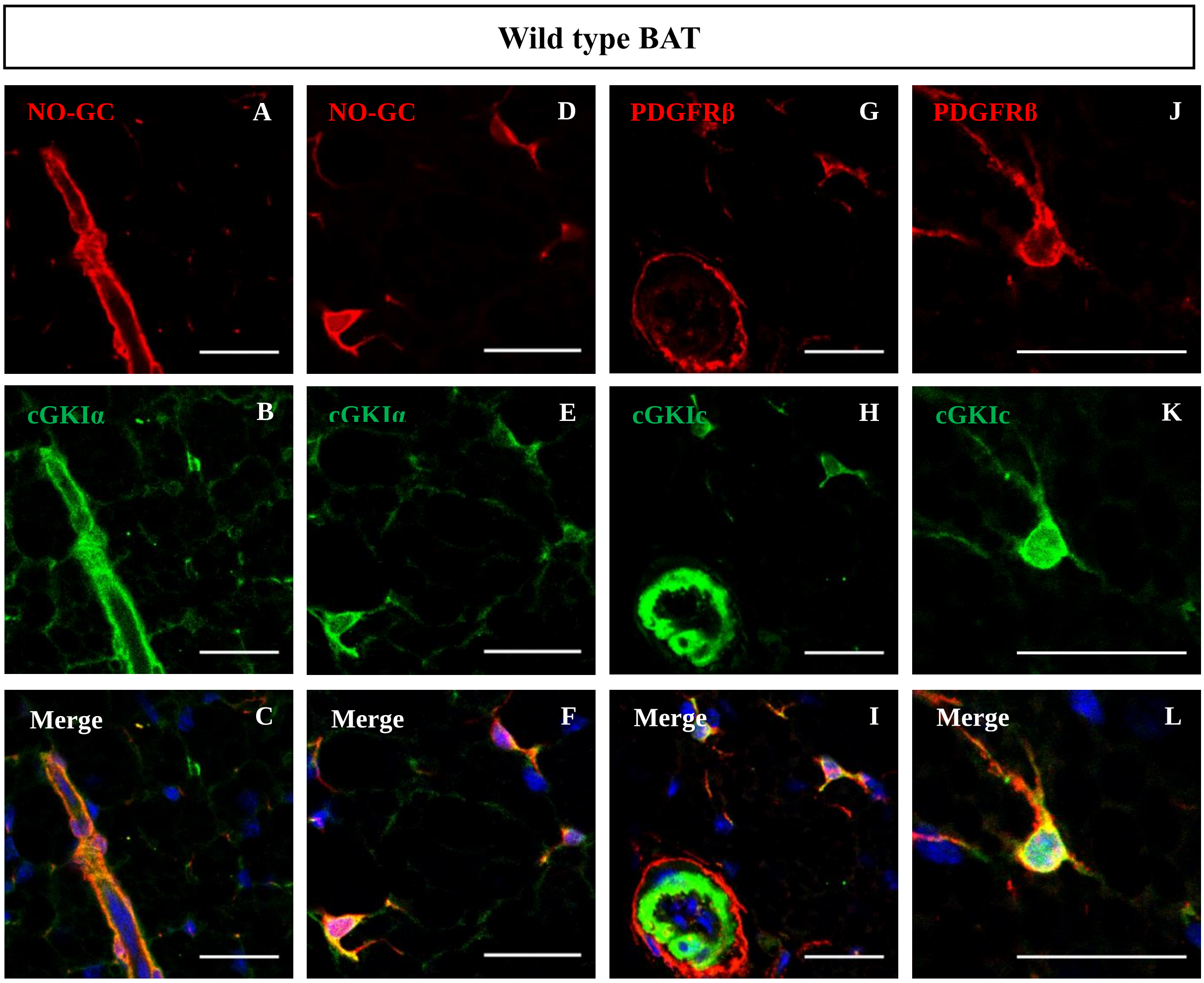

Figure 27. Representative laser-scanning microscope micrographs of wild type BAT showing expression of NO-GC, cGKIα, and PDGFRβ.

Wild type BAT cryosections of a 6 week-old, male mouse were stained overnight with a guinea pig polyclonal anti-cGKIα antibody (visualised with a guinea pig AlexaFluor® 488 secondary antibody) and a rabbit polyclonal antiserum against NO-GC (visualised with a rabbit AlexaFluor® 555 secondary antibody). Sections were also stained with a goat polyclonal PDGFRβ antiserum (visualised in red with a goat AlexaFluor® 594 secondary antibody) and a rabbit polyclonal common cGKI (visualised in green with a rabbit AlexaFluor® 488 secondary antibody). Nuclei in the lower row (C-L) were counterstained with Hoechst 33258. Scale bars 25 µm

C.5.2.3 cGKI-positive cells in the adrenal gland cortex express a marker for pericytes

To identify the cGKI-positive cells in the adrenal gland cortex, a similar procedure as in BAT was followed. We combined the goat-derived PDGFRβ antibody once with the rabbit cGKI common, and another time with the rabbit NO-GC antibody. PDGFRβ was highly expressed in the adrenal capsule (**Figure 28 A**) and colocalised with NO-GC (**Figure 28 C**). Cells scattered in the adrenal cortex were also double-positive for PDGFRβ and NO-GC (**Figure 28 F**). Moreover, cGKI-positive cells in the adrenal cortex were additionally positive for PDGFRβ (**Figure 28 L**). Based on our staining combinations, we infer that conical cells found in the adrenal cortex express cGKI, NO-GC and PDGFRβ. Our analyses of these cells demonstrated the existence of an NO-GC→cGMP→cGKI signalling pathway, while the expression of PDGFRβ marker classified them as pericytes.

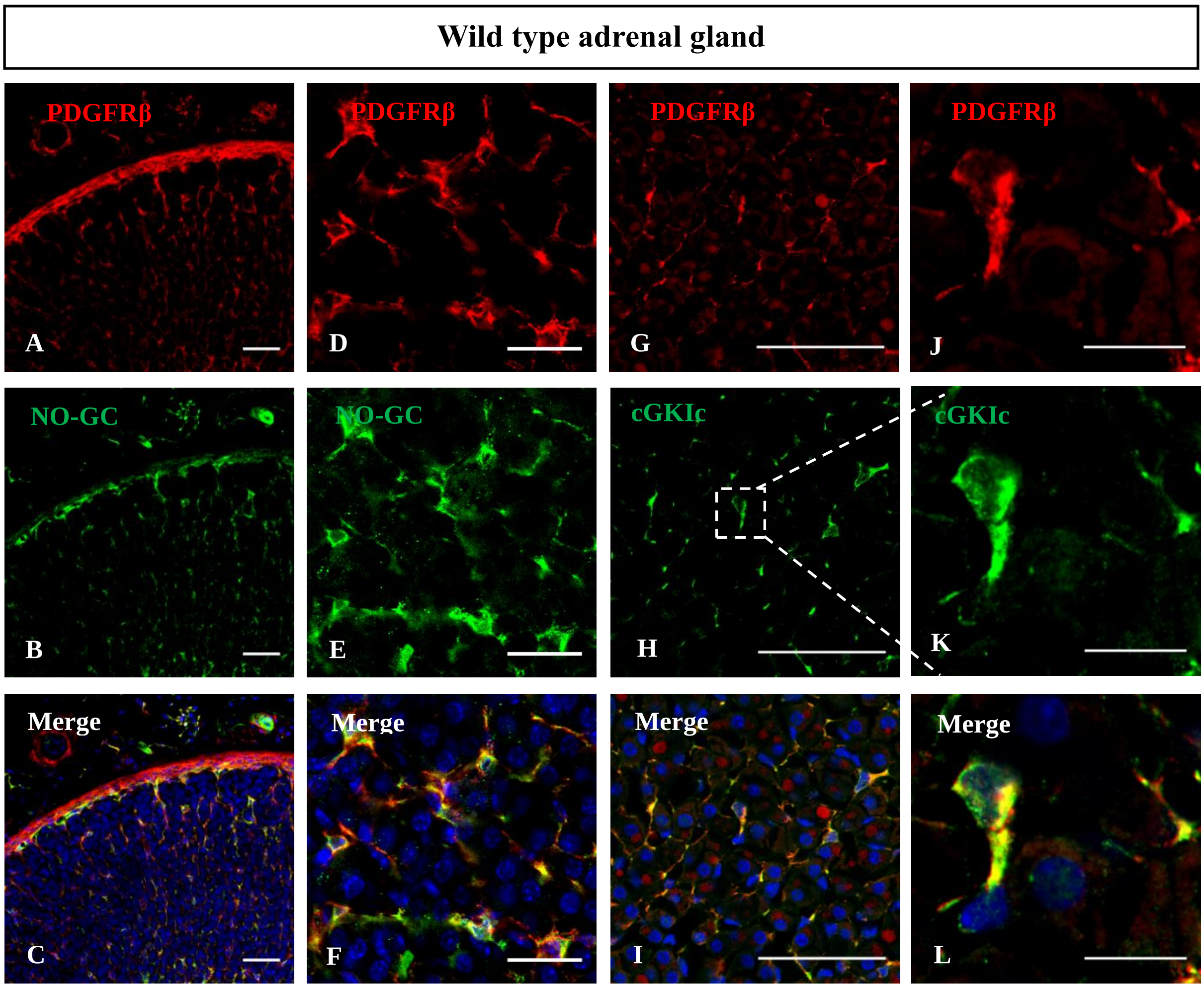

Figure 28. Representative laser-scanning microscope images of colocalisation studies with cGKI, PDGFRβ and NO-GC in wild type adrenal gland cortex sections.

Wild type adrenal gland cryosections of a 6 week-old male mouse were stained overnight with a goat polyclonal PDGFRβ antiserum (visualised in red with a goat AlexaFluor® 594 secondary antibody) and sequentially with either a rabbit polyclonal anti-cGKI common antibody or with a rabbit polyclonal antiserum against the NO-GC (both visualised with a rabbit AlexaFluor® 488 secondary antibody). Nuclei seen in the lower row (C-L) were counterstained with Hoechst 33258. Scale bars: A-C 50 µm, D-F 25 µm, G-I 50 µm and J-L 10 µm.

D. Discussion

D.1 Expression of cGKI in the organs of thermogenesis

The cGMP signalling pathway first emerged for its importance in the regulation of cardiovascular homeostasis and phototransduction [1], but it is now widely appreciated for its significance in a broad spectrum of (patho-) physiological processes. The most prominent of those well-established processes are: i) neuronal plasticity, subsequently involved in the modulation of learning and memory [5], ii) cell growth and survival (of VSMCs for instance), implicated in cardiovascular diseases such as atherosclerosis, and iii) platelet aggregation, which is associated with potentially severe thrombotic anomalies [5, 58]. Recently, the cGMP signalling pathway has been postulated to be involved in the modulation of the HPA-axis response [104, 105, 107, 108] and also in the regulation of thermogenesis [146, 147]. Yet, the exact cellular and molecular mechanism of how cGMP is involved in heat generation in BAT remains poorly understood. For that reason, in the present study, we addressed the questions of whether and how cGKI could be involved in cold-stress-evoked thermogenesis in mice.

Initially, we assayed the expression of cGKI in organs involved in thermogenesis such as the hypothalamus and BAT. We analysed lysates of the previously mentioned tissues via Western blot, which revealed a positive signal at the height of cGKI (~76 kDa) in both hypothalamus and BAT. That immunosignal was absent from the respective global cGKI knock out animals, confirming thus the specificity of our antibody (**Figure 9**). cGKI-brain KO animals exhibited complete ablation of cGKI in hypothalamic tissue-extracts, as evidenced by the absence of the respective cGKI signal in the Western blot (**Figure 9**). This finding was in accordance with previous studies, which had demonstrated the action of Nes-Cre in the entire CNS [188, 206]. BAT tissue extracts demonstrated a marked reduction of cGKI after the action of Nes-Cre. However, a small amount of cGKI was still detectable as a faint band in the Western blot (**Figure 9**). The weak, residual expression of cGKI in BAT could be, at least in part, attributed to the cGKI existing in VSMCs, which was not completely ablated by Nes-Cre, and furthermore to the cGKI of the conical cells, which also exhibited incomplete recombination by Nes-Cre (**Figure 11 B**). Thus, based on the broad expression of cGKI in BAT and the hypothalamus, it stands to reason that cGKI might well play a role in thermoregulation. Additionally, Nes-Cre line proved to be a well-suited mouse line for efficient ablation of cGKI in hypothalamus and BAT. As a consequence, the next step of this project was to determine the exact localisation of cGKI in the tissues of thermogenesis. Using the same specific common cGKI antibody as in the Western blots, a series of immunostainings were performed in brain and BAT sections (**Figures 10**, **11**). Although the overall expression levels of cGKI in hypothalamus had been reported to be rather low [57], higher amounts of cGKI were discovered in specific hypothalamic nuclei such as the dorsomedial hypothalamus (compact part, dorsal part) (**Figure 10 A**). This hypothalamic region is well-known for its implication in stressed-induced thermogenesis [129, 207]. Yet, the preoptic area of hypothalamus, which is postulated to be involved in body temperature regulation under non-stress conditions, demonstrated extremely low cGKI expression (**Figure 10**) (for a good review, see [124]). Furthermore, our analyses in BAT revealed cGKI in at least three regions of this organ: i) the nerve bundles innervating the tissue, ii) the VSMCs of the blood vessels, and iii) in small, conical cells with fine processes scattered among the brown adipocytes (**Figure 11**). Contrary to what has been previously reported [146, 148, 208, 209], we never observed cGKI expression in brown adipocytes (**Figure 11 A**), or in white adipocytes (data not shown) in any of our experimental procedures. This disagreement could be attributed to the usage of different cGKI antibodies. However, the specificity and sensitivity of our common cGKI antibody has been validated through countless experiments in over a decade. Our explanation for this discrepancy is that cGKI detected in wild type adipose tissues by our colleagues, comes from the conical cells, the VSMCs, or the nerve bundles found in brown (**Figure 11 A**, **C**) and white adipose (data not shown) tissues, and not from the actual adipocytes themselves, as described in Supplementary Figure S4 B of [148] or Figure 1 B of [209].

To study the expression of Cre recombinases, numerous reporter mice have been developed and are available for the researcher’s unique needs [170-172, 210]. These mouse models generally exploit the Cre/loxP recombination system to enable transcription and translation of a reporter gene after excision of an upstream cassette that blocks its expression [172]. Until the late '90s, various constructs encompassing the β-galactosidase gene had appeared that were functioning either alone [171], or in more sophisticated combinations with other genes such as the CAT/LacZ [211], or the LacZ/hAP [212]. However, these required complicated processing often extending over the course of several days, and their sensitivity could be easily compromised by various factors, such as the tissue thickness or the quality of the X-Gal solution. To circumvent these obstacles, fluorescent reporter mice have been developed to further facilitate research. These models require minimal post-experimental processing and even allow for real-time investigation of the cellular processes in living cells, tissues or animals. Typically, fluorescently-labelled tissues can be harvested, fixed and sectioned on the same day, hence minimising time, effort, and potential artefacts that may occur in the course of the otherwise long processing. For instance, a double fluorescent reporter mouse, generated by Muzumdar and colleagues, expresses a membrane-tagged red fluorescent protein (mT) before Cre-assisted recombination, that switches to a membrane-targeted EGFP protein after the mT has been removed [170]. In this way, it is feasible to distinguish between non-recombined, red-labelled and recombined, green-tagged cell populations. More elegant approaches that involve the usage of multiple colours in a random way have been also developed [213, 214]. In our studies, we made use of a Cre reporter line (R26-Ai14) that expresses a red fluorescent protein (td Tomato) after Cre-mediated excision of an upstream STOP cassette [172]. We crossed R26-Ai14 mice with a Nes-Cre line [188] to label nestin-expressing cells and their progeny, and harvested and analysed various organs including BAT and adrenal glands via epifluorescence microscopy. We have not performed co-expression analyses of Nes-Cre and cGKI in hypothalamus, as Nes-Cre should be highly expressed in this brain region [206, 215], and therefore should completely ablate cGKI from hypothalamus. BAT cryosections from a Nes-Cre$^{tg/+}$ x R26-Ai14$^{+/L2}$ mouse were subjected to epifluorescence microscopy that revealed activity of Nes-Cre in the same structures where we had previously detected cGKI expression. Moreover, this observation was also verified by co-staining with cGKI (**Figure 12**). Nes-Cre showed strong abundance in the blood vessels and peripheral nerve bundles innervating BAT (**Figure 12**, left image). The later exhibited intense staining for the neuronal marker βIII-tubulin (**Figure 11 E**) and also for tyrosine hydroxylase (data not shown). The majority of the conical, cGKI-positive cells were red, indicating Nes-Cre expression, at least, at a certain point earlier in their developmental course. The fact, that not all conical, cGKI-positive cells in BAT have been positive for Nes-Cre (**Figure 12** merge, white arrows) might explain the residual faint cGKI band in the Western blot of BAT from cGKI-brain KO mice (**Figure 9**) and also the residual green cells in **Figure 11 B**. Interestingly, we also observed conical, cGKI-positive cells in the adrenal gland cortex (**Figure 13 A**, square). In GKI-brain KO mice, cGKI in those cells was not ablated after the action of Nes-Cre (**Figure 13 B**). Indeed, our analyses of the adrenal glands from a Nes-Cre$^{tg/+}$ x R26-Ai14$^{+/L2}$ mouse indicated that there was no activity of Nes-Cre and simultaneous expression of cGKI in that conical cells, or in the adrenal cortex (**Figure 13 E**, merge). Our results contradicted those of Steenblock *et al.*, who identified Nes-Cre^{+} progenitor cells scattered throughout the adrenal cortex able to produce corticosterone upon stimulation with ACTH [216]. Contrarily, in our experiments, the adrenal medulla showed intense expression of Nes-Cre confirming thus its neuronal origin, but no signs of cGKI were observed there (**Figure 13 F**, merge). The absence of Nes-Cre expression in the adrenal cortex may also explain the absence of the impaired CORT production in cGKI-brain KO mice after IL-1β injection, which was shown by Gerling and colleagues [103].

D.2 In vivo examination of the Nes-Cre mouse line

After confirming the expression of cGKI in BAT and the hypothalamus, we examined its role in cold-stress-induced thermogenesis. With the help of the Cre/loxP system, we generated transgenic mice that lacked cGKI in the central and peripheral nervous system (cGKI-brain KO) and subjected them to a 4 °C cold-stress. We then monitored their body temperature with a digital thermometer via the rectum (rectal temperature). Initially, litter-matched, male mice of 40-44 weeks of age were randomly utilised in a 6-h cold-stress challenge. At the beginning of the assay, control and mutant mice exhibited almost identical body temperatures, and they were both able to stabilise it at around 31-32 °C for the first 3 h. At that time point, cGKI-brain KO mice displayed significantly lower body temperatures than control mice. After that, cGKI-brain KO mice showed a drop in body temperature later in the following hours. It plunged to lower than 30 °C, while that of the control mice remained well above 30 °C at the end of the cold-stress challenge (**Figure 14 A**). Nevertheless, although mutant mice showed a tendency towards exhibiting lower body temperatures under cold-stress compared to control mice, there was no statistical significance at the 4th, 5th and 6th hour. We believe that the lack of statistical significance could be explained by the low number of animals (n=3 for each group) used in this experiment. On the other hand, the body weight of control animals was significantly higher compared to that of knockout mice. The BAT weight nor the ratio of BAT to body weight were significantly different between the two groups (**Figure 14 B**).

Interestingly, in the last years, the use of the term “statistically significant” has gathered a great deal of attention and extensive discussions have been going on around it [217, 218]. According to Amrhein, scientists often misuse p-values to make unrealistic claims about their hypotheses or findings, so as to merely secure publishing of their data into scientific journals [219]. But forcing scientific results into a binary, “black or white” context, certainly does not reflect the complexity of the real world, let alone the complexity of biology. Publication bias has frequently pushed researchers to ignore interesting scientific data that do not meet the bar (of the 5%) or even manipulate them in order to surpass the publication criteria. In our particular context, we are not suggesting to ban statistics and p-values, but rather to reflect on the data in a more wise and open-minded way, trying to judge them in the context of the biology behind them. Hence, although the body temperature of mutant mice was not significantly lower in comparison to control mice at all time points, this tendency towards lower body temperatures might not be insignificant after all. Especially, for a small animal like the mouse, whose thermoneutrality zone lies at 30 °C [121, 122] and its normal body temperature at 36 °C [220].

To rule out the possibility that the trend towards altered thermoregulation observed in the cGKI-brain KO animals was solely due to body weight differences, we conducted a longitudinal study of their body weight. Males and females of various genotypes (Nes-Cre$^{+/+}$ x cGKI$^{+/L2}$, Nes-Cre$^{+/+}$ x cGKI$^{L1/L2}$, Nes-Cre$^{tg/+}$ x cGKI$^{+/L2}$, Nes-Cre$^{tg/+}$ x cGKI$^{L1/L2}$) were examined over a period of 13 weeks. We observed no significant differences between the genotypes Nes-Cre$^{+/+}$ x cGKI$^{+/L2}$ and Nes-Cre$^{+/+}$ x cGKI$^{L1/L2}$ or Nes-Cre$^{tg/+}$ x cGKI$^{+/L2}$ at any week in both genders (**Figure 15**). However, cGKI-brain KO mice (genotype: Nes-Cre$^{tg/+}$ x cGKI$^{L1/L2}$) of both sexes were significantly lighter than their Nes-Cre-negative counterparts (cGKI$^{+/L2}$ and cGKI$^{L1/L2}$) almost from the beginning of the study (week 6-13) (**Figure 15**). Most importantly, cGKI-brain KO mice of either gender demonstrated no significant body weight difference compared to their control mice (genotype: Nes-Cre$^{tg/+}$ x cGKI$^{+/L2}$) at any time during the study (**Figure 15**, comparison of red with the last black lines). It is worth noting, however, that male cGKI-brain KO and their control mice (genotype: Nes-Cre$^{tg/+}$ x cGKI$^{+/L2}$) displayed a peculiar "widening" between the line distance of their weight after week 11 (**Figure 15 A**). Here, although we did not follow their body weight in later stages beyond the 13th week of age, we speculate that this tendency might be the reason for the significant body weight difference observed in our "40-44 week-old" male mice in the previous cold-stress experiment (see **Figure 14**).

Thus, according to our analyses, the body weight of our mice is dependent on the Nes-Cre transgene and not on the number (one or two) of the cGKI alleles. Indeed, it has previously been reported that Nes-Cre-bearing mice display a mild hypopituitarism [188], which is responsible for their lighter weight in comparison to wild type mice. This phenotype arises from the existence of the human growth hormone (hGH) minigene downstream of the Cre recombinase, placed in there to achieve a higher expression level of the Cre transgene [221]. It is, hence, the expression of hGH in the hypothalamus that reduces the expression of hypothalamic growth hormone (GH)-releasing hormone (*Ghrh*) due to a negative feedback mechanism and leads to the GH deficiency. The researchers reported that three-month-old male Nes-Cre mice showed a significant decrease in the total body weight as compared to control littermates without the Nes-Cre transgene [221]. This finding could also explain the body weight discrepancies that we have observed in our first cold-stress experiment (**Figure 14 B**). Another study conducted by Galichet and colleagues compared various pituitary hormones before and after birth. They found that Nes-Cre mice had similar GH contents to the control mice before birth, but adult Nes-Cre mice displayed a 70-80% reduction in GH, prolactin (PRL) and thyroid-stimulating hormone (TSH) contents, while luteinizing hormone (LH) and adrenocorticotropic hormone (ACTH) levels were not affected [190].

Based on the above-mentioned reasons, we continued our body temperature analyses with female, body weight-matched mice, as female mice exhibited less body weight variances (**Figure 15 B**). Similarly to the previous cold-stress experiment with the male mice, a 6-h cold-stress challenge brought about the same outcome in weight-matched, female mice (**Figure 16 A**). Following a 6-h cold-stress challenge, female cGKI-brain KO mice had significantly lower body temperatures (time points t5 and t6) than control mice (**Figure 16 A**). Hence, we concluded that cGKI-brain KO mice display an impairment in body temperature regulation under cold-stress. This observation has been made in, at least, four independent experiments conducted in our lab by previous researchers (data not shown). During those experiments, the researchers made use of wireless thermometers implanted into the abdomen of the mice. The advantage of these thermometers was, that they were capable of simultaneously recording different body parameters such as the temperature and the activity of freely-moving animals. It is possible, that our experiments yielded slightly different results due to the different measurement method utilised (rectal via a digital thermometer vs core body temperature via wireless thermometers). Indeed, as described by Meyer *et al.*, thermometry in mice is a tricky procedure and requires adequate training and thorough planning [222]. For instance, rectal probing is subjected to procedural bias (insertion depth of the probe) and, therefore, is more suitable for preliminary studies. According to the authors, other methods including telemetric systems and BAT temperature probing systems are more appropriate for body temperature studies [222]. In the experiments performed in this work, locomotor activity was not monitored. Despite that, we couldn’t notice any visible behavioural difference between control and experimental animals. Nor can we claim that mice showed any sign of shivering, particularly in the initial phase of the cold-stress ordeal. That could be presumably attributed to the fact that our housing conditions (at 22 °C) already exposed mice to a continuous cold-stress, and therefore mice had already proceeded from shivering to non-shivering thermogenesis taking place in BAT. Recent studies postulate that the skeletal muscle apart from being a major energy expenditure organ (for example during exercise) also constitutes an important thermogenic organ involved in both shivering and nonshivering thermogenesis. Particularly in non-shivering thermogenesis, the skeletal muscle generates heat via futile Ca^{2+} cycling from the sarcoendoplasmic reticulum to the cytosol, via a sarcolipin/ sarcoendoplasmic reticulum calcium APTase (SERCA), depicted in **Figure 29** [223, 224]. In rodents, sarcolipin is an endogenous activator of SERCA, which uncouples Ca^{2+} transport from the hydrolysis of ATP, leading to an increase in the futile cycling of Ca^{2+} and heat production [225]. Interestingly, the thyroid hormone T3 has been shown to transcriptionally upregulate the expression of SERCA, via two thyroid hormone response elements, located in the promoter of this gene [226]. Elegant studies conducted by Rowland and colleagues have pinpointed the importance of both UCP-1 and SERCA for optimal thermogenesis and consequent survival of mice under cold-stress [227, 228]. In the present study, we haven't examined the role of skeletal muscles and thyroid hormones in heat production under cold-stress. However, deficits in the aforementioned systems may account for the observed cold-stress-induced phenotype in our cGKI-brain KO mice.

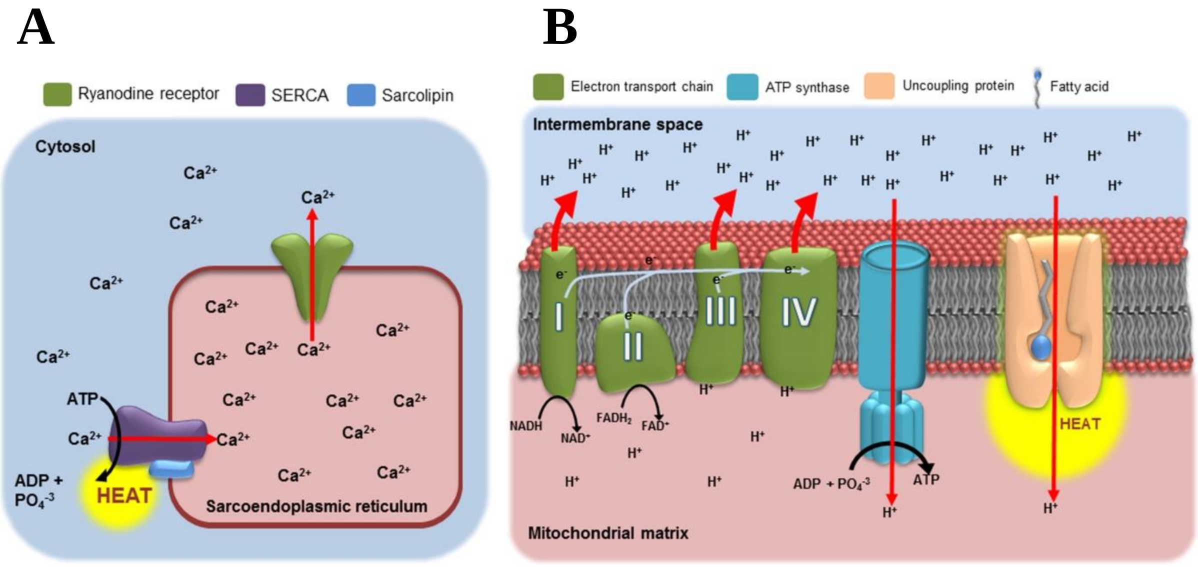

Figure 29. Comparison of the thermogenesis mechanisms in muscle and BAT.

(A) Schematic representation of futile calcium-cycling-mediated thermogenesis in the skeletal muscle. At rest, the passive leak of calcium from the sarcoendoplasmic reticulum (SR) occurs via the ryanodine receptor. To maintain intracellular calcium homeostasis, calcium is propelled back into the SR via the sarcoendoplasmic reticulum ATPase (SERCA) pump. The movement of calcium against the concentration gradient requires the hydrolysis of ATP which is a thermogenic process and produces heat. Sarcolipin is a key regulator of SERCA and activates thermogenesis via the futile calcium pathway. (B) Schematic of mitochondrial uncoupling and the cellular process of thermogenesis in BAT. Metabolic processes such as glycolysis, β-oxidation and the citric acid cycle contribute electrons through the nicotinamide adenine dinucleotide (NAD^+) and flavin adenine dinucleotide (FAD^+) carriers to the electron transport chain. The action of the electron transport chain (complexes I–IV) results in the pumping of protons across the inner mitochondrial membrane from the matrix into the intermembrane space and the establishment of the electrochemical gradient. Normally, this proton motive force is harnessed by ATP synthase to produce ATP from ADP. UCPs provide an alternative way through which protons can cross the inner mitochondrial membrane. Fatty acids activate UCPs by binding to a hydrophobic pocket within the protein that increases proton conductance. The leak of protons across the inner mitochondrial membrane results in the dissipation of energy through heat production. (Taken from [224])

PET is a powerful technique of particular importance in human diagnostics. Special PET scanners of smaller scale, dedicated for animal imaging studies have been already exploited for sophisticated analyses, in which the dynamic biodistribution of a radiolabelled compound is monitored over time non-invasively [229, 230]. PET scan comprises a great tool for complex brain analyses including elucidation of the mechanisms underlying brain disease or preclinical studies and basic research in neuropharmacology [231]. PET is also a potent method to assess normal biological processes, changes in biological processes under disease, or merely to monitor the response of healthy and diseased tissues to therapeutic intervention [230]. Previous studies have exploited the power of PET to study BAT activity with the use of [^{18}F]FDG (fluorodeoxyglucose) in mice [201] and humans [232].

Here, to assess the activity of BAT, we cold-stressed cGKI-brain KO and control mice in a custom-made apparatus and subsequently subjected them into analysis of [^{18}F]FDG biodistribution via PET. cGKI-brain KO mice exhibited a markedly reduced [^{18}F]FDG uptake in BAT compared to controls (**Figure 17 A**, **B**). Other metabolically active tissues such as the brain and the myocardium displayed no differences between controls and mutant mice (**Figure 17 D**), indicating a specific malfunction of BAT of cGKI-brain KO mice under cold-stress. It would have been unexpected though if glucose utilisation in the brain and heart had changed upon cold-stress, as these important tissues need to function stably irrespective of the animal's stress situation.

In general, heat generation in brown adipocytes via UCP-1 is dependent on free fatty acids derived either from brown adipocyte self-stores or from lipolysis of distant white fat depots [126, 128, 233]. In contrast to what was previously published, not only fatty acids but also glucose can be utilised for heat production, when fatty acids are unavailable for instance during fasting [234, 235]. In this scenario, glucose is transported into brown adipocytes by the glucose transporters GLUT1 (responsible for the basal glucose supply) and GLUT4 [155]. The insulin-regulated GLUT4 is predominantly expressed in the adipose tissue and skeletal muscles [200, 236] and becomes upregulated after exposure to cold, as shown for mice and rats [237-239]. Exercise or insulin can also trigger the rapid translocation of GLUT4 to the cell surface [236, 240]. Studies have moreover demonstrated, that glucose uptake via GLUT4 can contribute to a beneficial glucose homeostasis in mice and humans [241, 242]. Impaired radio-labelled glucose uptake in our PET scan analysis could be have been explained by reduced levels of glucose transporters in BAT. However, our Western blot analyses showed no differences in GLUT4 levels between unstressed, control and cGKI-brain KO mice (**Figure S2**). Furthermore, as GLUT4 is regulated by insulin, deficits in insulin levels could be accountable for improper GLUT4 regulation. Nevertheless, no insulin deficits were discovered in cGKI-brain KO mice in comparison to controls, as reported by Lutz and colleagues [243].

D.3 Noradrenaline levels in BAT of unstressed and cold-stressed mice

Previously, we examined the expression of cGKI in BAT of wild type and cGKI-brain KO animals (**Figure 11**). Given the abundant localisation of cGKI in the sympathetic nerve bundles of wild type mice, we hypothesised that ablation of cGKI therein via the activity of Nes-Cre (**Figure 11 D**) influenced noradrenaline content in the tissue. Compellingly, under basal conditions, we discovered much less noradrenaline in BAT of cGKI-brain KO mice compared to control mice (**Figure 18 A**). After 6 h of cold-stress, this tendency was still maintained, although not significant (**Figure 19 A**). It is quite unlikely that these noradrenaline differences emerged from BAT/body weight differences, as these measures were not different between the two groups (**Figure 18 D**, **19 D**). Altered noradrenaline levels could underlie deficits in its intraneuronal synthesis, and/or synaptic release. Secretion deficits and the role of Ca^{+2} were beyond the scope of this study, and therefore they still need to be investigated. Concerning synthesis, our Western blot analyses in BAT of mutant and control mice indicated no difference in the amount of TH, the rate-limiting enzyme participating in noradrenaline synthesis (**Figure 20**). TH is highly activated/deactivated by phosphorylation and dephosphorylation of several

Ser/Thr residues in the N-terminus, respectively. Phosphorylation at Ser19, for example, is vastly important and initiates binding to 14-3-3 proteins, which are well-known phosphorylation-dependent activators of TH [244]. Similarly, phosphorylation at Ser31 seems to control TH transport from the cell soma to the terminals using the microtubule network, where it is being targeted into the synaptic vesicles [245]. Moreover, a study by Toska *et al.* reported another phosphorylation site (Ser40) for TH and came also to the conclusion that phosphorylation at Ser19 causes an increase in the enzyme activity [246]. Based on the aforementioned studies, and given the fact that cGKI is a Ser/Thr kinase, it is tempting to speculate that TH activation in the sympathetic nerve terminals may rely on cGKI. As a result, the genetic ablation of cGKI may account for the diminished noradrenaline levels in BAT of cGKI-brain KO mice, via improper activation of TH.

Moreover, deficits in systemic noradrenaline levels are probably implausible. Our data show no expression of cGKI in the adrenal medulla (**Figure 13 F**), the main site of noradrenaline synthesis contributing to the systemic noradrenaline content. The role of macrophages in BAT thermogenesis, though, has been a matter of debate in recent years. Researchers in one group postulate that alternatively-activated macrophages can secrete noradrenaline that aids thermogenesis [247], while researchers in another group are claiming quite the opposite [248] (for an excellent review on the topic see: [249]). Interestingly, another study conducted by Pirzgalska *et al.* showed that macrophages residing in close proximity to the sympathetic nerves of BAT could internalise and degrade noradrenaline, rendering it thus unavailable to brown adipocytes [250]. However, whether that scenario, which involves macrophages in BAT-related thermogenesis, holds true in our case, still needs to be examined.

Insufficient noradrenaline levels could subsequently account for the diminished thermogenic capacity of BAT in cGKI-brain KO mice. Thermogenesis in BAT is achieved through UCP-1, a protein uniquely found in the inner mitochondrial membrane of brown adipocytes that is able to uncouple proton transfer from ATP synthesis by generating heat [126]. Noradrenaline upregulates UCP-1 expression at the level of transcription via a cAMP response element (CRE), located upstream of the UCP-1 promoter [126, 251, 252]. UCP-1 activity can be upregulated by free fatty acids too, which are thought to bind to it, and enhance its activity in an “allosteric” fashion [253, 254]. Moreover, the activity of UCP-1 can be hampered by succinylation. Sirt5 preserves UCP-1’s function and its thermogenic capacity by removing the succinate [255]. In our study, we did not find any significant differences in the amount of UCP-1 in the BAT of control and mutant mice (**Figure 20**). Yet mutant mice tended to possess slightly lower amounts of UCP-1 than control mice. It is possible that this tendency may result from the lower noradrenaline levels in mutant mice. However, the biological impact of the slightly reduced UCP-1 levels in knockout mice cannot be estimated. At this stage, we cannot speculate of any direct linkage between UCP-1 regulation and cGKI, which could explain our phenotype. Free fatty acid and succinate abundance that could give a clue in our research were not determined and therefore, further experiments need to be conducted into this direction.

Other studies have shown that noradrenaline stimulates glucose transport into brown adipocytes by enhancing the functional activity of GLUT1 [256], and that is probably mediated via a β3 adrenoreceptors-cAMP-PKA-PI3K signalling pathway [257]. Therefore, the lower amounts of noradrenaline in BAT of our mutant mice could be an explanation for the impaired glucose uptake in the PET experiment (**Figure 17 B**).

In addition to catecholamines, thyroid hormones were also found to regulate BAT activity [144, 224, 258]. Indeed, brown adipocytes possess the enzyme called deiodinase type 2 (DIO2), necessary for the local conversion of thyroxine (T4) to triiodothyronine (T3) [259] and also for adaptive thermogenesis occurring in BAT [260]. In rodents, thyroid hormones upregulate UCP-1 expression by directly acting at the nuclear thyroid hormone receptors located in brown adipocytes [258]. In line with the above, clinical data demonstrated that BAT activity is enhanced in hyperthyroid patients compared to hypothyroid ones [142]. Besides the classical peripheral action of T3, more recent studies have shown that thyroid hormones can also act centrally within the hypothalamus, to regulate BAT thermogenesis. For instance, intracerebroventricular administration of T3 in mice, increased BAT thermogenesis via activation of the sympathetic nervous system [261], while systemic administration of T3 for 6 days led to browning of WAT [144]. Interestingly, in another study, thyroidectomised rats failed to initiate a thermogenic program after cold exposure to 4 °C [262]. Having explained the significance of the thyroid gland in thermogenesis, it would be interesting to examine the levels of thyroid hormones as well as the function of the thyroid gland in our mutant mice to shed more light in its role in thermogenesis in our paradigm.

D.4 FRET-based cGMP measurements in primary cell cultures and tissue slices

Another part of our project analysed cGMP generation in primary cell cultures prepared from BAT or adrenal gland tissues. To our knowledge, this is the first time that primary BAT- and adrenal gland-derived cells were subjected to FRET-based cGMP measurements using the cGi500 biosensor (**Figure 8**). For these studies, the biosensor was expressed either globally, where all cells expressed the biosensor, or under the action of a cell-specific Cre which allows for sensor expression in certain cells.

Primary cell cultures from whole organs are heterogeneous, as cells, in that case, may originate from different structures of the organ. Concerning BAT, our previous studies have demonstrated cGKI expression in at least three types of cells that are therefore highly likely to possess an active cGMP signalling system. Nevertheless, our culture conditions (see section **B.2.4**), are unlikely to favour the growth of nerve cells, as they lack substantial necessary nerve growth factors [263, 264]. Brown adipocytes are also unlikely to grow under these conditions, as they require specific growth factors too (insulin, T3). Due to that reason, it is highly possible that the cell populations growing on our coverslips arose either from the cGKI-positive, conical cells or from the VSMCs, which are known to grow well under these specific culture conditions. For these experiments, no serum starvation was performed prior to the measurement on day 7. Serum starvation has been extensively performed in our lab for VSMCs cultures in order to promote their contractile phenotype [265-267], but in our case, any deliberate phenotypic modulation of our cells was tried to be avoided. We wanted to capture and analyse the cGKI-positive cells in the closest possible state, as in the native tissue. Hence, the culture medium was merely changed once, 3 to 4 days post-seeding, for nutrient replenishment and removal of dead cells, cell debris, and toxic metabolites.

Since the discovery of the ANP receptor in rat brown adipocytes [268], other studies have demonstrated the existence of all three natriuretic peptide receptor genes (NPR1, NPR2, NPR3) in squirrel BAT at levels similar to the beta-adrenergic receptor genes [269]. Further studies have demonstrated a lipolytic role for natriuretic peptides in humans, through a cGMP dependent pathway [270].

In our study, we used the whole BAT from a Npr2$^{LacZ/+}$ x R26-cGi500$^{+/L1}$ mouse. This mouse represented the “wild type” situation, as BAT cells bore only one mutated Npr2 allele, and thus the function of the CNP/Npr2 signalling pathway was intact due to the presence of the second allele. The functionality of the Npr2 null receptor had been compromised by the presence of β-galactosidase gene (LacZ) in exon 1 [189]. Similarly, the Rosa26 locus bore one cGi500 (L1) biosensor transgene. We measured cells with an approximate confluency of 80% under continuous superfusion with imaging buffer, which was supplemented with 10 mM D-glucose. “Wild type” BAT cells demonstrated a marked preference for CNP, along with a weak response to ANP (**Figure 21 A**). 14% of the cells demonstrated a DEA/NO-induced cGMP elevation additionally to the other two cGMP-elevating drugs. It is difficult to distinguish whether these cells originated from the blood vessel VSMCs, or the cGKI-positive, conical cells in BAT. Under culture conditions, VSMCs tend to upregulate Npr2 expression, and that could explain the marked preference for CNP (Moritz Lehners, personal communication). Subsequent probing with an antibody against αSMA revealed a generalised, extensive staining of BAT primary cells with slightly different intensities across them (data not shown). Preliminary data from our lab indicate that healthy, “contractile” VSMCs possess higher amounts of contractile proteins (e.g. αSMA) and have a “preference” to ANP over CNP (data not shown). On the other hand, the ”synthetic” VSMC phenotype, which contributes to the development of atherosclerosis [265-267], responds preferably to stimulation with CNP and possesses lower levels of contractile protein (data not shown) (for an extensive review on the topic, see [187]). For these reasons, we speculate that our culture conditions have favoured the expansion of the blood vessel VSMC population and promoted the shift towards their synthetic phenotype. Surprisingly, although most of the BAT-derived primary cells showed CNP-induced cGMP signals, X-gal staining (indicative of Npr2-expressing cells) of the cell-containing coverslips, yielded no blue-stained cells (data not shown). The failure to detect LacZ expression might constitute a technical issue resulting for instance from an extended fixation time which had inactivated β-galactosidase. In that case, to overcome the overfixation obstacle one could visualise β-galactosidase with an anti-β-galactosidase antibody. Another plausible explanation would be the relatively high detection limit of the LacZ/X-Gal staining as compared to the highly sensitive FRET/cGMP imaging. This means that many cells express the Npr2 in amounts that are sufficient to elicit a biological response (cGMP increase upon CNP application), but the expression levels of the LacZ reporter gene is apparently too low to allow for a positive X-Gal staining of these cells. Moreover, our culture conditions certainly supported the survival and growth of the stromal-vascular-fraction cells of BAT, which contained pre-adipocytes (but not mature brown adipocytes), fibroblasts, VSMCs, and other mural cells.

We also tested the cGMP response pattern of Npr2-null BAT cells. Among other functions, the Npr2 receptor has been proven essential for proper axon bifurcation of the dorsal root ganglion (DRG) neurons within the spinal cord [271], cranial sensory neurons [189], and neurons of the auditory system [272, 273]. As expected, BAT cells originating from an Npr2$^{LacZ/LacZ}$ x R26-cGi500$^{L1/L1}$ culture (which genetically lacks Npr2), showed no response to CNP. Instead, nearly all of them demonstrated a DEA/NO-induced cGMP elevation, except one cell, which also demonstrated an additional ANP-induced cGMP elevation (**Figure 21 B**). In summary, wild type BAT cells preferred CNP, while cells from an Npr-null BAT showed preference for DEA/NO. These are, however, preliminary results and need to be replicated several times before a safe statement can be drawn.

Next, we examined the cGMP-response pattern of BAT-cultured cells marked by Nes-Cre, as these cells might be important for the observed freezing phenotype of the cGKI-brain KO mice. BAT-derived, Nes-Cre-positive cells exhibited a variable cGMP response pattern to DEA/NO, ANP and CNP (**Figure 22**). By looking at the pie chart (**Figure 23**), it becomes apparent that the majority of the cells (64%) responded to CNP, either with or without a DEA/NO and ANP response. Interestingly, 16% of the cells were able to generate cGMP solely after addition of DEA/NO, while another 5% of the total cells were weakly responsive to ANP along with DEA/NO (**Figure 23**). We postulate that these variable response patterns may well have emerged from the heterogeneity of the cell types that Nes-Cre highlights (the VSMCs of the arterioles, and the cGKI-positive, conical cells, see **D.1**). Because Nes-Cre recombination is present in VSMCs of the BAT arterioles, a large fraction of the sensor-expressing VSMCs in our cell cultures may have arisen from these recombined cells that have expanded clonally, thus generating islets of cGi500-positive cells. These VSMCs may have been the ones showing CNP preference in our experiments. However, we believe that the cells in our BAT cultures that only responded to DEA/NO are of particular relevance regarding the in vivo situation in BAT. Indeed, cGMP imaging in acute BAT vibratome sections from mice of the same genotype (Nes-Cre$^{tg/+}$ x R26-mT/cGi500$^{+/L2}$) highlighted that the conical, Nes-Cre-positive cells of BAT strongly responded to DEA/NO, while ANP and CNP failed to induce a clear cGMP elevation in these cells (**Figure 25**). Given the fact that real-time cGMP measurements in vibratome sections were particularly challenging due to the tissue movements that drove the setup out of focus, the failure to detect ANP- or CNP-induced cGMP transients could have been also attributed to technical issues. However, in 5 independent experiments, we were unable to obtain evidence that the conical, Nes-Cre-positive cells responded to ANP or CNP. Furthermore, a potential inability of the cytosolic cGi500 sensor to detect the membrane-associated cGMP pools (generated in response to NPs) is implausible. The cytosolic cGi500 sensor has been successfully used to detect ANP- and CNP-induced cGMP signals in various other cell types including smooth muscle cells [274] and dorsal root ganglion neurons [275].

It is worth stressing here that FRET-based cGMP-imaging on vibratome sections (as opposed to FRET-based cGMP-imaging on primary cell cultures) pose a great deal of scientific significance. In primary cell cultures, the cell type of interest can be usually found intermingled with other cell populations, thereby making its study extremely challenging. Moreover, primary cells usually undergo phenotypic modulations under cell culture conditions, which could sometimes alter scientific results. Vibratome tissue-sections, on the contrary, represent the “close-to-native” situation, where cells are more likely to reflect their physiological response to scientific treatments.

D.5 cGKI-positive, conical cells in BAT and adrenal gland express markers for pericytes

To identify the cell type of the abundantly-occurring cGKI-positive, conical cells observed in BAT and the adrenal gland cortex, scattered between the brown adipocytes and CORT-producing cells, respectively, we used immunofluorescent co-staining with antibodies. An antibody against αSMA showed a positive signal in a blood vessel found in BAT (**Figure 26 A**), which colocalised with cGKI (**Figure 26 C**). However, the conical, cGKI-positive cells around the blood vessel and between the brown adipocytes were negative for αSMA (**Figure 26 C**). The cGKI-positive nerve bundles in BAT were nicely stained by the neuronal markers 3A10 and RMO, yet these did not costained the cGKI-positive, conical cells (**Figure 26 F**, **L**). The endothelial cell marker CD31 revealed the dense network of the BAT microvasculature, however, there was again no double stain with cGKI (**Figure 26 I**).

In our FRET experiments on vibratome sections, Nes-Cre-positive cells demonstrated robust cGMP signals upon stimulation with DEA/NO (**Figure 25**). With the use of an antibody against the NO-GC (kindly provided by Prof. Andreas Friebe, Würzburg, Germany), we showed that cGKI colocalised with NO-GC in the vessels and conical cells of BAT (**Figure 27**). Moreover, the conical cells also expressed the pericyte marker PDGFRβ. PDGFRβ was confined to the periphery of these cells, as PDGFRβ is a membrane receptor, while cGKI was evenly present at the cytosol. Thus, based on their marker expression, we propose that cGKI-positive, conical cells in BAT, that also co-express NO-GC, represent pericytes (**Figure 27**). Similarly, PDGFRβ-positive cells in the adrenal cortex, expressed both NO-GC and cGKI, classifying them also as pericytes (**Figure 28**). It is important to note that adrenal cortex pericytes did not express Nes-Cre and may, therefore, comprise a different subpopulation of pericytes.

Pericytes constitute mural cells present at intervals along the walls of capillaries, precapillary arterioles, postcapillary venules, and collecting venules, in close proximity to endothelial cells, as stated by Dore-Duffy and Cleary (**Figure 30**) [276]. In the present work, we postulate that the pericytes found in BAT and the adrenal cortex most likely represent capillary pericytes. In regard to our BAT pericytes, these resembled the middle pericyte shown in figure 30 below.

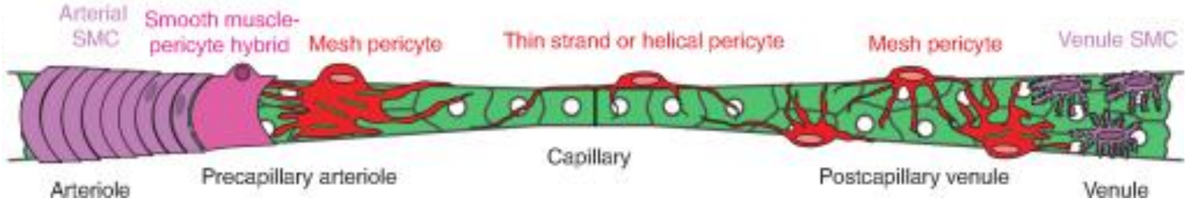

Figure 30. Pericyte population diversity in the vasculature of the brain.

Depiction of the mural cell types along the cerebral vasculature. Smooth muscle cells form concentric rings on arterioles. Hybrid smooth muscle-pericyte cells reside on precapillary arterioles and interlock with mesh pericytes at the arteriole–capillary interface, which occurs as penetrating arterioles ramify into the capillary bed. Pericytes in capillary beds typically exhibit long processes that traverse the microvasculature in single strands or pairs that twist in a helical fashion. Mesh pericytes become more prevalent again as capillaries turn into postcapillary venules. Stellate-shaped smooth muscle cells cover the walls of parenchymal venules. (Taken from [277]).

Pericytes play important roles in vascular biology as they participate in blood vessel formation, blood-brain barrier formation and maintenance [278, 279], and the control of blood flow [280, 281]. Especially the latter function has been the matter of debate in recent years. Hall and colleagues demonstrated that capillary pericytes in the brain can actively relax to dilate capillaries following neuronal activity (a process known as neurovascular coupling) and that this process requires the release of PGE_2 in presence of NO in order to relax pericytes [282]. In contrast, Hill and colleagues showed that capillary pericytes in the brain do not have the capacity to regulate blood flow, as they lack αSMA, and as a result, they are unable to relax in response to dilatory neuronal signals [283]. Instead, they proposed an alternative role for pericytes; that being the supply of a network for sensing, transmitting, or coordinating information between the neural and vascular compartments due to their long thin processes [283]. Consistent with the work of Hill *et al.*, our BAT cryosection stainings never demonstrated expression of αSMA in pericytes of that tissue (**Figure 26 A**). Whether that could be a fact or a technical issue still remains unclear, yet larger vessels within BAT were clearly stained positive for αSMA (**Figure 26 A**). So far, several markers have been used to identify pericytes. The most common of them include αSMA, desmin, NG2, PDGFRβ, aminopeptidase A and N, and CD146 [281]. However, none of these markers is absolutely specific for pericytes, and none of them can be used to identify all pericytes. Pericyte marker expression is dynamic and varies between organs and developmental stages, a reason that often causes difficulties with the identification and understanding of the ontogeny of pericytes (for excellent publications see: [284-286]. αSMA, for instance, is not appreciably expressed by skin or CNS pericytes under normal circumstances but becomes upregulated during retinopathy and in subcutaneously transplanted tumours [285]. Also, αSMA can be found in brain pericytes of the chicken embryo, but it is not expressed in brain pericytes of the mouse, as explained in a comprehensive review by Armulik *et al.* [284]. Indeed, several researchers have focused their attention on elucidating the expression of αSMA in pericytes. Nehls *et al.*, for instance, studied the expression of this marker in bovine retinae and rat mesentery pericytes using immunocytochemical methods. They came to the conclusion that pericytes around “true capillaries” (midcapillaries) did not contain αSMA, whereas pre- and postcapillary, as well as venule pericytes, displayed αSMA expression [287]. Moreover, other authors have described similar findings [205, 276, 281]. Dore-Duffy *et al.*, for example, specifically mentions that “in their capillary location, most pericytes are αSMA negative”, while the expression of this protein can be induced within the capillary “on-demand” and may be related to the role of the pericyte in focal regulation of capillary blood flow [276]. According to Yamazaki and colleagues, capillary pericytes do not express αSMA, but only NG2 and PDGFRβ, while capillary pericytes found in tumour vessels do express αSMA [205]. Furthermore, in primary cultures, freshly isolated pericytes from capillaries showed less than 5% expression of αSMA, but nearly 100% expression of this marker by day 7, implying that pericytes in primary cell cultures undergo a period of quiescence, that is followed by the development of the αSMA phenotype [276].

Another research group analysed pericytes harvested from the skeletal muscle and classified them into two subgroups based on their marker expression and their differentiation potential. Both type-1 (Nestin$^-$/ NG2$^+$/ CD146$^+$) and type-2 pericytes (Nestin$^+$/ NG2$^+$/ CD146$^+$) could give rise to αSMA-positive pericytes under culture conditions, while only type-2 pericytes were capable of forming βIII-tubulin-positive cells [288]. Based on the expression of Nestin, it could be possible that our adrenal gland and BAT pericytes represent type-1 and type-2 pericytes, respectively. Yet, regarding the expression of NG2 [289], our BAT pericytes seemed not to express this marker contrary to what other researchers usually described (data not shown). Control experiments of NG2 staining in wild type cerebellum yielded a positive result (data not shown), and these resembled the results obtained by Cuervo *et al.* [204]. Hence, it still remains to be clarified whether the failure to detect NG2 in our BAT pericytes was a technical issue or merely our BAT pericytes belong to a non-NG2-expressing subpopulation.

Pericytes are implicated in tumour biology, and in expansion and dissemination of the tumour cells around the body, as claimed by recent research. According to Birbrair *et al.*, pericytes are essential during tumour neovascularisation, i.e for the stabilisation of new blood vessels, due to their angiogenic potential. In that context, potential anti-pericyte agents could be used in the future in combination with common anti-cancer drugs. Such a regime could facilitate tumour shrinkage by eliminating pericytes at the tumour-microenvironment, a fact that would severely impair the blood supply of the tumour [290].

Due to their high plasticity, it has often been advocated that pericytes can give rise to a plethora of cells, including osteoblasts [291], chondrocytes [292], and muscle fibres [293]. Interestingly, research has shown that type-1 pericytes (Nestin$^-$/ NG2$^+$/ CD146$^+$) can give rise to adipocytes and contribute to fat accumulation [294-297], and vice versa, adipocytes can give rise to pericytes [298]. However, very little is known about the in vivo role of pericytes in the brown adipose tissue biology.

Based on our FRET and immunostaining data, PDGFRβ-positive pericytes in BAT possessed a functional NO/NO-GC/cGMP/cGKI signalling pathway, a finding that is in accordance with other work [299]. The role of NO-GC for proper BAT function and thermogenesis, as well as for protection against diet-induced obesity has been already postulated [145]. Because we were unable to detect any NO-GC or cGKI expression directly in brown adipocytes (**Figure 27**), we propose that the effects of NO/NO-GC and cGKI on BAT [145, 148] may be exerted in an indirect way, for instance via pericytes acting on brown adipocytes by modulating crucial signalling pathways. Also, because our BAT pericytes did not contain αSMA, it is rather implausible that they modulate thermogenesis in BAT, by regulating blood flow/nutrient supply. Nevertheless, an indirect regulation of blood flow via pericytes can not be excluded. We consider that the role of cGKI in the nervous system (hypothalamus, BAT nerves) may be perhaps much more important for the "freezing" phenotype of our cGKI-brain KO mice. For that reason, additional research in that direction has to be conducted.

Last but not least, PDGFRβ-, cGKI-positive pericytes scattered throughout the adrenal cortex might well be able to locally influence blood flow and thus affect ACTH availability to CORT-producing cells, or even restrain CORT secretion to the bloodstream. Moreover, the notion that pericytes might influence CORT levels by a temporal secretion of paracrine factors cannot be overseen. Indeed, during the last years, several studies have emerged, suggesting that additional factors can modulate adrenal CORT release independently of ACTH. For example, neuropeptides, growth factors and cytokines have been proposed to act as intra-adrenal paracrine factors regulating CORT release [300].

D.6 Summary and Outlook

The role of the cGMP signalling pathway in the cardiovascular system is well established, though, its function in thermogenesis in mice remains largely unclear. In the present project, we sought to decipher the involvement of cGMP signalling in cold-stress-induced thermogenesis by using conditional mouse mutants that were lacking cGKI in the nervous system and all Nestin$^+$ cells, and their progeny (cGKI-brain KO mice).

After confirming the expression of cGKI in organs of thermogenesis, namely the hypothalamus and BAT, we subjected cGKI-brain KO mice to a cold-stress ordeal and measured their body temperature, noradrenaline content in BAT, thermogenesis-related proteins (TH, UCP-1), as well as BAT activity with PET via uptake of [^{18}F]FDG. Subsequently, we performed FRET-based cGMP measurements in live cells, and numerous BAT-analyses by means of immunostaining to characterise conical, cGKI-positive cells in BAT.

Based on our data, we conclude, that cGKI-brain KO mice exhibit a body temperature regulation deficit under cold-stress. We have demonstrated, that cGKI-brain KO mice compared to control mice, were unable to maintain their body temperature after 6 h in a cold room at 4 °C. After cold-stress, the BAT noradrenaline content was not significantly different compared to control mice, although there was a tendency towards lower levels of noradrenaline in BAT of mutant mice. Under basal conditions, mutant mice possessed significantly lower amounts of noradrenaline in their BAT in comparison to control mice. We also analysed the levels of UCP-1 and TH in BAT of unstressed and cold-stressed mice. Albeit there was no significant difference as far as these two proteins are concerned between the two genotypes both under normal and stressed condition, cGKI-brain KO mice tended to exhibit lower amounts of UCP-1 and TH. Furthermore, our PET analyses of cold-stressed mice revealed an impairment in BAT activity. Indeed, the BAT of cGKI-brain KO mice took up significantly lower amounts of radio-labelled glucose ([^{18}F]FDG), when compared to the control group.

Next, we have performed FRET-based cGMP measurements in acute whole-BAT slices and BAT-derived primary cell cultures. Cell cultures exhibited a complex cGMP-response pattern. The majority of cultured cells derived from BAT were able to generate cGMP upon stimulation with CNP. A small percentage of cells (~16%), however, responded only to the NO donor DEA/NO. This was an exciting finding as FRET-based cGMP measurements on BAT vibratome slices demonstrated that cGKI-positive, Nes-Cre-positive cells in BAT were strongly responding to DEA/NO by generating cGMP.

In the last part of this work, we employed immunostaining techniques to characterise the type of the conical, cGKI-positive cells in BAT and the adrenal gland. While we never detected cGKI in brown adipocytes themselves, strong cGKI expression was observed in three other structures of BAT: the nerve bundles, VSMCs of the blood vessels, and in conical cells with fine, long processes that were in close proximity to the capillaries. The cGKI-positive, conical cells also co-expressed NO-GC, and based on their expression of the pericyte marker PDGFRβ, we identified them as pericytes. This is the first time to our knowledge that pericytes have been identified in BAT.

In sum, we showed here that genetic ablation of cGKI in the central and peripheral nervous system, as well as in Nestin-expressing cells, impaired stressed-induced thermogenesis in mice (**Figure 31**). Based on our data, we suggest that cGKI probably exerts its effects on thermogenesis in mice in an indirect way, since we were unable to detect cGKI in brown adipocytes themselves. We, therefore, propose that ablation of cGKI in pericytes of BAT may affect thermogenesis possibly by influencing necessary signalling cues to brown adipocytes, or indirectly by somehow influencing blood flow or nutrients to this tissue.

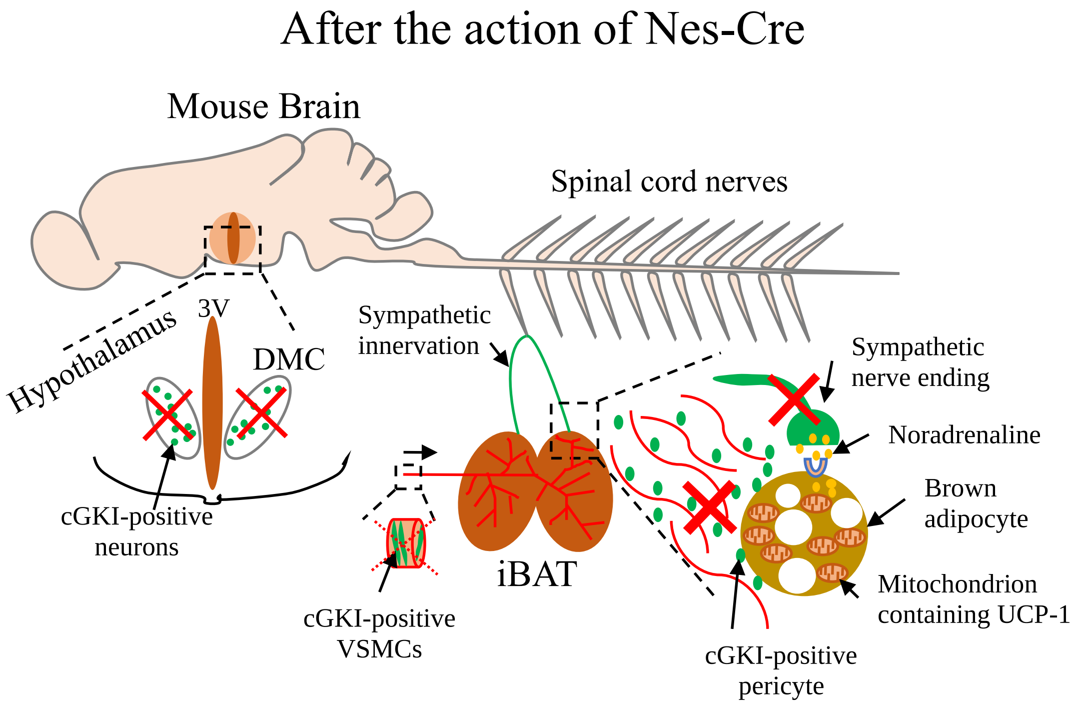

Figure 31. Graphical summary of this work.

Expression of cGKI (green) was detected in several structures involved in thermogenesis. The kinase was present in the compact part of the dorsomedial hypothalamus (DMC) as well as in sympathetic nerve bundles innervating iBAT. cGKI-brain KO animals, that were generated with the use of a Nes-Cre line, lacked cGKI in these structures (indicated by the red X). Within BAT, conical pericytes and the VSMCs of blood vessels also exhibited expression of cGKI. Nes-Cre-mediated ablation of cGKI was efficient in pericytes and less efficient in VSMCs (red arrow and dotted red arrow, respectively). cGKI-brain KO mice demonstrated an impairment of body temperature regulation under cold stress, most likely due to decreased BAT activity. Further analyses are required to elucidate the exact cellular and molecular mechanisms behind cGKI's role in thermogenesis. [DMC, dorsomedial hypothalamus, compact part; 3V, third ventricle; iBAT, interscapular BAT].

Despite our efforts, it was impossible to cover every aspect of this complex project within the given time. Today, BAT's significance in combating obesity and related comorbidities such as diabetes, heart disease, or the metabolic syndrome is very well appreciated. For that reason, a plethora of additional experiments still need to be carried out to fully comprehend the role of cGKI in BAT-related thermogenesis. For instance, since Nes-Cre and cGKI are both abundantly expressed in brain regions important for regulation of temperature [57, 188], it cannot be excluded that the impaired thermoregulation of cGKI-brain KO mice arises from neuronal tissues located upstream of BAT. Or from a combination of neuronal and non-neuronal, but still Nestin-expressing, cells/tissues. Hence, careful scrutiny of the hypothalamic areas responsible for thermoregulation with parallel high resolution-assessment for cGKI and Nestin expression are advisable. Because macrophages have been reported to modulate noradrenaline content in BAT [301], determination of the number of macrophages in both animal groups should be performed via FACS analyses. It would be also interesting to investigate the PDEs responsible for cGMP degradation in BAT pericytes via FRET-based, spinning-disk, confocal microscopy on acute vibratome slices, in the presence and absence of specific PDE inhibitors. If possible, FRET-based cGMP measurements on BAT nerve bundles of a Nes-Cre$^{tg/+}$ x R26-mT/cGi500$^{+/L2}$ mouse should also be performed via spinning-disk, confocal microscopy. Last but not least, since we propose that BAT pericytes may account for the temperature dysregulation of cGKI-brain KO mice, it would be extremely interesting to examine, whether cGKI ablation in these pericytes, for instance, via the act of a PDGFRβ-Cre mouse line, also results in the "freezing" phenotype. Alternatively, it would be also intriguing to see whether re-establishing cGKI in PDGFRβ-expressing cells of BAT, could restore the observed "freezing" phenotype.

E. Appendix

E.1 Chemicals, equipment and consumables

Reagent name, supplying company and accession numbers are given in alphabetical order. Substances not listed here were purchased from Roth.

E.1.1 Reagents and chemicals

Name	Supplier	Order Number
Agarose LE	Biozym	#840001
3,3’-Diaminobenzidine (DAB)	Sigma-Aldrich	D8001
DMEM GlutaMAX™	Gibco®/Life Technologies™	#10566-032
1 Kb DNA ladder	Invitrogen/Life Technologies™	#15615016
FCS, heat-inactivated	Gibco®/Life Technologies™	#10500-064
Hoechst 33258	Sigma-Aldrich	#861405
Na-L-Glutamate Monohydrate	Merck	#1.06445.1000
Normal Goat Serum	Dianova	#011-000-001
Normal Donkey Serum	Sigma-Aldrich	O0625
PageRuler™ Prestained Protein Ladder	Fermentas/Thermo Scientific™	#26616
Penicillin-Streptomycin, liquid	Gibco®/Life Technologies™	#15140-122
Midori Green Advance	Nippon Genetics	#MG04
Tris	Sigma-Aldrich	
Trypan Blue Stain	Gibco®/Life Technologies™	#15250061
10x Reaction buffer S	Bioron	

E.1.2 Enzymes

Name of Enzyme	Supplier	Order Number
Collagenase	Sigma-Aldrich	#C7926
Papain	Sigma-Aldrich	P5762
Hyaluronidase	Sigma-Aldrich	9001-54-1
Proteinase K	GENAXXON bioscience	#7528.1

E.1.3 Commercially available kits

Name of Kit	Supplier	Order Number
ECL Advance Western Blotting Detection Kit	GE Healthcare	#RPN2135
Total Protein Kit, Micro Lowry, Peterson's Modification	Sigma-Aldrich	#TP0300
Vectastain® Elite® ABC Kit	Vectorlabs	#PK6100
Norepinephrine ELISA kit Any Sample	ImmuSmol	#BA-E-5200

E.2 Equipment and devices

Name	Supplier	Modell
Autoclave	SANOclav	La-Va
Balance	Sartorius	Excellence
	Mettler	AM50
Binocular light	Schott	KL 1500 LCD
Camera	Allied Vision Technologies GmbH	Marlin F-046C
	Cybertech	CS1
	SONY	Cyber-shot VX DSC-W17

QuantEM,	512SC	Photometrics
Centrifuge	Eppendorf	Centrifuge 5804R (A-4-44)
	Eppendorf	Centrifuge 5417C(F35-40-11)
Clean bench	Thermo Scientific	HERA safe
Cryostat	MicromInternational	HM525
Digital imaging system	Biozym Scientific GmbH	FluorChem® FC3
Fluorescence microscope	ZEISS	Axioskop 20
Freezer (−20 °C)	Liebherr	Premium No Frost
Freezer (−80 °C)	Revco Technologies	ULT2186-3-V35
Fridge-Freezer	Liebherr	Comfort No Frost
SDS Gel preparing system	Bio-Rad	Mini-Protean® 3
Heating block	Eppendorf	Thermomixer compact
Homogeniser	MP Biomedicals	Fast Prep®-24
Incubator	New Brunswick Scientific	Innova® CO-170
Light microscope	ZEISS	Axiovert 40C
Manual cell counter	Neolab	
Microplate photometer	Thermo Scientific	Multiskan™ EX
Microtome	MicromInternational	HM335E
Power supply	Biometra	Standard Power Pack P25
	Bio-Rad	200/2.0 Power Supply

Shaker	Biometra	WT12
Stereoscopic microscope	ZEISS	Stemi 2000-CS
Thermocycler	Peqlab	Primus 96 advanced
	Peqlab	peqSTAR 2X
UV-Transilluminator	Vilber-Lourmat	TFX-20M
Vibratome	Leica	VT1200
Vortex-Mixer	Neolab	Vortex Mixer
Water bath	Memmert	
	Medax	
Western blotting device	Roth	MAXI-Semi-Dry-Blotter

All consumables (pipette tips, cell culture flasks, reaction tubes, falcons) used in this project were purchased from one of the following companies: Corning, Sarstedt and Roth.

E.3 Supplementary tables

Table 1. Conditions for genotyping PCRs.

Mouse line	Primer	Cycles	T_d, time	T_a, time	T_e, time	Product size
cGKI$^{L1/L2}$	RF53 0.3 µl RF118 0.3 µl RF125 0.3 µl	35	95°C, 10 sec	50°C, 30 sec	72°C, 30 sec	L2: 338 bp + : 284bp L1: 250 bp
Nes-Cre	Cre800 0.3 µl Cre1200 0.3µl	35	95°C, 10 sec	58°C, 30 sec	72°C, 30 sec	tg: 402 bp + : none
R26-mT/cGi500	BB01 0.3 µl BB02 0.3 µl BB03 0.3 µl	35	95°C, 10 sec	61°C, 30 sec	72°C, 30 sec	L2: 250 bp + : 330 bp
Npr2-LacZ	P1 0.3 µl P2 0.3 µl P3 0.3 µl	35	95°C, 10 sec	65°C, 30 sec	72°C, 30 sec	LacZ : 398 bp + : 348 bp
R26-Ai14	BB33 0.3 µl BB34 0.3 µl BB35 0.3µl BB36 0.3 µl	35	94°C, 10 sec	65°C, 30 sec	72°C, 30 sec	L2 : 196 bp + : 297 bp

All PCR programmes possess an initial denaturation step (at 95 °C for 5 min, for R26-Ai14: 94 °C for 2 min) and a final elongation step (at 72 °C for 5 min).

Table 2. Primer sequences for genotyping PCRs.

Primer name	Sequence 5' → 3'	Usage
BB01	CTCTGCTGCCTCCTGGCTTCT	Genotyping PCR, R26 common fwd
BB02	CGAGGCGGATCACAAGCAATA	Genotyping PCR, R26 wt rev
BB03	TCAATGGGCGGGGGTCGTT	Genotyping PCR, R26-mT/cGi500 rev
BB33	AAGGGAGCTGCAGTGGAGTA	Genotyping PCR, Ai14 wt fwd
BB34	CCDAAAATCTGTGGGAAGTC	Genotyping PCR, Ai14 wt rev
BB35	GGCATTAAAGCAGCGTATCC	Genotyping PCR, Ai14 ko rev
BB36	CTGTTCCTGTACGGCATGG	Genotyping PCR, Ai14 ko fwd
RF53	CCTGGCTGTGATTTCACTCCA	Genotyping PCR, cGKI fwd
RF118	AAATTATAACTTGTCAAATTCTTG	Genotyping PCR, cGKI rev
RF125	GTCAAGTGACCACTATG	Genotyping PCR, cGKI rev
Cre800	GCTGCCACGACCAAGTGACAGCAATG	Genotyping PCR, Cre fwd
Cre1200	GTAGTTATTCGGATCATCAGCTACAC	Genotyping PCR, Cre rev
P1	TGCCACCCTATCCTTAGTCC	Genotyping PCR, wt fwd
P2	GTGTTCTGGCAGCACCAC	Genotyping PCR, wt rev
P3	TCGCTATTACGCCAGCTG	Genotyping PCR, Npr2LacZ rev

Table 3. List of primary antibodies

Antibody	Species (mono-/polyclonal)	Application, dilution	Order details
cGKIc (DH)	rabbit (p)	IF, IHC: 1:1000 WB: 1:5000	Ref. [203]
cGKIα	guinea pig (p)	IF: 1:2000	Ref. [189]
βIII-tubulin	mouse (m)	IF: 1:500	#G7121, Promega
αSMA	mouse (m)	IF: 1:800	#A2547, Sigma
PDGFRβ	goat (p)	IF: 1:100	#AF1042, R&D Systems
NO-GC	rabbit (p)	IF: 1:800	Donation Prof. Andreas Friebe
CD31	rat (m)	IF: 1:50	#550274, BD Biosciences
RMO (neurofilament-M)	mouse (m)	IF: 1:500	#2338, Cell Signaling
GLUT4	goat (p)	WB: 1:250	#SC 1608, Santa Cruz
TH	sheep (p)	IF: 1:1000 WB: 1:1000	NB 300-110 Novus Biologicals
UCP-1	rabbit (m)	WB: 1:1000	#14670, Cell Signaling
GAPDH	rabbit	WB: 1:5000	#2118, Cell Signaling
3A10	mouse (m)	IF: 1:1000	#NBP2-37548, Novus Biologicals

Table 4. List of secondary antibodies

Antibody	Species	Application, dilution	Order details
anti-rabbit biotinylated	goat	IHC: 1:500	BA-1000, Vector Laboratories
anti-mouse biotinylated	horse	IHC	BA-2000, Vector Laboratories
anti-rabbit HRP	goat	WB: 1:5000	#7074S, Cell Signaling
anti-rabbit Alexa 488	goat	IF: 1:500	#A11008, Invitrogen
anti-rabbit Alexa 594	goat	IF: 1:500	#A11012, Invitrogen
anti-rabbit Alexa 555	goat	IF: 1:500	#A21428, Invitrogen
anti-mouse Alexa 555	goat	IF: 1:500	#A21424, Invitrogen
anti-rat Alexa 594	rabbit	IF: 1:500	#A21211, Invitrogen
anti-rat Alexa 488	goat	IF: 1:500	#A11006, Invitrogen
anti-guinea pig Alexa 488	goat	IF: 1:500- 1:1000	#106545003, Dianova
anti-goat Alexa 594	donkey	IF: 1:500	#A11058, Invitrogen
anti-goat Alexa 647	donkey	IF: 1:500	#A21447, Invitrogen
Anti-sheep Alexa 488	donkey	IF: 1:500	#A11015, Invitrogen

Table 5. Composition of SDS-PAGE gels.

Quantities suffice for 2 gels of 0.75 mm thickness. Add TEMED and APS at last, otherwise, the gel will initiate to polymerise.

Reagent	Stacking gel	Resolving gel	
Pipette in that order:	4%	8%	12%
Rotiphorese® Gel 30 (*Roth*) (30% acrylamide/ bisacrylamide, ratio 37.5:1)	650 µl	2.7 ml	4 ml
4x Tris-SDS, pH 8.8, stored 4 °C	–	2.5 ml	2.5 ml
4x Tris-SDS, pH 6.8, stored 4 °C	1.25 ml	–	–
ddH$_2$0	3.05 ml	4.7 ml	3.4 ml
tetramethyl ethylenediamine (TEMED), stored at 4 °C	10 µl	10 µl	10 µl
20% ammonium persulfate (APS), stored at -20 °C	25 µl	50 µl	50 µl

E.4 Supplementary figures

E.4.1 Expression of cGKI in BAT revealed by immunohistochemistry on paraffin sections

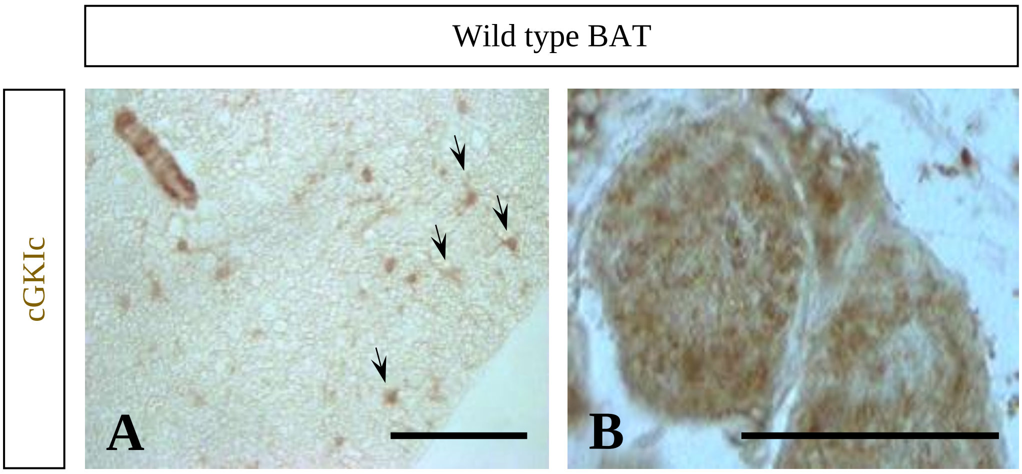

Figure S1. Immunohistochemistry images of wild type murine BAT, depicting cGKI expression.

10 µm-thick paraffin sections were stained overnight with the cGKI common antibody and visualised by the avidin-biotin method using the diaminobenzidine (DAB) substrate, as a chromogen. (A) cGKI was strongly expressed in the VSMCs of the vasculature, as seen in the upper left corner, and in small, conical cells with thin processes, evenly scattered within the tissue (arrows). Interestingly, no cGKI was observed in the brown adipocytes themselves. (B) A nerve bundle innervating BAT, which shows intense cGKI stain. Scale bars: 100 µm.

E.4.2 Western blot examination of GLUT-4 levels in BAT

Unstressed 48-60 week-old male mice

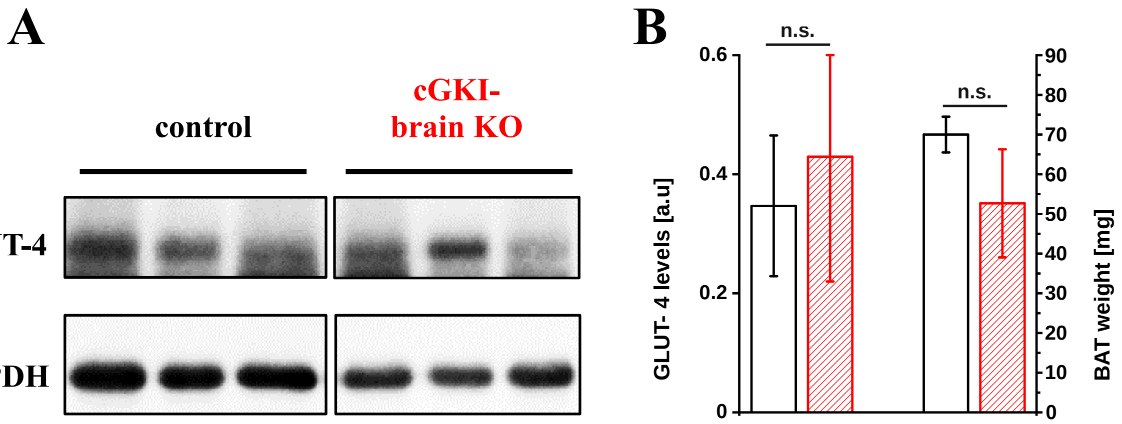

Figure S2. Western blot analysis of GLUT-4 levels in BAT of 48-60 week-old male mice.

To shed light on the possible reason that accounted for the reduced glucose uptake in our PET scan experiment, we examined the levels of GLUT-4 in BAT of 48-60 week-old unstressed, male mice (controls: n= 3, cGKI-brain KO: n= 3). (A) Image depicting Western blot analysis of GLUT-4 in whole-BAT of control and cGKI-brain KO animals. (B) Densitometric analysis GLUT-4 levels shown in Western blot in A. cGKI-brain KO animals exhibited non-significantly slightly elevated amounts of GLUT-4 compared to controls (0.43 ± 0.21 vs 0.35 ± 0.12 respectively). The whole-BAT weight of mutant animals did not differ from that of controls (52.67 ± 13.62 vs 70 ± 4.51, respectively). Data are presented as mean values ± SEM. Statistical significance was tested with a Student’s t-test. (Preliminary data).

F. References

1. Kemp-Harper, B. and R. Feil, *Meeting report: cGMP matters. Sci Signal*, 2008. **1**(9):pe12.
2. Feil, R. and B. Kemp-Harper, *cGMP signalling: from bench to bedside. Conference on cGMP generators, effectors and therapeutic implications. EMBO Rep*, 2006. **7**(2): p. 149-53.
3. Potter, L.R., et al., *Natriuretic peptides: their structures, receptors, physiologic functions and therapeutic applications. Handb Exp Pharmacol*, 2009. (191): p. 341-66.
4. Dumoulin, A., et al., *Molecular Analysis of Sensory Axon Branching Unraveled a cGMP-Dependent Signaling Cascade. Int J Mol Sci*, 2018. **19**(5): p. 1266.
5. Hofmann, F., et al., *Function of cGMP-dependent protein kinases as revealed by gene deletion. Physiol Rev*, 2006. **86**(1): p. 1-23.
6. Schmidtko, A., *Nitric oxide-mediated pain processing in the spinal cord. Handb Exp Pharmacol*, 2015. **227**: p. 103-117.
7. Schmidtko, A., I. Tegeder, and G. Geisslinger, *No NO, no pain? The role of nitric oxide and cGMP in spinal pain processing. Trends Neurosci*, 2009. **32**(6): p. 339-346.
8. Kots, A.Y., et al., *A short history of cGMP, guanylyl cyclases, and cGMP-dependent protein kinases. Handb Exp Pharmacol*, 2009(191): p. 1-14.
9. Smith, M., G.I. Drummond, and H.G. Khorana, *Cyclic Phosphates. IV.1 Ribonucleoside-3',5' Cyclic Phosphates. A General Method of Synthesis and Some Properties. J Am Chem Soc*, 1961. **83**(3): p. 698-706.
10. Ashman, D.F., et al., *Isolation of adenosine 3', 5'-monophosphate and guanosine 3', 5'-monophosphate from rat urine. Biochem Biophys Res Commun*, 1963. **11**: p. 330-4.
11. Kimura, H. and F. Murad, *Two forms of guanylate cyclase in mammalian tissues and possible mechanisms for their regulation. Metabolism*, 1975. **24**(3): p. 439-45.
12. Lucas, K.A., et al., *Guanylyl cyclases and signaling by cyclic GMP. Pharmacol Rev*, 2000. **52**(3): p. 375-414.
13. Pyriochou, A. and A. Papapetropoulos, *Soluble guanylyl cyclase: more secrets revealed. Cell Signal*, 2005. **17**(4): p. 407-413.
14. Russwurm, M. and D. Koesling, *NO activation of guanylyl cyclase. EMBO J*, 2004. **23**(22): p. 4443-4450.
15. Friebe, A. and D. Koesling, *The function of NO-sensitive guanylyl cyclase: what we can learn from genetic mouse models. Nitric Oxide*, 2009. **21**(3-4): p. 149-56.
16. Francis, S.H., et al., *cGMP-dependent protein kinases and cGMP phosphodiesterases in nitric oxide and cGMP action. Pharmacol Rev*, 2010. **62**(3): p. 525-563.
17. Koesling, D., E. Mergia, and M. Russwurm, *Physiological Functions of NO-Sensitive Guanylyl Cyclase Isoforms. Curr Med Chem*, 2016. **23**(24): p. 2653-2665.
18. Derbyshire, E.R. and M.A. Marletta, *Biochemistry of soluble guanylate cyclase. Handb Exp Pharmacol*, 2009(191): p. 17-31.
19. Lapp, H., et al., *Cinaciguat (BAY 58–2667) Improves Cardiopulmonary Hemodynamics in Patients With Acute Decompensated Heart Failure. Circulation*, 2009. **119**(21): p. 2781-2788.
20. Bredt, D.S. and S.H. Snyder, *Isolation of nitric oxide synthetase, a calmodulin-requiring enzyme. Proc Natl Acad Sci U S A*, 1990. **87**(2): p. 682-685.
21. Fleming, I., *Molecular mechanisms underlying the activation of eNOS. Pflugers Arch*, 2010. **459**(6): p. 793-806.
22. Forstermann, U., et al., *Nitric oxide synthase isozymes. Characterization, purification, molecular cloning, and functions. Hypertension*, 1994. **23**(6 Pt 2): p. 1121-31.
23. Förstermann, U. and W.C. Sessa, *Nitric oxide synthases: regulation and function. Eur Heart J*, 2012. **33**(7): p. 829-837d.
24. Stuehr, D., S. Pou, and G.M. Rosen, *Oxygen reduction by nitric-oxide synthases. J Biol Chem*, 2001. **276**(18): p. 14533-6.
25. Alderton, W.K., C.E. Cooper, and R.G. Knowles, *Nitric oxide synthases: structure, function and inhibition. Biochem J*, 2001. **357**(3): p. 593-615.
26. Kleppisch, T. and R. Feil, *cGMP signalling in the mammalian brain: role in synaptic plasticity and behaviour. Handb Exp Pharmacol*, 2009. **191**: p. 549-579.
27. Toda, N., K. Ayajiki, and T. Okamura, *Control of systemic and pulmonary blood pressure by nitric oxide formed through neuronal nitric oxide synthase. J Hypertens*, 2009. **27**(10): p. 1929-40.
28. Rajfer, J., et al., *Nitric oxide as a mediator of relaxation of the corpus cavernosum in response to nonadrenergic, noncholinergic neurotransmission. N Engl J Med*, 1992. **326**(2): p. 90-4.

29. Turko, I.V., et al., *Inhibition of cyclic GMP-binding cyclic GMP-specific phosphodiesterase (Type 5) by sildenafil and related compounds. Mol Pharmacol*, 1999. **56**(1): p. 124-30.
30. Rosen, R.C. and J.B. Kostis, *Overview of phosphodiesterase 5 inhibition in erectile dysfunction. Am J Cardiol*, 2003. **92**(9a): p. 9m-18m.
31. Shesely, E.G., et al., *Elevated blood pressures in mice lacking endothelial nitric oxide synthase. Proc Natl Acad Sci U S A*, 1996. **93**(23): p. 13176-81.
32. Knowles, R.G. and S. Moncada, *Nitric oxide synthases in mammals. Biochem J*, 1994. **298**(Pt 2): p. 249-258.
33. Rudic, R.D., et al., *Direct evidence for the importance of endothelium-derived nitric oxide in vascular remodeling. J Clin Invest*, 1998. **101**(4): p. 731-6.
34. Forstermann, U., *Oxidative stress in vascular disease: causes, defense mechanisms and potential therapies. Nat Clin Pract Cardiovasc Med*, 2008. **5**(6): p. 338-49.
35. Nathan, C.F. and J.B. Hibbs, Jr., *Role of nitric oxide synthesis in macrophage antimicrobial activity. Curr Opin Immunol*, 1991. **3**(1): p. 65-70.
36. Garthwaite, J., *Concepts of neural nitric oxide-mediated transmission. Eur J Neurosci*, 2008. **27**(11): p. 2783-2802.
37. Brown, G.C. and J.J. Neher, *Inflammatory neurodegeneration and mechanisms of microglial killing of neurons. Mol Neurobiol*, 2010. **41**(2-3): p. 242-7.
38. Kanwar, J.R., et al., *Recent advances on the roles of NO in cancer and chronic inflammatory disorders. Curr Med Chem*, 2009. **16**(19): p. 2373-94.
39. Potter, L.R., *Natriuretic peptide metabolism, clearance and degradation. FEBS J*, 2011. **278**(11): p. 1808-1817.
40. Potter, L.R., S. Abbey-Hosch, and D.M. Dickey, *Natriuretic peptides, their receptors, and cyclic guanosine monophosphate-dependent signaling functions. Endocr Rev*, 2006. **27**(1): p. 47-72.
41. Hisado-Oliva, A., et al., *Mutations in C-natriuretic peptide (NPPC): a novel cause of autosomal dominant short stature. Genet Med*, 2018. **20**(1): p. 91-97.
42. Waldman, S.A., R.M. Rapoport, and F. Murad, *Atrial natriuretic factor selectively activates particulate guanylate cyclase and elevates cyclic GMP in rat tissues. J Biol Chem*, 1984. **259**(23): p. 14332-14334.
43. Kuhn, M., *Molecular physiology of membrane guanylyl cyclase receptors. Physiol Rev*, 2016. **96**(2): p. 751-804.
44. Boudin, E., et al., *Bi-allelic Loss-of-Function Mutations in the NPR-C Receptor Result in Enhanced Growth and Connective Tissue Abnormalities. Am J Hum Genet*, 2018. **103**(2): p. 288-295.
45. Schmidt, H., et al., *C-type natriuretic peptide (CNP) is a bifurcation factor for sensory neurons. Proc Natl Acad Sci U S A*, 2009. **106**(39): p. 16847-16852.
46. Hofmann, F., *The biology of cyclic GMP-dependent protein kinases.* J Biol Chem, 2005. **280**(1): p. 1-4.
47. Pfeifer, A., et al., *Structure and function of cGMP-dependent protein kinases. Rev Physiol Biochem Pharmacol*, 1999. **135**: p. 105-149.
48. Vallur, R., H. Kalbacher, and R. Feil, *Catalytic Activity of cGMP-Dependent Protein Kinase Type I in Intact Cells Is Independent of N-Terminal Autophosphorylation. PLOS ONE*, 2014. **9**(6): p. e98946.
49. S H Francis, a. and J.D. Corbin, *Structure and Function of Cyclic Nucleotide-Dependent Protein Kinases. Annu Rev Physiol*, 1994. **56**(1): p. 237-272.
50. de Jonge, H.R. and O.M. Rosen, *Self-phosphorylation of cyclic guanosine 3':5'-monophosphate-dependent protein kinase from bovine lung. Effect of cyclic adenosine 3':5'-monophosphate, cyclic guanosine 3':5'-monophosphate and histone. J Biol Chem*, 1977. **252**(8): p. 2780-2783.
51. Lincoln, T.M., D.A. Flockhart, and J.D. Corbin, *Studies on the structure and mechanism of activation of the guanosine 3':5'-monophosphate-dependent protein kinase. J Biol Chem*, 1978. **253**(17): p. 6002-9.
52. Hofmann, F., et al., *cGMP Regulated Protein Kinases (cGK)*, in *cGMP: Generators, Effectors and Therapeutic Implications*. *Handb Exp Pharmacol*, 2009. p. 137-162.
53. Feil, R., et al., *Cyclic GMP-dependent protein kinases and the cardiovascular system: insights from genetically modified mice. Circ Res*, 2003. **93**(10): p. 907-916.
54. Wall, M.E., et al., *Mechanisms associated with cGMP binding and activation of cGMP-dependent protein kinase. Proc Natl Acad Sci U S A*, 2003. **100**(5): p. 2380-2385.
55. Schlossmann, J. and M. Desch, *cGK substrates. Handb Exp Pharmacol*, 2009(191): p. 163-193.
56. Hofmann, F., et al., *cGMP regulated protein kinases (cGK). Handb Exp Pharmacol*, 2009(191): p. 137-162.
57. Feil, S., et al., *Distribution of cGMP-dependent protein kinase type I and its isoforms in the mouse brain and retina. Neuroscience*, 2005. **135**(3): p. 863-8.
58. Wen, L., et al., *A shear-dependent NO-cGMP-cGKI cascade in platelets acts as an auto-regulatory brake of thrombosis. Nat Commun*, 2018. **9**(1): p. 4301.

59. Massberg, S., et al., *Increased adhesion and aggregation of platelets lacking cyclic guanosine 3',5'-monophosphate kinase I. J Exp Med*, 1999. **189**(8): p. 1255-64.
60. Wegener, J.W., et al., *cGMP-dependent protein kinase I mediates the negative inotropic effect of cGMP in the murine myocardium. Circ Res*, 2002. **90**(1): p. 18-20.
61. Cary, S.P., J.A. Winger, and M.A. Marletta, *Tonic and acute nitric oxide signaling through soluble guanylate cyclase is mediated by nonheme nitric oxide, ATP, and GTP. Proc Natl Acad Sci U S A*, 2005. **102**(37): p. 13064-13069.
62. Stone, J.R. and M.A. Marletta, *Soluble guanylate cyclase from bovine lung: activation with nitric oxide and carbon monoxide and spectral characterization of the ferrous and ferric states. Biochemistry*, 1994. **33**(18): p. 5636-5640.
63. Pfeifer, A., et al., *Defective smooth muscle regulation in cGMP kinase I-deficient mice. EMBO J*, 1998. **17**(11): p. 3045-51.
64. Sausbier, M., et al., *Mechanisms of NO/cGMP-dependent vasorelaxation. Circ Res*, 2000. **87**(9): p. 825-30.
65. Vaandrager, A.B., et al., *N-terminal myristoylation is required for membrane localization of cGMP-dependent protein kinase type II. J Biol Chem*, 1996. **271**(12): p. 7025-7029.
66. Lohmann, S.M., et al., *Distinct and specific functions of cGMP-dependent protein kinases. Trends Biochem Sci*, 1997(8): p. 307-312.
67. Vaandrager, A.B., B.M. Hogema, and H.R. de Jonge, *Molecular properties and biological functions of cGMP-dependent protein kinase II. Front Biosci*, 2005. **10**: p. 2150-64.
68. Vaandrager, A.B., et al., *Membrane targeting of cGMP-dependent protein kinase is required for cystic fibrosis transmembrane conductance regulator Cl- channel activation. Proc Natl Acad Sci U S A*, 1998. **95**(4): p. 1466-71.
69. Miyazawa, T., et al., *Cyclic GMP-dependent protein kinase II plays a critical role in C-type natriuretic peptide-mediated endochondral ossification. Endocrinology*, 2002. **143**(9): p. 3604-10.
70. Talts, J.F., et al., *Endochondral ossification is dependent on the mechanical properties of cartilage tissue and on intracellular signals in chondrocytes. Ann N Y Acad Sci*, 1998. **857**: p. 74-85.
71. Pfeifer, A., et al., *Intestinal secretory defects and dwarfism in mice lacking cGMP-dependent protein kinase II. Science*, 1996. **274**(5295): p. 2082-6.
72. Oster, H., et al., *cGMP-dependent protein kinase II modulates mPer1 and mPer2 gene induction and influences phase shifts of the circadian clock. Curr Biol*, 2003. **13**(9): p. 725-33.
73. Werner, C., et al., *Importance of NO/cGMP signalling via cGMP-dependent protein kinase II for controlling emotionality and neurobehavioural effects of alcohol. Eur J Neurosci*, 2004. **20**(12): p. 3498-506.
74. Gambaryan, S., et al., *cGMP-dependent protein kinase type II regulates basal level of aldosterone production by zona glomerulosa cells without increasing expression of the steroidogenic acute regulatory protein gene. J Biol Chem*, 2003. **278**(32): p. 29640-8.
75. Spiessberger, B., et al., *cGMP-dependent protein kinase II and aldosterone secretion. FEBS J*, 2009. **276**(4): p. 1007-13.
76. Biel, M. and S. Michalakis, *Cyclic nucleotide-gated channels. Handb Exp Pharmacol*, 2009(191): p. 111-36.
77. Kaupp, U.B. and R. Seifert, *Cyclic nucleotide-gated ion channels. Physiol Rev*, 2002. **82**(3): p. 769-824.
78. Li, M., et al., *Structure of a eukaryotic cyclic-nucleotide-gated channel. Nature*, 2017. **542**: p. 60.
79. Weyand, I., et al., *Cloning and functional expression of a cyclic-nucleotide-gated channel from mammalian sperm. Nature*, 1994. **368**(6474): p. 859-863.
80. Zufall, F., G. Shepherd, and C. Barnstable, *Cyclic nucleotide gated channels as regulators of CNS development and plasticity. Curr Opin Neurobiol*, 1997. **7**(3): p. 404-412.
81. Barnstable, C.J., J.Y. Wei, and M.H. Han, *Modulation of synaptic function by cGMP and cGMP-gated cation channels. Neurochem Int*, 2004. **45**(6): p. 875-884.
82. Komatsu, H., et al., *Mutations in a Cyclic Nucleotide–Gated Channel Lead to Abnormal Thermosensation and Chemosensation in C. elegans. Neuron*, 1996. **17**(4): p. 707-718.
83. Bender, A.T. and J.A. Beavo, *Cyclic nucleotide phosphodiesterases: molecular regulation to clinical use. Pharmacol Rev*, 2006. **58**(3): p. 488-520.
84. Conti, M. and J. Beavo, *Biochemistry and physiology of cyclic nucleotide phosphodiesterases: essential components in cyclic nucleotide signaling. Annu Rev Biochem*, 2007. **76**: p. 481-511.
85. Francis, S.H., J.D. Corbin, and E. Bischoff, *Cyclic GMP-hydrolyzing phosphodiesterases. Handb Exp Pharmacol*, 2009(191): p. 367-408.
86. Kokkonen, K. and D.A. Kass, *Nanodomain Regulation of Cardiac Cyclic Nucleotide Signaling by Phosphodiesterases. Annu Rev Pharmac*, 2017. **57**(1): p. 455-479.

87. Zaccolo, M. and M.A. Movsesian, *cAMP and cGMP signaling cross-talk: role of phosphodiesterases and implications for cardiac pathophysiology. Circ Res*, 2007. **100**(11): p. 1569-1578.
88. Straub, R., et al., *et. al. A possible vulnerability locus for bipolar affective disorder on chromosome 21q22.3. Nat Genet*, 1994. **8**(3): p. 291-296.
89. Sano, H., et al., *Increased social interaction in mice deficient of the striatal medium spiny neuron-specific phosphodiesterase 10A2. J Neurochem*, 2008. **105**(2): p. 546-556.
90. Schmidt, C.J., et al., *et. al. Preclinical characterization of selective phosphodiesterase 10A inhibitors: a new therapeutic approach to the treatment of schizophrenia. J Pharmacol Exp Ther*, 2008. **325**(2): p. 681-690.
91. McDonald, M.L., et al., *Genetic association of cyclic AMP signaling genes with bipolar disorder. Transl Psychiatry*, 2012. **2**: p. e169.
92. Wong, M., et al., *Phosphodiesterase genes are associated with susceptibility to major depression and antidepressant treatment response. Proc Natl Acad Sci U S A*, 2006. **103**(41): p. 15124-15129.
93. Coudray, C., et al., *Evidence for the presence of several phosphodiesterase isoforms in brown adipose tissue of Zucker rats: modulation of PDE2 by the fa gene expression. FEBS Lett*, 1999. **456**(1): p. 207-210.
94. Papadimitriou, A. and K.N. Priftis, *Regulation of the hypothalamic-pituitary-adrenal axis. Neuroimmunomodulation*, 2009. **16**(5): p. 265-71.
95. Kyrou, I. and C. Tsigos, *Stress hormones: physiological stress and regulation of metabolism. Curr Opin Pharmacol*, 2009. **9**(6): p. 787-93.
96. Perlman, R.L. and M. Chalfie, *Catecholamine release from the adrenal medulla. Clin Endocrinol Metab*, 1977. **6**(3): p. 551-76.
97. McEwen, B.S., *Stress, Adaptation, and Disease: Allostasis and Allostatic Load. Ann N Y Acad Sci*, 1998. **840**(1): p. 33-44.
98. Grippo, A.J. and A.K. Johnson, *Stress, depression and cardiovascular dysregulation: A review of neurobiological mechanisms and the integration of research from preclinical disease models. Stress*, 2009. **12**(1): p. 1-21.
99. Dimsdale, J.E., *Psychological Stress and Cardiovascular Disease. J Am Coll Cardiol*, 2008. **51**(13): p. 1237-1246.
100. Kyrou, I., G.P. Chrousos, and C. Tsigos, *Stress, Visceral Obesity, and Metabolic Complications. Ann N Y Acad Sci*, 2006. **1083**(1): p. 77-110.
101. Gross, K.L. and J.A. Cidlowski, *Tissue-specific glucocorticoid action: a family affair. Trends Endocrinol Metab*, 2008. **19**(9): p. 331-9.
102. Mezuk, B., et al., *Depression and Type 2 Diabetes Over the Lifespan. A meta-analysis. Diabetes Care*, 2008. **31**(12): p. 2383-2390.
103. Gerling, A., *Role of the cGMP-dependent protein kinase type I in the regulation of stress response and thermogenesis*. 2012, *University of Tuebingen*.
104. Brann, D.W., et al., *Gaseous transmitters and neuroendocrine regulation. Neuroendocrinology*, 1997. **65**(6): p. 385-95.
105. McCann, S.M., et al., *Hypothalamic control of gonadotropin secretion by LHRH, FSHRF, NO, cytokines, and leptin.* D*omest Anim Endocrinol*, 1998. **15**(5): p. 333-44.
106. McCann, S.M., et al., *Hypothalamic control of FSH and LH by FSH-RF, LHRH, cytokines, leptin and nitric oxide. Neuroimmunomodulation*, 1998. **5**(3-4): p. 193-202.
107. McCann, S.M., et al., *Role of nitric oxide in the neuroendocrine responses to cytokines. Ann N Y Acad Sci*, 1998. **840**: p. 174-84.
108. Ducsay, C.A. and D.A. Myers, *eNOS activation and NO function: differential control of steroidogenesis by nitric oxide and its adaptation with hypoxia. J Endocrinol*, 2011. **210**(3): p. 259-69.
109. Adams, M.L., et al., *Nitric oxide control of steroidogenesis: endocrine effects of NG-nitro-L-arginine and comparisons to alcohol. Life Sci*, 1992. **50**(6): p. Pl35-40.
110. Cymeryng, C.B., L.A. Dada, and E.J. Podesta, *Effect of nitric oxide on rat adrenal zona fasciculata steroidogenesis. J Endocrinol*, 1998. **158**(2): p. 197-203.
111. Mohn, C.E., et al., *The rapid release of corticosterone from the adrenal induced by ACTH is mediated by nitric oxide acting by prostaglandin E2. Proc Natl Acad Sci U S A*, 2005. **102**(17): p. 6213-8.
112. Perras, B., et al., *Intranasal atrial natriuretic peptide acts as central nervous inhibitor of the hypothalamo-pituitary-adrenal stress system in humans. J Clin Endocrinol Metab*, 2004. **89**(9): p. 4642-8.
113. Heisler, S., et al., *Y-1 adrenocortical tumor cells contain atrial natriuretic peptide receptors which regulate cyclic nucleotide metabolism and steroidogenesis. Endocrinology*, 1989. **125**(5): p. 2235-43.

114. Liang, F., et al., *B-Type natriuretic peptide inhibited angiotensin II-stimulated cholesterol biosynthesis, cholesterol transfer, and steroidogenesis in primary human adrenocortical cells. Endocrinology*, 2007. **148**(8): p. 3722-9.
115. MacFarland, R.T., B.D. Zelus, and J.A. Beavo, *High concentrations of a cGMP-stimulated phosphodiesterase mediate ANP-induced decreases in cAMP and steroidogenesis in adrenal glomerulosa cells. J Biol Chem*, 1991. **266**(1): p. 136-42.
116. Nikolaev, V.O., et al., *Real-time monitoring of the PDE2 activity of live cells: hormone-stimulated cAMP hydrolysis is faster than hormone-stimulated cAMP synthesis. J Biol Chem*, 2005. **280**(3): p. 1716-9.
117. Andric, S.A., et al., *Protein kinase G-mediated stimulation of basal Leydig cell steroidogenesis. Am J Physiol Endocrinol Metab*, 2007. **293**(5): p. E1399-408.
118. Kostic, T.S., et al., *Structural complexity of the testis and PKG I / StAR interaction regulate the Leydig cell adaptive response to repeated immobilization stress. Int J Androl*, 2010. **33**(5): p. 717-29.
119. Andric, S.A., et al., *Sildenafil treatment in vivo stimulates Leydig cell steroidogenesis via the cAMP/cGMP signaling pathway. Am J Physiol Endocrinol Metab*, 2010. **299**(4): p. E544-50.
120. Hanke, C.J., et al., *Nitric oxide inhibits aldosterone synthesis by a guanylyl cyclase-independent effect. Endocrinology*, 1998. **139**(10): p. 4053-60.
121. Neff, E.P., *Thermoneutral mice heat up research. Lab Animal*, 2017. **46**: p. 331.
122. Gordon, C.J., *Thermal physiology of laboratory mice: Defining thermoneutrality. J Therm Biol*, 2012. **37**(8): p. 654-685.
123. Goldstein, D.S. and I.J. Kopin, *Evolution of concepts of stress. Stress*, 2007. **10**(2): p. 109-20.
124. Morrison, S.F., K. Nakamura, and C.J. Madden, *Central control of thermogenesis in mammals. Exp Physiol*, 2008. **93**(7): p. 773-97.
125. Kataoka, N., et al., *Psychological Stress Activates a Dorsomedial Hypothalamus-Medullary Raphe Circuit Driving Brown Adipose Tissue Thermogenesis and Hyperthermia. Cell Metab*, 2014. **20**(2): p. 346-358.
126. Cannon, B. and J. Nedergaard, *Brown Adipose Tissue: Function and Physiological Significance*. *Physiol Rev*, 2004. **84**(1): p. 277-359.
127. Symonds, M.E., *Brown Adipose Tissue Growth and Development.* Scientifica, 2013. **2013**: p. 14.
128. Boss, O., P. Muzzin, and J.P. Giacobino, *The uncoupling proteins, a review. Eur J Endocrinol*, 1998. **139**(1): p. 1-9.
129. Morrison, S.F., *Central pathways controlling brown adipose tissue thermogenesis. News Physiol Sci*, 2004. **19**: p. 67-74.
130. Morrison, S.F., C.J. Madden, and D. Tupone, *Central control of brown adipose tissue thermogenesis. Front Endocrinol*, 2012. **3**.
131. Nakamura, K. and S.F. Morrison, *Central efferent pathways mediating skin cooling-evoked sympathetic thermogenesis in brown adipose tissue. Am J Physiol Regul Integr Comp Physiol*, 2007. **292**(1): p. R127-36.
132. Morrison, S.F., W.-H. Cao, and C.J. Madden, *Dorsomedial hypothalamic and brainstem pathways controlling thermogenesis in brown adipose tissue. J Therm Biol*, 2004. **29**(7): p. 333-337.
133. Cao, W.-H. and S.F. Morrison, *Glutamate receptors in the raphe pallidus mediate brown adipose tissue thermogenesis evoked by activation of dorsomedial hypothalamic neurons. Neuropharmacology*, 2006. **51**(3): p. 426-437.
134. Madden, C.J. and S.F. Morrison, *Brown adipose tissue sympathetic nerve activity is potentiated by activation of 5-hydroxytryptamine (5-HT)1A/5-HT7 receptors in the rat spinal cord. Neuropharmacology*, 2008. **54**(3): p. 487-496.
135. De Matteis, R., D. Ricquier, and S. Cinti, *TH-, NPY-, SP-, and CGRP-immunoreactive nerves in interscapular brown adipose tissue of adult rats acclimated at different temperatures: an immunohistochemical study. J Neurocytol*, 1998. **27**(12): p. 877-86.
136. Nagatsu, T., M. Levitt, and S. Udenfriend, *Tyrosine hydroxylase. The Iinitial step in norepinephrine biosynthesis. J Biol Chem*, 1964. **239**: p. 2910-7.
137. Daubner, S.C., T. Le, and S. Wang, *Tyrosine hydroxylase and regulation of dopamine synthesis. Arch Biochem Biophys*, 2011. **508**(1): p. 1-12.
138. Tabrez, S., et al., *A synopsis on the role of tyrosine hydroxylase in Parkinson's disease. CNS Neurol Disord Drug Targets*, 2012. **11**(4): p. 395-409.
139. S, F.Y.K. *Tyrosine hydroxylase defiency*. *GenesReview* 2008, 2017 May 11; Available from: https://www.ncbi.nlm.nih.gov/books/NBK1437/.
140. Dauncey, M.J., *Thyroid hormones and thermogenesis. Proc Nutr Soc*, 1990. **49**(2): p. 203-215.
141. Iwen, K.A., R. Oelkrug, and G. Brabant, *Effects of thyroid hormones on thermogenesis and energy partitioning. J Mol Endocrinol*, 2018. **60**(3): p. R157.

142. Broeders, E.P.M., et al., *Correction: Thyroid Hormone Activates Brown Adipose Tissue and Increases Non-Shivering Thermogenesis—A Cohort Study in a Group of Thyroid Carcinoma Patients. PLOS ONE*, 2018. **13**(12): p. e0209225.
143. Silva, J.E., *Thyroid Hormone Control of Thermogenesis and Energy Balance. Thyroid*, 1995. **5**(6): p. 481-492.
144. Alvarez-Crespo, M., et al., *Essential role of UCP1 modulating the central effects of thyroid hormones on energy balance. Mol Metabol*, 2016. **5**(4): p. 271-282.
145. Hoffmann, L.S., et al., *Stimulation of soluble guanylyl cyclase protects against obesity by recruiting brown adipose tissue. Nat Commun*, 2015. **6**: p. 7235.
146. Hoffmann, L.S., C.J. Larson, and A. Pfeifer, *cGMP and Brown Adipose Tissue. Handb Exp Pharmacol*, 2016. **233**: p. 283-99.
147. Reverte-Salisa, L., A. Sanyal, and A. Pfeifer, *Role of cAMP and cGMP Signaling in Brown Fat. Handb Exp Pharmacol*, 2018.
148. Haas, B., et al., *Protein Kinase G Controls Brown Fat Cell Differentiation and Mitochondrial Biogenesis. Sci Signal*, 2009. **2**(99): p. ra78-.
149. Zhang, X., et al., *Sildenafil promotes adipogenesis through a PKG pathway. Biochem Biophys Res Commun*, 2010. **396**(4): p. 1054-9.
150. Miyashita, K., et al., *Natriuretic peptides/cGMP/cGMP-dependent protein kinase cascades promote muscle mitochondrial biogenesis and prevent obesity. Diabetes*, 2009. **58**(12): p. 2880-92.
151. Sengenès, C., et al., *Involvement of a cGMP-dependent Pathway in the Natriuretic Peptide-mediated Hormone-sensitive Lipase Phosphorylation in Human Adipocytes. J Biol Chem*, 2003. **278**(49): p. 48617-48626.
152. Virtanen, K.A., et al., *Functional Brown Adipose Tissue in Healthy Adults. N Engl J Med*, 2009. **360**(15): p. 1518-1525.
153. Nedergaard, J., T. Bengtsson, and B. Cannon, *Unexpected evidence for active brown adipose tissue in adult humans. Am J Physiol Endocrinol Metab*, 2007. **293**(2): p. E444-52.
154. Cypess, A.M., et al., *Identification and importance of brown adipose tissue in adult humans. N Engl J Med*, 2009. **360**(15): p. 1509-17.
155. Nedergaard, J., T. Bengtsson, and B. Cannon, *New Powers of Brown Fat: Fighting the Metabolic Syndrome. Cell Metabolism*. **13**(3): p. 238-240.
156. Bartelt, A., et al., *Brown adipose tissue activity controls triglyceride clearance. Nat Med*, 2011. **17**(2): p. 200-5.
157. Cinti, S., *The role of brown adipose tissue in human obesity. Nutr Metab Cardiovasc Dis*, 2006. **16**(8): p. 569-574.
158. Kershaw, E.E. and J.S. Flier, *Adipose tissue as an endocrine organ. J Clin Endocrinol Metab*, 2004. **89**(6): p. 2548-56.
159. Vijgen, G.H.E.J., et al., *Brown Adipose Tissue in Morbidly Obese Subjects. PLOS ONE*, 2011. **6**(2): p. e17247.
160. Birling, M.-C., F. Gofflot, and X. Warot, *Site-Specific Recombinases for Manipulation of the Mouse Genome*, in *Transgenesis Techniques*, E.J. Cartwright, Editor, *Transgenesis Techniques*, 2009, Humana Press. p. 245-263.
161. Barrangou, R. and J.A. Doudna, *Applications of CRISPR technologies in research and beyond. Nat Biotechnol*, 2016. **34**(9): p. 933-941.
162. Mural, R.J., *et. al. A comparison of whole-genome shotgun-derived mouse chromosome 16 and the human genome. Science*, 2002. **296**(5573): p. 1661-1671.
163. Waterston, R.H., *et. al. Initial sequencing and comparative analysis of the mouse genome. Nature*, 2002. **420**(6915): p. 520-562.
164. Couzin-Frankel, J., *When Mice Mislead. Science*, 2013. **342**(6161): p. 922-925.
165. Feil, S., N. Valtcheva, and R. Feil, *Inducible Cre Mice. Methods Mol Biol*, 2009. **530**: p. 343-63.
166. Sternberg, N. and D. Hamilton, *Bacteriophage P1 site-specific recombination. I. Recombination between loxP sites. J Mol Biol*, 1981. **150**(4): p. 467-486.
167. Feil, R., et al., *Ligand-activated site-specific recombination in mice. Proc Natl Acad Sci U S A*, 1996. **93**(20): p. 10887-10890.
168. Feil, R., et al., *Regulation of Cre Recombinase Activity by Mutated Estrogen Receptor Ligand-Binding Domains. Biochem Biophys Res Commun*, 1997. **237**(3): p. 752-757.
169. Metzger, D. and R. Feil, *Engineering the mouse genome by site-specific recombination. Curr Opin Biotechnol*, 1999. **5**: p. 470-476.
170. Muzumdar, M.D., et al., *A global double-fluorescent Cre reporter mouse. Genesis*, 2007. **45**(9): p. 593-605.

171. Soriano, P., *Generalized lacZ expression with the ROSA26 Cre reporter strain. Nat Genet*, 1999. **21**: p. 70.
172. Madisen, L., et al., *A robust and high-throughput Cre reporting and characterization system for the whole mouse brain. Nat Neurosci*, 2010. **13**(1): p. 133-140.
173. Pichler, B.J., H.F. Wehrl, and M.S. Judenhofer, *Latest advances in molecular imaging instrumentation. J Nucl Med*, 2008. **49 Suppl 2**: p. 5s-23s.
174. de Kemp, R.A., et al., *Small-Animal Molecular Imaging Methods. J Nucl Med*, 2010. **51**(Supplement 1): p. 18S-32S.
175. Cherry, S.R. and S.S. Gambhir, *Use of positron emission tomography in animal research. Ilar J*, 2001. **42**(3): p. 219-32.
176. Phelps, M.E., *Positron emission tomography provides molecular imaging of biological processes. Proc Natl Acad Sci U S A*, 2000. **97**(16): p. 9226-33.
177. Antoni, G. and B. Långström, *Radiopharmaceuticals: Molecular Imaging using Positron Emission Tomography*. W. Semmler and M. Schwaiger, Editors. *Molecular Imaging I*, 2008. *Springer Berlin* Heidelberg: Berlin, Heidelberg. p. 177-201.
178. Sossi, V. and T.J. Ruth, *Micropet imaging: in vivo biochemistry in small animals. J Neural Transm* (Vienna), 2005. **112**(3): p. 319-30.
179. Thunemann, M., *Generation and characterization of transgenic mice for noninvasive cell tracking with PET and for FRET-based cGMP imaging*, in *Faculty of mathematical and natural sciences*. 2012, University of Tuebingen. p. 160.
180. Brooker, G., L.J. Thomas, Jr., and M.M. Appleman, *The assay of adenosine 3',5'-cyclic monophosphate and guanosine 3',5'-cyclic monophosphate in biological materials by enzymatic radioisotopic displacement. Biochemistry*, 1968. **7**(12): p. 4177-81.
181. Brooker, G., et al., *Radioimmunoassay of cyclic AMP and cyclic GMP. Adv Cyclic Nucleotide Res*, 1979. **10**: p. 1-33.
182. Sprenger, J.U. and V.O. Nikolaev, *Biophysical techniques for detection of cAMP and cGMP in living cells. Int J Mol Sci*, 2013. **14**(4): p. 8025-8046.
183. Hahn, K. and A. Toutchkine, *Live-cell fluorescent biosensors for activated signaling proteins. Curr Opin Cell Biol*, 2002. **14**(2): p. 167-172.
184. Thunemann, M., et al., *Transgenic mice for cGMP imaging. Circ Res*, 2013. **113**(4): p. 365-71.
185. Russwurm, M., et al., *Design of fluorescence resonance energy transfer (FRET)-based cGMP indicators: a systematic approach. Biochem J*, 2007. **407**(1): p. 69-77.
186. Förster, T., *Zwischenmolekulare Energiewanderung und Fluoreszenz. Ann Phys*, 1948. **437**: p. 55-75.
187. Lehners, M., et al., *cGMP signaling and vascular smooth muscle cell plasticity. J Cardiovasc Dev Dis*, 2018. **5**(2): p. pii: E20.
188. Tronche, F., et al., *Disruption of the glucocorticoid receptor gene in the nervous system results in reduced anxiety. Nat Genet*, 1999. **23**(1): p. 99-103.
189. Ter-Avetisyan, G., F.G. Rathjen, and H. Schmidt, *Bifurcation of Axons from Cranial Sensory Neurons Is Disabled in the Absence of Npr2-Induced cGMP Signaling. J Neurosci*, 2014. **34**(3): p. 737-747.
190. Galichet, C., R. Lovell-Badge, and K. Rizzoti, *Nestin-Cre Mice Are Affected by Hypopituitarism, Which Is Not Due to Significant Activity of the Transgene in the Pituitary Gland. PLoS ONE*, 2010. **5**(7): p. e11443.
191. Rothwell, N.J. and M.J. Stock, *A role for brown adipose tissue in diet-induced thermogenesis. Nature*, 1979. **281**(5726): p. 31-35.
192. Westerterp, K.R., *Diet induced thermogenesis. Nutr Metabol*, 2004. **1**(1): p. 5.
193. Feldman, A.T. and D. Wolfe, *Tissue Processing and Hematoxylin and Eosin Staining*. *Histopathology*. p. 31-43.
194. Qidwai, K., M. Afkhami, and C.E. Day, *The Pathologist's Guide to Fixatives*. *Histopathology*. p. 21-30.
195. Hsu, S.M., L. Raine, and H. Fanger, *Use of avidin-biotin-peroxidase complex (ABC) in immunoperoxidase techniques: a comparison between ABC and unlabeled antibody (PAP) procedures. J Histochem Cytochem*, 1981. **29**(4): p. 577-580.
196. Odell, I.D. and D. Cook, *Optimizing Direct Immunofluorescence. Histopathology*. p. 111-117.
197. Lowry, O.H., et al., *Protein measurement with the Folin phenol reagent. J Biol Chem*, 1951. **193**(1): p. 265-75.
198. Laemmli, U.K., *Cleavage of Structural Proteins during the Assembly of the Head of Bacteriophage T4. Nature*, 1970. **227**: p. 680.
199. Dallner, O.S., et al., *Beta3-adrenergic receptors stimulate glucose uptake in brown adipocytes by two mechanisms independently of glucose transporter 4 translocation. Endocrinology*, 2006. **147**(12): p. 5730-9.

200. Slot, J.W., et al., *Immuno-localization of the insulin regulatable glucose transporter in brown adipose tissue of the rat. J Cell Biol*, 1991. **113**(1): p. 123-135.

201. Wang, X., L.J. Minze, and Z.-Z. Shi, *Functional Imaging of Brown Fat in Mice with (18)F-FDG micro-PET/CT. JoVE*, 2012(69): p. 4060.

202. Gnad, T., et al., *Adenosine activates brown adipose tissue and recruits beige adipocytes via A2A receptors. Nature*, 2014. **516**: p. 395.

203. Valtcheva, N., et al., *The commonly used cGMP-dependent protein kinase type I (cGKI) inhibitor Rp-8-Br-PET-cGMPS can activate cGKI in vitro and in intact cells. J Biol Chem*, 2009. **284**(1): p. 556-562.

204. Cuervo, H., et al., *PDGFRβ-P2A-CreER(T2) mice: a genetic tool to target pericytes in angiogenesis. Angiogenesis*, 2017. **20**(4): p. 655-662.

205. Yamazaki, T. and Y.-s. Mukouyama, *Tissue Specific Origin, Development, and Pathological Perspectives of Pericytes. Front Cardiovasc Med*, 2018. **5**(78).

206. Dubois, N.C., et al., *Nestin-Cre transgenic mouse line Nes-Cre1 mediates highly efficient Cre/loxP mediated recombination in the nervous system, kidney, and somite-derived tissues. Genesis*, 2006. **44**(8): p. 355-360.

207. Bamshad, M., C.K. Song, and T.J. Bartness, *CNS origins of the sympathetic nervous system outflow to brown adipose tissue*. *Am J Physiol*, 1999. **276**: p. 1569-R1578.

208. Leiss, V., et al., *Expression of cGMP-dependent protein kinase type I in mature white adipocytes. Biochem Biophys Res Commun*, 2014. **452**(1): p. 151-156.

209. Mitschke, M.M., et al., *Increased cGMP promotes healthy expansion and browning of white adipose tissue. FASEB J*, 2013. **27**(4): p. 1621-1630.

210. Li, S., et al., *Overview of the reporter genes and reporter mouse models. Animal Model Exp Med*, 2018. **1**(1): p. 29-35.

211. Araki, K., et al., *Site-specific recombination of a transgene in fertilized eggs by transient expression of Cre recombinase. Proc Natl Acad Sci U S A*, 1995. **92**(1): p. 160-4.

212. Lobe, C.G., et al., *Z/AP, a double reporter for cre-mediated recombination. Dev Biol*, 1999. **208**(2): p. 281-92.

213. Livet, J., et al., *Transgenic strategies for combinatorial expression of fluorescent proteins in the nervous system. Nature*, 2007. **450**: p. 56.

214. Cai, D., et al., *Improved tools for the Brainbow toolbox. Nat Methods*, 2013. **10**(6): p. 540-7.

215. Liang, H., S. Hippenmeyer, and H.T. Ghashghaei, *A Nestin-cre transgenic mouse is insufficient for recombination in early embryonic neural progenitors. Biology Open*, 2012: p. BIO20122287.

216. Steenblock, C., et al., *Isolation and characterization of adrenocortical progenitors involved in the adaptation to stress. Proc Natl Acad Sci U S A*, 2018. **115**(51): p. 12997-13002.

217. Wasserstein, R.L. and N.A. Lazar, *The ASA Statement on p-Values: Context, Process, and Purpose.* The *Am Stat*, 2016. **70**(2): p. 129-133.

218. Wasserstein, R.L., A.L. Schirm, and N.A. Lazar, *Moving to a World Beyond “p < 0.05”. Am Stat*, 2019. **73**(sup1): p. 1-19.

219. Valentin Amrhein, S.G. &, and B. McShane, *Scientists rise up against statistical significance. Nature*, 2019(567): p. 305-307.

220. Talan, M., *Body temperature of C57BL/6J mice with age. Exp Gerontol*, 1984. **19**(1): p. 25-29.

221. Declercq, J., et al., *Metabolic and Behavioural Phenotypes in Nestin-Cre Mice Are Caused by Hypothalamic Expression of Human Growth Hormone. PloS one*, 2015. **10**(8): p. e0135502-e0135502.

222. Meyer, C.W., Y. Ootsuka, and A.A. Romanovsky, *Body Temperature Measurements for Metabolic Phenotyping in Mice. Front Physiol*, 2017. **8**(520).

223. Periasamy, M., J.L. Herrera, and F.C.G. Reis, *Skeletal Muscle Thermogenesis and Its Role in Whole Body Energy Metabolism. Diabetes Metab*, 2017. **41**(5): p. 327-336.

224. Fuller-Jackson, J.-P. and B.A. Henry, *Adipose and skeletal muscle thermogenesis: studies from large animals. J Endocrinol*, 2018. **237**(3): p. R99.

225. Bal, N.C., et al., *Sarcolipin is a newly identified regulator of muscle-based thermogenesis in mammals. Nat Med*, 2012. **18**(10): p. 1575-9.

226. Simonides, W.S., et al., *Mechanism of thyroid-hormone regulated expression of the SERCA genes in skeletal muscle: implications for thermogenesis. Biosci Rep*, 2001. **21**(2): p. 139-54.

227. Rowland, L.A., et al., *Uncoupling Protein 1 and Sarcolipin Are Required to Maintain Optimal Thermogenesis, and Loss of Both Systems Compromises Survival of Mice under Cold Stress. J Biol Chem*, 2015. **290**(19): p. 12282-12289.

228. Bal, N.C., et al., *Increased Reliance on Muscle-based Thermogenesis upon Acute Minimization of Brown Adipose Tissue Function. J Biol Chem*, 2016. **291**(33): p. 17247-17257.

229. Yao, R., R. Lecomte, and E.S. Crawford, *Small-Animal PET: What Is It, and Why Do We Need It? J Nucl Med Technol*, 2012. **40**(3): p. 157-165.

230. Hutchins, G.D., et al., *Small Animal PET Imaging. ILAR J*, 2008. **49**(1): p. 54-65.
231. Lancelot, S. and L. Zimmer, *Small-animal positron emission tomography as a tool for neuropharmacology. Trends Pharmacol Sci*, 2010. **31**(9): p. 411-417.
232. Crandall, J.P., et al., *Repeatability of brown adipose tissue measurements on FDG PET/CT following a simple cooling procedure for BAT activation. PLOS ONE*, 2019. **14**(4): p. e0214765.
233. Golozoubova, V., et al., *Only UCP1 can mediate adaptive nonshivering thermogenesis in the cold. FASEB J*, 2001. **15**(11): p. 2048-2050.
234. Kawashita, N.H., et al., *Glucose uptake, glucose transporter GLUT4, and glycolytic enzymes in brown adipose tissue from rats adapted to a high-protein diet. Metabolism*, 2002. **51**(11): p. 1501-5.
235. Shin, H., et al., *Lipolysis in Brown Adipocytes Is Not Essential for Cold-Induced Thermogenesis in Mice. Cell Metabolism*, 2017. **26**(5): p. 764-777.e5.
236. Leto, D. and A.R. Saltiel, *Regulation of glucose transport by insulin: traffic control of GLUT4. Nat Rev Mol Cell Biol*, 2012. **13**: p. 383.
237. Nikami, H., et al., *Cold exposure increases glucose utilization and glucose transporter expression in brown adipose tissue. Biochem Biophys Res Commun*, 1992. **185**(3): p. 1078-1082.
238. Shimizu, Y., et al., *Increased expression of glucose transporter GLUT-4 in brown adipose tissue of fasted rats after cold exposure. Am J Physiol*, 1993. **264**(6 Pt 1): p. E890-5.
239. Olichon-Berthe, C., E. Van Obberghen, and Y. Le Marchand-Brustel, *Effect of cold acclimation on the expression of glucose transporter Glut 4. Mol Cell Endocrinol*, 1992. **89**(1-2): p. 11-8.
240. Huang, S. and M.P. Czech, *The GLUT4 Glucose Transporter. Cell Metabolism*, 2007. **5**(4): p. 237-252.
241. Skorobogatko, Y., et al., *RalA controls glucose homeostasis by regulating glucose uptake in brown fat. Proc Natl Acad Sci U S A*, 2018. **115**(30): p. 7819-7824.
242. Lee, P., et al., *Brown Adipose Tissue Exhibits a Glucose-Responsive Thermogenic Biorhythm in Humans. Cell Metabolism*, 2016. **23**(4): p. 602-609.
243. Lutz, S.Z., et al., *Genetic Ablation of cGMP-Dependent Protein Kinase Type I Causes Liver Inflammation and Fasting Hyperglycemia. Diabetes*, 2011. **60**(5): p. 1566-1576.
244. Ghorbani, S., et al., *Regulation of tyrosine hydroxylase is preserved across different homo- and heterodimeric 14-3-3 proteins. Amino Acids*, 2016. **48**(5): p. 1221-1229.
245. Jorge-Finnigan, A., et al., *Phosphorylation at serine 31 targets tyrosine hydroxylase to vesicles for transport along microtubules. J Biol Chem*, 2017. **292**(34): p. 14092-14107.
246. Toska, K., et al., *Regulation of tyrosine hydroxylase by stress-activated protein kinases. J Neurochem*, 2002. **83**(4): p. 775-83.
247. Nguyen, K.D., et al., *Alternatively activated macrophages produce catecholamines to sustain adaptive thermogenesis. Nature*, 2011. **480**(7375): p. 104-8.
248. Fischer, K., et al., *Alternatively activated macrophages do not synthesize catecholamines or contribute to adipose tissue adaptive thermogenesis. Nat Med*, 2017. **23**: p. 623.
249. Villarroya, F., et al., *Toward an Understanding of How Immune Cells Control Brown and Beige Adipobiology. Cell Metabolism*, 2018. **27**(5): p. 954-961.
250. Pirzgalska, R.M., et al., *Sympathetic neuron-associated macrophages contribute to obesity by importing and metabolizing norepinephrine. Nat Med*, 2017. **23**(11): p. 1309-1318.
251. Gaudry, M.J. and K.L. Campbell, *Evolution of UCP1 Transcriptional Regulatory Elements Across the Mammalian Phylogeny. Front Physiol*, 2017. **8**(670).
252. Mory, G., et al., *Noradrenaline controls the concentration of the uncoupling protein in brown adipose tissue. FEBS Lett*, 1984. **166**(2): p. 393-6.
253. Azzu, V., et al., *The regulation and turnover of mitochondrial uncoupling proteins. Biochim Biophys Acta*, 2010. **1797**(6-7): p. 785-791.
254. Divakaruni, A.S., D.M. Humphrey, and M.D. Brand, *Fatty Acids Change the Conformation of Uncoupling Protein 1 (UCP1). J Biol Chem*, 2012. **287**(44): p. 36845-36853.
255. Wang, G., et al., *Regulation of UCP1 and Mitochondrial Metabolism in Brown Adipose Tissue by Reversible Succinylation. Molecular Cell*, 2019. **74**(4): p. 844-857.e7.
256. Shimizu, Y., et al., *Effects of noradrenaline on the cell-surface glucose transporters in cultured brown adipocytes: novel mechanism for selective activation of GLUT1 glucose transporters. Biochem J*, 1998. **330 (Pt 1)**: p. 397-403.
257. Chernogubova, E., B. Cannon, and T. Bengtsson, *Norepinephrine Increases Glucose Transport in Brown Adipocytes via β3-Adrenoceptors through a cAMP, PKA, and PI3-Kinase-Dependent Pathway Stimulating Conventional and Novel PKCs. Endocrinology*, 2004. **145**(1): p. 269-280.
258. Weiner, J., et al., *Thyroid hormones and browning of adipose tissue. Mol Cell Endocrinol*, 2017. **458**: p. 156-159.
259. Carvalho, S.D., et al., *Central Role of Brown Adipose Tissue Thyroxine 5'-Deiodinase on Thyroid Hormone-Dependent Thermogenic Response to Cold. Endocrinology*, 1991. **128**(4): p. 2149-2159.

260. de Jesus, L.A., et al., *The type 2 iodothyronine deiodinase is essential for adaptive thermogenesis in brown adipose tissue. J Clin Invest*, 2001. **108**(9): p. 1379-1385.
261. Lopez, M., et al., *Hypothalamic AMPK and fatty acid metabolism mediate thyroid regulation of energy balance. Nat Med*, 2010. **16**: p. 1001-1008.
262. Triandafillou, J., C. Gwilliam, and J. Himms-Hagen, *Role of thyroid hormone in cold-induced changes in rat brown adipose tissue mitochondria. Can J Biochem*, 1982. **60**(5): p. 530-7.
263. Bottenstein, J.E., *Growth Requirements of Neural Cells in Vitro. Advanc Cell Neurob*, 1983, Elsevier. p. 333-379.
264. Bottenstein, J.E., *Growth and Differentiation of Neural Cells in Defined Media. Cell Cult Neurosci*, 1985. Springer US: Boston, MA. p. 3-43.
265. Owens, G.K., *Regulation of differentiation of vascular smooth muscle cells. Physiol Rev*, 1995. **75**(3): p. 487-517.
266. Chamley-Campbell, J., G.R. Campbell, and R. Ross, *The smooth muscle cell in culture. Physiol Rev*, 1979. **59**(1): p. 1-61.
267. Worth, N.F., et al., *Vascular smooth muscle cell phenotypic modulation in culture is associated with reorganisation of contractile and cytoskeletal proteins. Cell Motil Cytoskeleton*, 2001. **49**(3): p. 130-45.
268. Okamura, H., et al., *Atrial natriuretic peptide receptors are present in brown adipose tissue.* Biochem *Biophys Res Commun*, 1988. **156**(2): p. 1000-6.
269. Hampton, M., R.G. Melvin, and M.T. Andrews, *Transcriptomic Analysis of Brown Adipose Tissue across the Physiological Extremes of Natural Hibernation. PLOS ONE*, 2014. **8**(12): p. e85157.
270. Dessì-Fulgheri, P., R. Sarzani, and A. Rappelli, *Role of the natriuretic peptide system in lipogenesis/lipolysis. Nutr Metabol Cardiovasc Dis*, 2003. **13**(4): p. 244-249.
271. Schmidt, H., et al., *The receptor guanylyl cyclase Npr2 is essential for sensory axon bifurcation within the spinal cord. J Cell Biol*, 2007. **179**(2): p. 331-340.
272. Wolter, S., et al., *GC-B Deficient Mice With Axon Bifurcation Loss Exhibit Compromised Auditory Processing. Front Neural Circuits*, 2018. **12**: p. 65-65.
273. Schmidt, H. and B. Fritzsch, *Npr2 null mutants show initial overshooting followed by reduction of spiral ganglion axon projections combined with near-normal cochleotopic projection. Cell Tissue Res*, 2019.
274. Thunemann, M., et al., *Visualization of cGMP with cGi biosensors. Methods Mol Biol*, 2013. **1020**: p. 89-120.
275. Schmidt, H., et al., *Dorsal root ganglion axon bifurcation tolerates increased cyclic GMP levels: the role of phosphodiesterase 2A and scavenger receptor Npr3. Eur J Neurosci*, 2016. **44**(12): p. 2991-3000.
276. Dore-Duffy, P. and K. Cleary, *Morphology and Properties of Pericytes*, in *The Blood-Brain and Other Neural Barriers: Reviews and Protocols*, *Humana Press*. 2011, p. 49-68.
277. Hartmann, D.A., et al., *Pericyte structure and distribution in the cerebral cortex revealed by high-resolution imaging of transgenic mice. Neurophotonics*, 2015. **2**(4): p. 1-13, 13.
278. Armulik, A., et al., *Pericytes regulate the blood–brain barrier. Nature*, 2010. **468**: p. 557.
279. Chen, J., et al., *CD146 is essential for PDGFRβ-induced pericyte recruitment. Protein Cell*, 2018. **9**(8): p. 743-747.
280. Krueger, M. and I. Bechmann, *CNS pericytes: Concepts, misconceptions, and a way out. Glia*, 2010. **58**(1): p. 1-10.
281. Trost, A., et al., *Brain and Retinal Pericytes: Origin, Function and Role. Front Cell Neurosci*, 2016. **10**(20).
282. Hall, C.N., et al., *Capillary pericytes regulate cerebral blood flow in health and disease. Nature*, 2014. **508**(7494): p. 55-60.
283. Hill, R.A., et al., *Regional Blood Flow in the Normal and Ischemic Brain Is Controlled by Arteriolar Smooth Muscle Cell Contractility and Not by Capillary Pericytes. Neuron*, 2015. **87**(1): p. 95-110.
284. Armulik, A., A. Abramsson, and C. Betsholtz, *Endothelial/pericyte interactions. Circ Res*, 2005. **97**(6): p. 512-23.
285. Attwell, D., et al., *What is a pericyte? J Cereb Blood flow Metab*, 2016. **36**(2): p. 451-455.
286. Iwayama, T., et al., *PDGFRα signaling drives adipose tissue fibrosis by targeting progenitor cell plasticity. Genes Dev*, 2015. **29**(11): p. 1106–1119
287. Nehls, V. and D. Drenckhahn, *Heterogeneity of microvascular pericytes for smooth muscle type alpha-actin. J Cell Biol*, 1991. **113**(1): p. 147-154.
288. Birbrair, A., et al., *Skeletal muscle pericyte subtypes differ in their differentiation potential. Stem cell Res*, 2013. **10**(1): p. 67-84.
289. Stallcup, W.B., *The NG2 proteoglycan: past insights and future prospects. J Neurocytol*, 2002. **31**(6-7): p. 423-35.
290. Birbrair, A., et al., *Type-2 pericytes participate in normal and tumoral angiogenesis. Am J Physiol*, 2014. **307**(1): p. C25-C38.

291. Doherty, M.J., et al., *Vascular Pericytes Express Osteogenic Potential In Vitro and In Vivo. J Bone Miner Res*, 1998. **13**(5): p. 828-838.
292. Farrington-Rock, C., et al., *Chondrogenic and Adipogenic Potential of Microvascular Pericytes. Circulation*, 2004. **110**(15): p. 2226-2232.
293. Dellavalle, A., et al., *Pericytes resident in postnatal skeletal muscle differentiate into muscle fibres and generate satellite cells. Nat Commun*, 2011. **2**: p. 499.
294. Tang, W., et al., *White fat progenitor cells reside in the adipose vasculature. Science*, 2008. **322**(5901): p. 583-6.
295. Enerback, S., *The origins of brown adipose tissue. N Engl J Med*, 2009. **360**(19): p. 2021-3.
296. Tran, K.-V., et al., *The Vascular Endothelium of the Adipose Tissue Gives Rise to Both White and Brown Fat Cells. Cell Metabolism*, 2012. **15**(2): p. 222-229.
297. Birbrair, A., et al., *Role of pericytes in skeletal muscle regeneration and fat accumulation. Stem Cells Dev*, 2013. **22**(16): p. 2298-2314.
298. Mendel, T.A., et al., *Pericytes Derived from Adipose-Derived Stem Cells Protect against Retinal Vasculopathy. PLOS ONE*, 2013. **8**(5): p. e65691.
299. König, P., et al., *NO-sensitive guanylyl cyclase is expressed in pericytes but absent from endothelial cells in the murine lung. BMC Pharmacology*, 2011. **11**(1): p. P38.
300. Ehrhart-Bornstein, M., et al., *Intraadrenal interactions in the regulation of adrenocortical steroidogenesis. Endocr Rev*, 1998. **19**(2): p. 101-43.
301. Camell, C.D., et al., *Inflammasome-driven catecholamine catabolism in macrophages blunts lipolysis during ageing. Nature*, 2017. **550**: p. 119.